INFORMATION TO USERS

This manuscript has been reproduced from the microfilm master. UMI films the text directly from the original or copy submitted. Thus, some thesis and dissertation copies are in typewriter face, while others may be from any type of computer printer.

The quality of this reproduction is dependent upon the quality of the copy submitted. Broken or indistinct print, colored or poor quality illustrations and photographs, print bleedthrough, substandard margins, and improper alignment can adversely affect reproduction.

In the unlikely event that the author did not send UMI a complete manuscript and there are missing pages, these will be noted. Also, if unauthorized copyright material had to be removed, a note will indicate the deletion.

Oversize materials (e.g., maps, drawings, charts) are reproduced by sectioning the original, beginning at the upper left-hand corner and continuing from left to right in equal sections with small overlaps.

Photographs included in the original manuscript have been reproduced xerographically in this copy. Higher quality 6" x 9" black and white photographic prints are available for any photographs or illustrations appearing in this copy for an additional charge. Contact UMI directly to order.

ProQuest Information and Learning
300 North Zeeb Road, Ann Arbor, MI 48106-1346 USA
800-521-0600

UMI®

MODELLING STUDIES OF GLACIAL-INTERGLACIAL TRANSITIONS

by

MASAKAZU YOSHIMORI
B.Eng., Waseda University, 1995
M.Eng., Waseda University, 1997

A Dissertation Submitted in Partial Fulfillment of the
Requirements for the Degree of

DOCTOR OF PHILOSOPHY

in the School of Earth and Ocean Sciences

We accept this dissertation as conforming
to the required standard

Dr. A. J. Weaver, Supervisor (School of Earth and Ocean Sciences)

Dr. G. M. Flato, Member (School of Earth and Ocean Sciences)

Dr. N. A. McFarlane, Member (School of Earth and Ocean Sciences)

Dr. N. J. Livingston, Outside Member (Department of Biology)

Dr. A. J. Broccoli, External Examiner (NOAA, Geophysical Fluid Dynamics Laboratory)

University of Victoria

Supervisor: Dr. A. J. Weaver

Abstract

Glaciation/deglaciation is one of the most extreme and fundamental climatic events in Earth's history. The origin of the glacial-interglacial cycles has been explored for more than a century and the astronomical theory is now well established. However, the mechanism that links the astronomical forcing to the geological record in the Earth's climate system is poorly understood. In this thesis, aspects of the last glacial termination and the last glacial inception, are studied.

First, the response of ocean's thermohaline circulation to changes in orbital geometry and atmospheric CO_2 concentration in the last glacial termination is investigated using a coupled climate (atmosphere-ocean-sea ice) model. It is shown that the thermohaline circulation is affected by both orbital and CO_2 forcing and the details of the mechanisms involved are explored. The climatic impact of changes in the thermohaline circulation is then investigated. It is revealed that the influence of changes in the thermohaline circulation on surface air temperature is concentrated in the North Atlantic and adjacent continents. It is also shown that this influence has its peak in winter rather than in summer. A dynamic ice sheet model is then globally and asynchronously coupled to the climate model. The relative importance of orbital and CO_2 forcing in the mass balance of ice sheets is investigated using the coupled climate-ice sheet model. It is shown that CO_2 forcing is of secondary importance to orbital forcing as the warming in eastern North America and Scandinavia due to CO_2 forcing has its peak in winter, whereas that due to orbital forcing has its peak in summer. It is, nevertheless, concluded that the last glacial termination was initiated through increasing summer insolation and accelerated by a subsequent increase in atmospheric CO_2 concentration.

Second, the importance of subgrid topography in simulating the last glacial inception is investigated using the coupled climate model. The effects of subgrid elevation and subgrid ice-flow are incorporated in the model. Despite the use of high subgrid resolution, the coupled climate model fails to capture the last glacial inception. An atmospheric general circulation model is then used to explore the reasons for the failure, as well as the importance of changes in sea surface conditions and vegetation in simulating the last glacial inception. A realistic, geographic distribution of perennial snow cover and global net accumulation rate are successfully simulated when colder sea surface conditions than those of the present-day are specified. It is also shown that the effect of the vegetation feedback is large.

It is revealed that changes in ocean circulation and vegetation are at least partly responsible for the complicated link between astronomical forcing and climate states during the glacial-interglacial cycles. As these two components play important roles, it is suggested that both components as well as ice sheet dynamics should be included in realistic paleoclimate simulations.

Examiners:

Dr. A. J. Weaver, Supervisor (School of Earth and Ocean Sciences)

Dr. G. M. Flato, Member (School of Earth and Ocean Sciences)

Dr. N. A. McFarlane, Member (School of Earth and Ocean Sciences)

Dr. N. J. Livingston, Outside Member (Department of Biology)

Dr. A. J. Broccoli, External Examiner (NOAA, Geophysical Fluid Dynamics Laboratory)

Table of Contents

Abstract ii

Table of Contents iv

List of Tables vii

List of Figures viii

Acknowledgements xii

1 Introduction 1

1.1 Introduction 1

1.2 Orbital forcing 2

1.3 Glacial-interglacial cycles 4

1.4 Role of ocean and atmospheric CO_2 concentration 7

1.5 Paleoclimate modelling 9

2 Model descriptions 12

2.1 The coupled climate model 12

2.1.1 The atmosphere component 12

2.1.2 The ocean component 19

2.1.3 The sea ice component 23

2.2 The ice sheet model 27

2.2.1 Dynamics 27

2.2.2 Glacio-isostacy 29

2.3 Atmospheric general circulation model 29

3 Glacial termination: Changes in thermohaline circulation 32

3.1 Introduction 32

3.2 Experimental design 35

3.3 Results 38

3.3.1 Meridional overturning streamfunction 38
3.3.2 Depth-integrated steric height 39
3.3.3 Effect of atmospheric CO_2 concentration 42
3.3.4 Effect of orbital parameters 45
3.4 Discussion 53
3.5 Conclusion 61

4 Glacial termination: Changes in climate and ice sheet **63**
4.1 Introduction 63
4.2 Coupling of the ice sheet model 65
4.3 Experimental design 69
4.4 Results 70
4.4.1 Climate model response 70
4.4.2 Ice-sheet response 81
4.5 Discussion 86
4.6 Conclusion 90

5 Glacial inception: Effect of subgrid topography **92**
5.1 Introduction 92
5.2 Subgrid treatment and experimental design 93
5.3 Results 101
5.3.1 The effect of subgrid elevation 101
5.3.2 The effect of subgrid ice-flow 103
5.4 Discussion and conclusion 108

6 Glacial inception: Effect of surface conditions **110**
6.1 Introduction 110
6.2 Experimental design 114
6.3 Results 119
6.3.1 Coupled model simulated sea surface conditions 119
6.3.2 Present-day AGCM Simulations 120
6.3.3 116 kaBP AGCM Simulations 123
6.4 Discussion 136
6.5 Conclusion 137

7 Conclusion **139**

Bibliography 143

Glossary of Acronyms 166

VITA 168

List of Tables

3.1 Experimental design for CO_2 perturbation 36
3.2 Orbital parameters used in the experiments 37
3.3 Experimental design for orbital perturbation 37
3.4 Annual mean response to CO_2 forcing 43
3.5 Annual mean response to orbital forcing 49

4.1 Annual mean response of the climate model 75
4.2 Comparison between the climate model (model 1) and the coupled climate-ice sheet model (model 2) 85

5.1 Experiments using the coupled climate model (PD: present-day) 94
5.2 Resolution of the subcell 96
5.3 Experimental design for the study of subgrid elevation (PD: Present-day) . 98
5.4 Experimental design for the study of subgrid ice-flow (PD: Present-day) . . 100
5.5 Snowfall rate (10^{-3} m yr^{-1}) 101
5.6 Snow melting rate (10^{-3} m yr^{-1}) 101
5.7 Net accumulation rate (10^{-4} m yr^{-1}) 102

6.1 AGCM simulations (1) (after Mitchell 1993) 115
6.2 Experiments using GCMII (PD: present-day) 117
6.3 Annual mean response of the GCMII 123

List of Figures

1.1 Elements of the Earth's orbit (from Berger 1996) 2

2.1 Schematic diagram of energy fluxes in the atmosphere component 14

3.1 Summer (mid-June) insolation anomaly relative to the present at 90°, 60°, and 30°N after Rind et al. (1989), and based on data from Berger (1978). . 36

3.2 Simulated annual mean, present-day, zonally-averaged meridional overturning streamfunction in the Atlantic Ocean (A1). Contour interval is 2 Sv (1 Sv $\equiv 10^6$ m^3 s^{-1}), and counterclockwise circulation is shaded. 39

3.3 Simulated present-day, annual mean, zonally-averaged depth-integrated steric height in the Atlantic Ocean (A1). 41

3.4 Relationship between the meridional contrast in depth-integrated steric height between 30°S and 60°N, and the strength of the meridional overturning in the Atlantic Ocean. 42

3.5 Simulated annual mean, zonally-averaged meridional overturning streamfunction in the Atlantic Ocean. Contour interval is 2 Sv (1 Sv $\equiv 10^6$ m^3 s^{-1}), and counterclockwise circulation is shaded. 44

3.6 Effect of CO_2 on depth-integrated steric height under 11 kaBP and 21 kaBP orbital geometries. In the contribution of the temperature difference, positive value reflects warmer temperature, while negative value reflects colder temperature. In the contribution of the salinity difference, positive value reflects lower salinity while negative value reflects higher salinity. 46

3.7 Difference in annual mean, freshwater fluxes (m/yr) at the surface between 280 ppmv and 200 ppmv CO_2 forcing. 47

3.8 Simulated winter sea ice thickness. Here winter is defined as the period of 30 days following the winter solstice. 48

3.9 The effect of orbital parameters on insolation (W m^{-2}). Contour interval is 10 W m^{-2}, and negative values are dotted. VE, SS, AE, and WS are respectively vernal equinox, summer solstice, autumnal equinox, and winter solstice in the NH. 50

3.10 Simulated annual mean zonally-averaged meridional overturning streamfunction in the Atlantic Ocean. Contour interval is 2 Sv (1 Sv $\equiv 10^6$ m^3 s^{-1}), and counterclockwise circulation is shaded. 51
3.11 Effect of precession and obliquity on depth-integrated steric height. 54
3.12 Effect of precession (A7 minus A6) on the contrast between the annual mean NH and SH responses at the early stage of integration (300 years). 55
3.13 Annual mean insolation at the top of the atmosphere and absorbed shortwave radiation at the surface (300 years). 56
3.14 Difference in annual mean, freshwater fluxes (m/yr) at the surface between A7 and A6. 57
3.15 Simulated winter sea ice thickness. Here the definition of winter is the same as Fig. 3.8. 58

4.1 Model integration procedure. 67
4.2 Flow of moisture between the components of the climate model. 68
4.3 Insolation at the top of the atmosphere relative to the present (W m^{-2}). Contour interval is 5 W m^{-2}, and negative values are dotted. VE, SS, AE, and WS are respectively vernal equinox, summer solstice, autumnal equinox, and winter solstice in the NH. 71
4.4 Simulated annual mean surface air temperature relative to the present-day control simulation. Contour interval is 0.5°C, and negative values are shaded. 73
4.5 Simulated sea surface temperature relative to the present-day control simulation during the NH summer. Contour interval is 1.0°C, and negative values are shaded. Here summer is defined as the period of 30 days following the summer solstice. 74
4.6 Simulated present-day winter sea ice thickness. Here winter is defined as the period of 30 days following the winter solstice. 75
4.7 Simulated annual mean northward heat transport in the Atlantic Ocean (1 PW $\equiv 10^{15}$ W). 76
4.8 Simulated seasonal surface air temperature relative to the present-day control simulation. Contour interval is 1°C, and negative values are shaded. Here the definitions of summer and winter are the same as Figs. 4.5 and 4.6. . . 77
4.9 Simulated seasonal northward heat transport in the Atlantic Ocean relative to the present-day control simulation (1 PW $\equiv 10^{15}$ W). Here the definitions of summer and winter are the same as Figs. 4.5 and 4.6. 78

4.10 Simulated difference in surface air temperature during the NH summer. Contour interval is 0.5°C, and negative values are shaded. Here the definition of summer is the same as Fig. 4.5. 79

4.11 Difference in simulated winter precipitation rate. Here the definition of winter is the same as Fig. 4.6. 80

4.12 Difference in simulated annual mean snowfall rate. 82

4.13 Ice volume evolution (10^{16} m^3) under the present-day forcing in the coupled climate-ice sheet model. 83

4.14 Present-day, simulation using the coupled climate-ice sheet model and observations. 84

4.15 Initial conditions used for the experiments. 86

4.16 Ice sheet response of the coupled climate-ice sheet model to changes in radiative forcing. 87

5.1 Insolation at the top of the atmosphere at 116 kaBP relative to the present (W m^{-2}). Contour interval is 5 W m^{-2}, and negative values are dotted. VE, SS, AE, WS are respectively vernal equinox, summer solstice, autumnal equinox, and winter solstice in the NH. 95

5.2 Subgrid topography over North America. 97

5.3 Distribution of normalised areal fraction with respect to elevation. Histogram in blue represents normalised areal fraction sampled at each meter while that in red represents normalised areal fraction sampled at each subgrid elevation level. Black line represents elevation without any subgrid treatment. 99

5.4 Annual mean net accumulation with the lowest subgrid resolution (M1). . . 104

5.5 Annual mean net accumulation with the highest subgrid resolution (M5). . 105

5.6 Ice thickness at selected subgrid elevation levels in the present-day simulation. 106

5.7 Ice thickness at selected subgrid elevation levels in the 116 kaBP simulation. 107

6.1 Experimental procedures (see text for details). 117

6.2 Differences in sea surface temperature (°C) between 116 kaBP (B2) and present-day (B1) from the coupled climate model simulations. 121

6.3 As in Fig. 6.2 but for differences in sea ice amount. Note that 1 kg m^{-2} is approximately equivalent to 1 mm in ice thickness. 122

6.4 Simulated minus observed surface air temperature (°C). 124

6.5 Net annual snow accumulation rate (kg m^{-2} yr^{-1}). 126

6.6 Annual snow budget (kg m^{-2} yr^{-1}). Data are extracted only over land between 60°W and 120°W (North America except Alaska) and then zonally-averaged. 127

6.7 Difference between 116 kaBP experiments (E3 – E6) and the control run. Data are extracted only over land between 60°W and 120°W and then zonally-averaged. 128

6.8 Difference between the 116 kaBP simulation with simulated 116 kaBP sea surface conditions (E4) and the 116 kaBP simulation with simulated present-day sea surface conditions (E3). Data are extracted only over land between 60°W and 120°W and then zonally-averaged. 130

6.9 Difference in seasonal snow melting rate (kg m^{-2} yr^{-1}) between the 116 kaBP simulation with simulated 116 kaBP sea surface conditions (E4) and the 116 kaBP simulation with simulated present-day sea surface conditions (E3). Data are extracted only over land between 60°W and 120°W and then zonally-averaged. 131

6.10 Difference between E4 and E3 in summer energy budget at the land surface (W m^{-2}). Positive values represents net gain of energy for the surface while negative values represents net loss of energy for the surface. Data are extracted between 60°W and 120°W and then zonally-averaged. 131

6.11 Areas specified as tundra (shaded). 133

6.12 Net annual snow accumulation rate (kg m^{-2} yr^{-1}). 134

6.13 Annual snow budget (kg m^{-2} yr^{-1}). Data are extracted only over land between 60°W and 120°W and then zonally-averaged. 135

6.14 Difference between E6 and E4 in summer energy budget at the land surface (W m^{-2}). Positive values represent net gain of energy for the surface while negative values represent net loss of energy for the surface. Data are extracted between 60°W and 120°W and then zonally-averaged. 136

Acknowledgements

This work has been supported by NSERC (National Science and Engineering Research Council) Operating, Strategic and CSHD (Climate System History and Dynamics) research grants. Funding from the MSC/CICS (Meteorological Service of Canada/Canadian Institute of Climate Studies) is also gratefully acknowledged. Computations are primarily performed on two IBM SP2s partially funded from an IBM SUR grant. I also thank to the CCCma (Canadian Centre for Climate Modelling and Analysis) for allowing me to use their model and computers.

I am enormously thankful to my supervisor, Dr. Andrew Weaver for introducing this fascinating field of paleoclimatology, continuous encouragement, and his other tremendous support, including corrections in the manuscripts and financial support. I enjoyed participating in international conferences and workshops, and giving lectures to undergraduate students. In particular, the PMIP (Paleoclimate Modelling Intercomparison Project) workshop was a great chance to meet international leaders in the community of paleoclimatology. The knowledge gained in the workshop greatly influenced on this thesis. I appreciate him for providing such opportunities as well.

I am grateful to Dr. Shawn Marshall and Dr. Garry Clarke for kindly providing me an ice sheet model as well as their scientific advice. I owe thanks to Dr. Cathy Reader for kindly helping me in using the CCCma model, and Dr. Norm McFarlane for his scientific advice.

I am indebted to Ed Wiebe, Michael Roth, and Daithi Stone for their technical supports and corrections of English in the manuscript. I would like to thank to Dr. Andreas Schmittner for scientific discussions and to Michael Eby for his help in modelling. I would also like to thank all graduate students and post-doctoral fellows in the lab for their friendliness and a comfortable environment.

Chapter 1

Introduction

1.1 Introduction

Climate can be defined as the statistics of weather phenomena. Understanding of the climate system may be attempted by studying present-day and past climates, and the climate on other planets. It is the study of past and present-day climate that provides the basis for prediction of the future. The global scale instrumental record of some weather elements covers only about a century. Therefore, global scale climate changes, other than current global warming, are not instrumentally recorded. For many quantities, the available observational record is unsuitable for the study of climate variability on time scales longer than about a decade. Moreover, the weather of other planets occurs under very extreme environmental conditions and, together with a lack of data, is of little practical use. Fortunately, the Earth itself has been recording climate-related indicators over its history. Paleoclimate proxy records over millions of years, in which the Earth underwent diverse climate states, have been collected. The collected data have been analysed and used to reconstruct the climate states in the past. However, each record is usually acquired separately and the relationships between them are not necessarily obvious. As a result, the suggested mechanisms of climate change are often educated guesswork.

Since numerical experiments can explore the possibilities of suggested mechanisms of climate change, and furthermore since their results can be referenced to the actual paleoenvironmental records, paleoclimate studies using numerical climate models give us valuable insight into the climate system. At the same time, paleoclimate modelling provides an opportunity for testing climate model performance. In this study, modelling is applied to the climate change/transition during the last glacial cycle. There are several reasons for which this period deserves a high priority for investigation: 1) glaciation/deglaciation is one of the most extreme and fundamental paleoclimatic events in the Earth's history; 2) as it is relatively recent on the geological time scale, the paleoenvironmental proxy records are abundant; 3) the land-sea distribution is similar to that of today; and 4) it is a unique period in Earth's history for which external and greenhouse-gas forcing is well known. Particular attention is paid to the importance of external forcing and internal feedback mechanisms.

Throughout this thesis, the experiments are undertaken from the point of view that the Earth's climate is a system consisting of many subsystems interacting with each other in very complicated ways.

1.2 Orbital forcing

The Earth revolves around the Sun in a slightly elliptical orbit, and the plane containing this orbit is called the ecliptic (Berger 1996). The Sun is located at one of the two foci of the ellipse (Fig. 1.1). The seasonal variations of incoming solar radiation at the top of the atmosphere (insolation) today result from the two facts that the Earth's axis of rotation is tilted from the line perpendicular to the plane of the ecliptic ("tilt season"), and that the distance between the Sun and the Earth varies with the Earth's revolution due to the ellipticity of the orbit ("distance season"). For example, when the Earth's axis at the North Pole is tilted toward the Sun (summer solstice), the Northern Hemisphere (NH) experiences stronger solar radiation and longer daylight hours, while the Southern Hemisphere (SH) experiences weaker solar radiation and shorter daylight hours. The opposite conditions apply during the winter solstice. When the position of the Earth is closest to the Sun (perihelion), the Earth receives more solar radiation than it does when the position is furthest from the Sun (aphelion). At present, the "distance season" moderates the dominant "tilt season" in the NH while it reinforces the dominant "tilt season" in the SH (Broecker 1985, fig. 7-10). The Earth's orbital and rotational elements change over time due to the interplay of the gravitational attraction of the masses existing in the solar system.

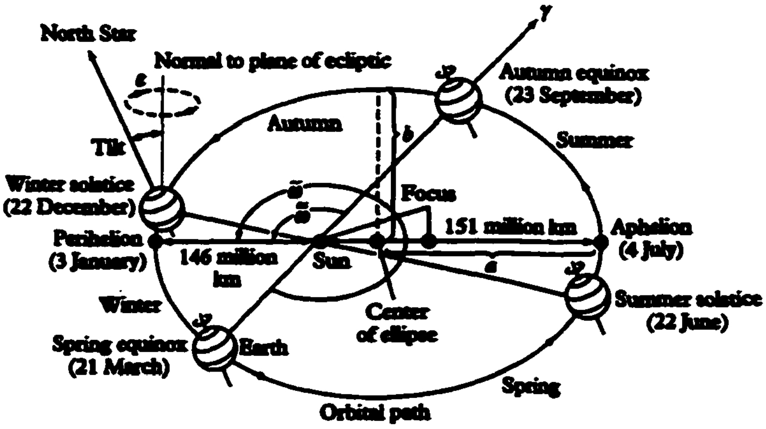

Figure 1.1: **Elements of the Earth's orbit (from Berger 1996)**

Insolation at any given latitude and season (location and time) is uniquely determined by the following five parameters: 1) the solar constant, S_0; 2) the semi-major axis of the orbit, a; 3) the eccentricity of the orbit, e; 4) the obliquity of the ecliptic, ε; and 5) the longitude of the perihelion relative to the moving vernal equinox, ω (Berger 1978; Berger and Loutre 1991). The eccentricity is defined as, $e = \left(a^2 - b^2\right)^{1/2} / a$, where b is the semi-minor axis of the orbit, whereas the obliquity is defined as the angle between a plane passing through the Earth's equator and the plane of the ecliptic, which is equivalent to the angle between the Earth's axis of rotation and the line perpendicular to the plane of the ecliptic. By solving the equations of motion for the planetary and the Earth-Moon systems, long-term variations in orbital and rotational elements are obtained. The solutions by Berger (1978) and Berger and Loutre (1991), for example, are expected to be reliable over the last 1.5 Ma and 5 Ma, respectively. Apart from variations in solar activity, it has been shown that variations in the obliquity, the longitude of perihelion, and the eccentricity are responsible for the major seasonal perturbations of insolation.

The obliquity of the ecliptic, 23.44° at present, has varied between 22.23 and 24.44° over the last 150 ka, and between 22.08° and 24.54° over the last 5 Ma, at a period of about 41 ka (Berger and Loutre 1991). The greater obliquity results in larger insolation at mid and high latitudes in summer hemispheres while it results in smaller insolation at low and mid latitudes in winter hemispheres. Note that high latitudes in winter hemispheres are not affected significantly since they already experience the so-called polar night. Changes in obliquity lead to the latitudinal redistribution of insolation as well as seasonal redistribution. The resulting net gain (loss) of the annual insolation at high latitudes due to increased (decreased) insolation during summer is compensated for by the net loss (gain) of the annual insolation at low latitudes through decreased (increased) insolation during winter, keeping the total amount of annual insolation received by the Earth constant. For reference, the net annual gain at the poles due to increased obliquity can reach about 17 W m^{-2} (Crowley and North 1991, p.132-136).

The variations in the longitude of perihelion relative to the moving vernal equinox at a period of about 22 ka are called the precession of the equinoxes, which results from the axial precession (wobble) and precession of the orbit. The resulting net gain of insolation during the period when the Earth is near perihelion, and hence moves at faster angular velocity, is cancelled by the net loss of insolation during the period when the Earth is near aphelion, and hence moves at slower angular velocity, keeping the annual total amount of insolation received at any given latitude constant. In effect, however, the precession is modulated by eccentricity which splits the precession period of 22 ka into 23 ka and 19 ka (Imbrie and Imbrie 1980). This modulated precession is called the climatic precession and the precession index, $e\sin\omega$, is introduced to describe the combined effect. The precession index, 0.0169 at present, has varied between -0.04180 and 0.04394 over the last 150 ka, and between -0.05625 and 0.05623 over the last 5 Ma (Berger and Loutre 1991). A positive precession index occurs when the perihelion is between vernal and autumnal equinoxes while a negative precession index occurs when the perihelion is between autumnal and vernal equinoxes. The magnitude indicates the difference in length between half-year astronomical seasons (from vernal to autumnal equinoxes, and from autumnal to vernal equinoxes) and the difference between the Earth-Sun distance at both solstices (Berger 1988).

The eccentricity of the orbit, 0.01668 at present, has varied between 0.01409 and 0.04399 over the last 150 ka, and between 0.00027 and 0.05713 over the last 5 Ma, at periods of about 413 ka and 100 ka (Berger and Loutre 1991). Changes in eccentricity, under a constant semi-major axis, alter the total amount of insolation received over the globe each year, through changes in the mean Earth-Sun distance. However, the resulting change is at most 0.2%, or about 0.7 W m^{-2} (Crowley and North 1991, p.132-136). At the same time, as the eccentricity increases, the foci move away from the centre of the ellipse and hence the difference in the Earth-Sun distance at the perihelion and the aphelion increases. As mentioned, this results in a modulation of the precession of the equinoxes and an intensification of the amplitude of the "distance season".

1.3 Glacial-interglacial cycles

Evidence of glaciation is usually given by glacial deposits on the continents, ice-rafted debris in the ocean sediments, and oxygen isotope ratio measurements of calcium carbonate in microfossils (principally foraminifera, but also cocoliths — Bradley 1999, p.199) in the ocean sediments. Since the terrestrial record is eroded by successive glaciations and is also time discontinuous, the marine record is frequently used. Two stable isotopes of oxygen utilised are ^{18}O and ^{16}O, with ^{18}O being heavier than ^{16}O due to two extra neutrons. Note that ^{17}O is too rare to be practically measured. The fractionation occurs through phase change (vaporisation and condensation) such that the lighter oxygen, ^{16}O, is preferentially evaporated from the ocean and the heavier oxygen, ^{18}O, is preferentially precipitated. As moisture is generally transported from low latitudes to high latitudes in the atmosphere, polar ice caps are isotopically lighter than mean ocean water. As ice sheets at high latitudes, depleted in ^{18}O, grow, mean ocean water becomes enriched in ^{18}O. The fractionation also occurs through chemical reaction (water to carbonate) when oxygen is taken up by microfossils. The degree of fractionation is determined by the temperature of the environment, with the heavier isotope being depleted under warmer temperatures. Therefore, the oxygen isotope ratio contains information about the global land ice volume and the local temperature of ocean water. It is, however, generally believed that the oxygen isotope ratio in benthic foraminifera is more indicative of ice volume over the last 2.5 million years as the deep ocean today is already close to the freezing point of seawater (Shackleton 1967). While relative sea level does not respond linearly to continental ice volume due to concurrent variations of oceanic area and thermal expansion of sea water (Marsiat and Berger 1990), it gives an approximate idea of globally-integrated glacial evolution. The confidence in the reconstruction of the global ice volume using the oxygen isotope ratio is given by the comparison with glacio-eustatic sea level changes during the last glacial cycle (e.g., Linsley 1996; Shackleton 1987). They are derived from raised coral reef terraces, assuming a constant rate of local tectonic uplift. The geographical information of glaciation is supplemented by ice-rafted debris and other terrestrial evidence.

The Cenozoic Era, a geologically defined period from 65 MaBP to present (Harland et al. 1990), is characterised by a general trend of cooling (Savin et al. 1975; Barron 1985; Van Zinderen Bakker and Mercer 1986; Wolfe 1994, and also summarised in Kennett 1982; Crowley and North 1991), probably because of decreasing atmospheric CO_2 concentrations (Pearson and Palmer 2000). Along with this cooling, several significant climatic events occurred. For instance, the first major Antarctic glaciation occurred in East Antarctica c.a. 34-42 MaBP (Kennett 1977; 1982; Miller et al. 1987; Robin 1988; Lear et al. 2000, and also summarised in Oglesby 1989). After several advances and retreats, the semi-permanent East Antarctic ice sheet formed c.a. 14-16 MaBP (Kennett 1977; 1982; Miller et al. 1987; Robin 1988; Schnitker 1980; Shackleton and Kennett 1975b; Woodruff et al. 1981; Barron et al. 1991; Ehrmann and Mackensen 1992, and also summarised in Oglesby 1989). The onset of Greenland glaciation occurred c.a. 8-10 MaBP (Jansen et al. 1990; Larsen et al. 1994). The first continental-scale NH glaciation initiated c.a. 2.75 MaBP (Curry 1966; McDougall and Wensink 1966; Stipp et al. 1967; Berggren 1972; Shackleton et al. 1984; Shackleton and Kennett 1975a; Shackleton and Opdyke 1977; Keigwin and Thunell 1979; Poore 1981; Raymo 1994; Tiedemann et al. 1994) with European glaciation c.a. 2.57 MaBP (Jansen and Sjøholm 1991).

Thereafter, NH ice sheets repeatedly advanced and retreated at a dominant period of 41 ka until around 0.9 MaBP, and then with much larger amplitude at a dominant period of 100 ka until today (Imbrie et al. 1993). Marine isotope stages, assigned by fluctuations in the oxygen isotope ratio, exceed a hundred (Cronin 1999, p.158).

To explain the waxing and waning of ice sheets, or so-called glacial-interglacial cycles, various hypotheses have been considered (e.g., Ewing and Donn 1956; 1958; Donn and Ewing 1966; Wyle 1968; Worthington 1968; Newell 1974 and also summarised in Imbrie and Imbrie 1980). The astronomical theory, which links glacial-interglacial cycles to orbitally-driven changes in insolation (orbital forcing), was introduced by Joseph Alphonse Adhémar in 1842 (Imbrie and Imbrie 1979; Berger 1988). Some scientists, including James Croll in 1875, considered winter to be the critical (control) season (Imbrie and Imbrie 1979; Berger 1988). However, this idea was not accepted because it is always cold during winter at the very high latitudes where ice sheets most likely nucleate, and also insolation changes little in the winter due to the polar night (Ruddiman 2001). On the other hand, other scientists, including Milutin Milankovitch in 1938, consider summer to be the critical season as it is the time when significant melting occurs (Imbrie and Imbrie 1979; Berger 1988). Note that this particular version of the astronomical theory, with emphasis on insolation at 65°N, is called Milankovitch theory.

Seeking the origin of the glacial-interglacial cycles, global ice volume records have been intensively studied in the time and the frequency domains (e.g., Berger et al. 1991; Hays et al. 1976; Imbrie et al. 1992; 1993; 1984), and in the frequency-time domain (e.g., Bolton et al. 1995; Liu and Chao 1998) over the last three decades. It has been shown that these records persistently contain spectral peaks at periods of about 23 ka and more dominantly at about 41 ka before around 0.9 MaBP, and thereafter at periods of about 23 ka, 41 ka, and, most dominantly, 100 ka. The three periods of 23 ka, 41 ka and 100 ka correspond to that of orbital eccentricity, obliquity, and climatic precession, respectively, with high coherencies. As a result, fluctuations in orbital forcing have been widely recognised as the primary triggers responsible for the glacial-interglacial cycles.

It has been shown that the amplitude and phase of the global ice volume in the 23 ka and 41 ka bands can be explained as a simple linear response to variations in the NH summer insolation driven by the precession of the equinoxes and by obliquity, respectively (Imbrie and Imbrie 1980; Imbrie et al. 1992). The larger gain in the 41 ka band than in the 23 ka band is explained by the difference of the period, that is, a longer time is available to build ice under forcing with longer periodicity. On the other hand, the response of the global ice volume in the 100 ka band produces several paradoxes which cannot be explained by a simple linear theory (100 ka problem). For example: 1) ice volume varies in time in a sawtooth pattern under sinusoidal (symmetric) variations of orbital eccentricity; 2) the amplitude of the 100 ka insolation cycle is too small to explain the observed ice volume; 3) the phase of the 100 ka insolation cycle is too delayed to explain the observed ice volume; 4) there is an increasing trend in the amplitude of the 100 ka cycle in ice volume while the orbital eccentricity shows a decreasing trend; and 5) the recorded dominant cycle in ice volume shifts from the 41 ka obliquity band to the 100 ka eccentricity band at about 0.9 MaBP (Imbrie et al. 1993). There are presently two hypothesis that explain 4) and 5): Orbital forcing is superimposed on the background trend of cooling due to decreasing atmospheric CO_2 concentration on the tectonic time scale. This cooling gradually raises the threshold of orbital forcing (summer insolation) that is required for ice sheets to decay. (Raymo 1997; Paillard 1998). On the other hand, ice sheets slowly erode landscapes and strip soil cover (deformable "soft" bed) which facilitates basal sliding of ice when the soils are saturated with water. After successive glaciations, only undeformable "hard" bed remains, which allows for ice sheets to grow thicker without intruding into warmer latitudes (Clark and Pollard 1998). Both mechanisms result in longer characteristic time scales for glacial-interglacial cycles. In any case, 1)–3) remain to be explained satisfactorily.

It is extremely difficult to consider physically plausible models of linear resonance in which the climate system is only, and extremely, sensitive to forcing in the 100 ka eccentricity band (Imbrie and Imbrie 1980). Furthermore, evoking alternate simple models which are only sensitive to one side of the envelope of 23 ka cycle of climatic precession (rectification models) only produces additional complexities. These include the so-called 400 ka problem in which ice volume does not show a spectral peak at the 413 ka eccentricity band, and the stage 11 problem (but probably stage 1 as well although it is incomplete) in which ice volume displays a similar amplitude of response even when the amplitude of orbital eccentricity is small (Howard 1997; Imbrie and Imbrie 1980; Imbrie et al. 1993). Clearly, the global ice volume record cannot be explained only by orbital forcing. Indeed, many nonlinear models, which reproduce a dominant 100 ka ice volume cycle, rely on some sort of internal mechanism in the climate system, such as ice dynamics with delayed bedrock response and changes in ocean circulation and atmospheric CO_2 concentration (Saltzman 1990).

1.4 Role of ocean and atmospheric CO_2 concentration

Orbital cycles are engraved in numerous other proxy records as well as in global ice volume records (Cronin 1999, 149-185). Synthesising these records, Broecker et al. (1985) and Broecker and Denton (1989) proposed the occurrence of a major reorganisation of the ocean-atmosphere system during glacial-interglacial transitions. Particularly important are changes in the thermohaline circulation, which may also cause changes in atmospheric concentrations of greenhouse gases. Imbrie et al. (1992; 1993) investigated the phase relationship between ice volume and many other diverse and geographically widespread (yet marine-biased) proxy records, known as the SPECMAP (see Glossary of Acronyms). The results revealed that these proxies are separated into two groups: an early response group that leads ice volume, and a late response group that lags ice volume. The early response group consists of proxies related to deep ocean circulation in the Atlantic Ocean and atmospheric CO_2 concentration, whereas the late response group consists of proxies related to NH climate, such as sea surface temperature (SST) in the North Atlantic, the mass of terrestrial biosphere, and continental aridity in China and Arabia. Another study has shown that European vegetation also belongs to the late response group (Ruddiman 2001). The late response group is considered to be the response to the build-up of significant NH ice masses, rather than a direct response to insolation, considering its response time. This interpretation is consistent with the LGM simulation by Manabe and Broccoli (1985) in which cooler SST in the North Atlantic is caused by existence of large ice sheets and the influence of ice sheets is confined within the NH. Other responses in this group may, in turn, be explained by the response to cooler SST in the North Atlantic (Pinot et al. 1999; Rind et al. 1986).

The existence of an early response group suggests that changes in ocean circulation and atmospheric CO_2 play important roles in glacial-interglacial cycles. Recently, Shackleton (2000) independently refined the ages of ocean sediment and gases trapped in ice cores with orbital tuning. He also separated the contribution of ice volume and the contribution of ocean temperature to the oxygen isotope ratio in ocean sediment by using the record of the isotope ratio in atmospheric oxygen trapped in the ice core. As a result, it was concluded that NH summer insolation, deep water temperature, surface air temperature (SAT) in Antarctica, and atmospheric CO_2 concentrations are in phase and lead ice volume, implying the attribution of the 100 ka cycle to another component of the climate system such as global carbon cycle, rather than ice sheet dynamics. Moreover, it was shown that the amplitude of the ice volume cycle at the 100 ka band is similar or even smaller than at the 41 ka band.

When proxies other than ice volume are considered, another paradox arises which should be added to the list in the previous section: 6) hemispherically synchronous climate change accompanies hemispherically asynchronous insolation changes (Alley and Clark 1999; Broecker and Denton 1989; Guilderson et al. 1994; Lowell et al. 1995). In the proposed process model of Imbrie et al. (1992; 1993), the thermohaline circulation and atmospheric CO_2 concentration links climate between the two hemispheres. This role of CO_2 is consistent with the model simulation of Broccoli and Manabe (1987) in that atmospheric CO_2

concentration equally affects both hemispheres, although the thermohaline circulation likely affects both hemispheres asymmetrically (Crowley 1992).

Synthesising, cross-spectral analysis suggests an important role of ocean circulation and atmospheric CO_2 concentration during the glacial-interglacial cycles. The questions to be addressed in this thesis are: which components of the climate system play important roles during the glacial-interglacial cycles, and to what extent? Are they interacting with each other? These are important steps towards the ultimate questions of how glaciation started and ended, which remain largely unanswered after more than a century.

1.5 Paleoclimate modelling

Efforts have been made towards the establishment of models that reproduce the observed global ice volume records (summarised in Berger 1988; Imbrie et al. 1993; Saltzman 1990). In addition to zero-dimensional models (e.g., Imbrie and Imbrie 1980; Paillard 1998), zonally-averaged ice sheet models driven by meridional shift of equilibrium line which corresponds to changes in summer insolation (e.g., Birchfield et al. 1981; Budd and Smith 1981; Hyde and Peltier 1985; 1987; Oerlemans 1980; 1981b;a; 1982; Pollard 1982; Weertman 1976), and zonally-averaged ice sheet models coupled to zonally-averaged energy balance atmosphere models (e.g., Birchfield et al. 1982; Pollard 1978; 1983; Steen and Ledley 1997) have been extensively used. These studies have investigated some important feedback mechanisms, such as the ice albedo feedback, the ice elevation feedback (it becomes colder as the ice sheet grows higher), the elevation-desert effect (it becomes drier as the ice sheet grows higher), and the vertical displacement of bedrock due to glacio-isostatic adjustment. The delay of the bedrock response to changes in imposed ice load keeps the ice surface at low elevation after removal of significant ice masses. This process likely contributes to the rapid terminations, which is a crucial element of the 100 ka ice volume cycle. Note that although the importance of iceberg calving and basal sliding have also been pointed out, quantification of such mechanisms is extremely difficult. As mentioned earlier, these studies produced great insight into the behaviour of the Earth as a dynamical system. However, uncertainties remain due to their idealised climatologies.

Neeman et al. (1988a;b) coupled a two-dimensional ice sheet model to a zonally-averaged statistical-dynamical atmosphere model, whereas Gallée et al. (1991; 1992) coupled a zonally-averaged ice sheet model to a two-dimensional, two-level, quasi-geostrophic atmosphere model. Although the atmospheric components of these models are more sophisticated than simple energy balance models, the limitation exists that neither the climate nor the ice sheets were purely zonal phenomena. Andrews (1997) warns against focusing only on the areally "integrated responses". The purpose here, however, is not to cast doubt on the orbital theory, which has its foundation in the globally integrated ice volume record. Rather, it is to emphasise the importance of taking into account the inherent two-dimensionality of the processes. This recognition will become more crucial when interactions between components of the climate system and feedback mechanisms in the climate system are studied.

With respect to higher dimensional climate models, there are generally two approaches used in their integration: 1) long-term, time-evolving forcing with computationally inexpensive models (e.g., Deblonde and Peltier 1990; 1991; 1993; Peltier and Marshall 1995; Short et al. 1991; Tarasov and Peltier 1997a); and 2) perpetual forcing to equilibrium with expensive, but more complicated and physically-based, models (summarised in Mitchell 1993). Although the former approach has the advantage that the models can be integrated over a whole glacial cycle, the role of the hydrological cycle, ocean circulation, and sea ice as feedback mechanisms are usually not considered.

It is known that the LGM climate simulated using an AGCM is sensitive to prescribed sea surface conditions (Bard 1999; Hostetler and Mix 1999; Marsiat and Valdes 2001; Pinot et al. 1999; Rind and Peteet 1985; Webb et al. 1997), as is the Younger Dryas climate (Rind et al. 1986). Therefore, the sensitivity of a model to different forcing from today is probably underestimated when present-day sea surface conditions are applied. To obtain a realistic present-day climate, a coupled AGCM-mixed layer ocean model requires specification of oceanic horizontal heat fluxes. This requirement is removed in fully coupled atmosphere-ocean general circulation models (GCMs), but such coupled models usually require surface flux adjustments to ensure realistic present-day climate simulations. The validity of such flux adjustments in simulating climates largely perturbed from the present is questionable (Manabe 1989; Marotzke and Stone 1995; Fanning and Weaver 1997b). In this thesis, the global climate model that is primarily used consists of an energy-moisture balance atmosphere model, an OGCM, and a dynamic-thermodynamic sea ice model, without flux adjustments. The strength of the climate model is the detailed physics of the ocean component. It is, therefore, suitable for the study of processes involving ocean circulation. An ice sheet model and AGCM are also used when they are necessary to resolve processes not captured by the climate model.

The outline of the rest of the thesis is as follows: In the next chapter, the three models used in this thesis are described; that is the coupled climate (atmosphere-ocean-sea ice) model, the ice sheet model, and the AGCM. In Chapter 3, the response of thermohaline circulation to changes in atmospheric CO_2 concentration and orbital geometry during the last deglaciation is investigated using the coupled climate model. Experiments are conducted under four different sets of perpetual, radiative forcing; that is, two different orbital geometries (11 kaBP and 21 kaBP) and two different atmospheric CO_2 concentrations (280 ppmv and 200 ppmv). The ice sheet model is globally and asynchronously coupled to the climate model in Chapter 4. The response of ice sheets to changes in the atmospheric CO_2 concentration and orbital geometry during the last deglaciation is investigated using the coupled climate-ice sheet model. The same sets of perpetual radiative forcing are used as in Chapter 3 to study the relative importance of orbital and CO_2 forcing for the mass balance of the ice sheet in glacial termination. In Chapter 5, the importance of subgrid-scale topography in simulating the last glacial inception is investigated using the coupled climate model. The effect of subgrid-scale topography is incorporated in two different ways. In the first approach, the effect of subgrid elevation is emphasised while subgrid ice-flow is also included in the second approach. In Chapter 6, the importance of the lower boundary conditions (SST, sea ice distribution, and vegetation) in simulating the last glacial inception is investigated using the AGCM. The sea surface conditions used to drive the AGCM are obtained from the simulations of the coupled climate model. Studies regarding the last glacial termination in Chapter 3 and 4, and the last glacial inception in Chapter 5 and 6 are followed by conclusions in Chapter 7.

Chapter 2

Model descriptions

In this chapter the three models used in this thesis are described: the coupled climate model, the ice sheet model, and the AGCM. The first model is used throughout the thesis, i.e., in Chapters 3–6, the second model coupled to the first model in Chapter 4, and the third model in Chapter 6. All models are described here in a spherical coordinate system, (λ, ϕ, z), where λ is longitude increasing eastward with zero defined at an arbitrary longitude, ϕ is latitude increasing northward with zero defined at the equator, and z is the vertical coordinate increasing upward with zero defined at the surface of a resting ocean. As in the conventional geophysical fluid dynamics, u, v, and w represent longitudinal (zonal), latitudinal (meridional), and vertical component of velocity, respectively.

2.1 The coupled climate model

The coupled climate model consists of three components: atmosphere, ocean, and sea ice. All components cover the whole global area with horizontal resolution of 3.6° and 1.8° in longitude and latitude, respectively. The model resolves the annual cycle and is designed to simulate climates under various forcing, with particular emphasis on the processes involving ocean circulation. This has been achieved by explicitly calculating heat and freshwater fluxes, instead of using conventional mixed boundary conditions in driving the OGCM (Fanning and Weaver 1996). Indeed, the model has been shown to be useful for studies of climates greatly perturbed from that of the present-day, including paleoclimate applications (Murdock et al. 1997; Poussart et al. 1999; Weaver et al. 1998). This is due to the fact that the model does not require flux adjustments. The comprehensive description of the nearly identical model and its various applications including both the present-day and LGM equilibrium climates, as well as global warming simulations is given in Weaver et al. (2001).

2.1.1 The atmosphere component

The atmosphere component of the coupled model is based on the two-dimensional energy-moisture balance model (EMBM) of Fanning and Weaver (1996). It is a relatively simple model based on the vertically-integrated thermodynamic energy and moisture balance equations. Sea level air temperature (T_a) and specific humidity (q_a) are its two prognostic variables. An eddy diffusion parameterisation is employed to represent net horizontal transport of heat and moisture. As described below, some important feedback mechanisms are incorporated such as the ice-albedo feedback and the water vapour feedback on outgoing longwave radiation. Orography is felt by the atmosphere through SAT in calculating outgoing longwave radiation, saturation specific humidity, threshold temperature between snow and rain, snow melting rate, and albedo. One of the strengths of the EMBM is its inexpensive computational cost due to its simplified physics, while its main weakness lies in the lack of an explicit calculation of atmospheric dynamics.

Energy balance equation

The EMBM assumes an exponentially-decaying vertical thermodynamic profile:

$$\rho(z)\,T(z) = \rho_a T_a \exp\left(-z/H_t\right) \tag{2.1}$$

where ρ and T are respectively the density and temperature of the air at height z, and H_t is a constant scale height for pressure (e-folding height for air pressure relative to the surface) chosen to be 8.4 km as in Gill (1982). The vertically-integrated thermodynamic energy balance equation is expressed as

$$\rho_a H_t C_{pa} \frac{\partial T_a}{\partial t} = Q_{HT} + Q_{SSW} - Q_{OLW} + Q_{LW} + Q_{SH} + Q_{LH}^{P} - Q_{LH}^{M} \tag{2.2}$$

where $C_{pa} = 1004$ J kg^{-1} K^{-1} is the specific heat of air at constant pressure. On the right hand side, Q_{HT} is the net horizontal heat transport, Q_{SSW} the shortwave radiation absorbed by the atmosphere, Q_{OLW} the outgoing longwave radiation, Q_{LW} the net upward longwave radiation at the surface, Q_{SH} the surface sensible heat flux, Q_{LH}^{P} the latent heat release associated with precipitation, and Q_{LH}^{M} the latent heat consumption associated with snow melting over land (Fig. 2.1).

The net horizontal heat transport is parameterised as an eddy diffusion:

$$Q_{HT} = \rho_a H_t C_{pa} \nabla_h \cdot (\nu \nabla_h T_a)$$

where ∇_h is a two-dimensional horizontal gradient operator, and ν is a latitude-dependent horizontal eddy diffusivity coefficient for heat, representing large scale heat transport processes in the atmosphere. The order of this coefficient ($\sim 10^6$ m^2 s^{-1}) is much larger than

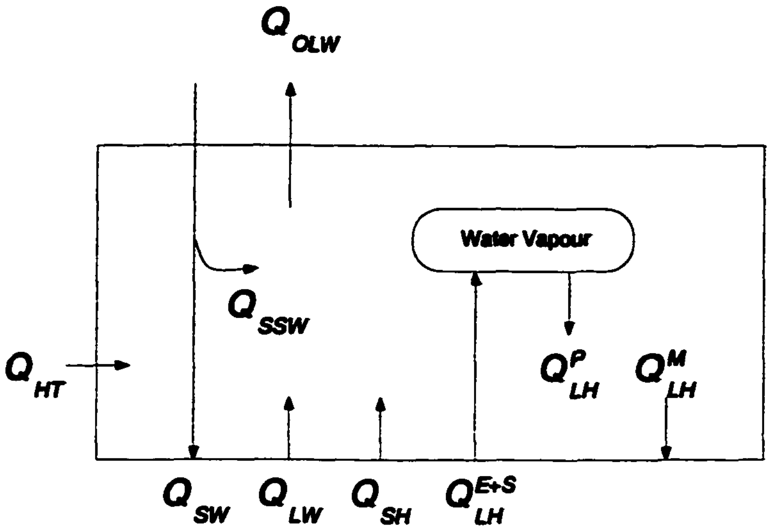

Figure 2.1: **Schematic diagram of energy fluxes in the atmosphere component**

that of the molecular diffusion ($\sim 10^{-5}$ m^2 s^{-1}) so that the latter effect is negligible (Fanning and Weaver 1996 and Kundu 1990, p.481).

The shortwave radiation absorbed by the atmosphere, Q_{SSW}, is treated as a source term using a planetary albedo, α. By the definition of planetary albedo, the total shortwave radiation absorbed by the planet Earth, Q_{TSW}, is written as

$$Q_{TSW} = \frac{S_0}{4} S \,(1 - \alpha) \tag{2.3}$$

where S_0 = 1368 W m^{-2} is the solar constant (obtained from observations), and S the latitude-dependent annual distribution of insolation at the top of the atmosphere (calculated from the formula by Berger 1978). To represent the shortwave absorption processes in the atmosphere by water vapour, dust, ozone, and clouds, a constant absorption parameter, $C_a = 0.3$, is introduced. This parameter determines the fraction of energy absorbed by the atmosphere and the surface such that 30% of the total shortwave radiation absorbed by the planet Earth is always absorbed by the atmosphere and the rest is absorbed by the surface. Therefore,

$$Q_{SSW} = C_a Q_{TSW}. \tag{2.4}$$

An ice-albedo feedback is incorporated into the model by locally changing the planetary albedo:

$$\alpha = \begin{cases} \alpha_0 & \text{if ice-free} \\ \alpha_0 + \Delta\alpha & \text{otherwise} \end{cases} \tag{2.5}$$

where α_0 is the observed, latitude-dependent, monthly mean planetary albedo under average-cloudiness skies (Graves et al. 1993). The increase of planetary albedo, $\Delta\alpha$, due to the presence of sea ice is parameterised as a function of ice thickness, H_i:

$$\Delta\alpha = \begin{cases} \max(0, \Delta\alpha_0 + 0.1 \ln H_i) & \text{if } H_i < 1\text{m} \\ \Delta\alpha_0 & \text{otherwise} \end{cases}, \tag{2.6}$$

while due to the presence of snow over land it is simply:

$$\Delta\alpha = \Delta\alpha_0, \tag{2.7}$$

where $\Delta\alpha_0 = 0.18$ is termed the albedo jump. Note that possible changes in α due to clouds are ignored.

The parameterisation of the outgoing longwave radiation is based on Thompson and Warren (1982), in which the effect of changes in amount of atmospheric water vapour is included. The radiative forcing associated with changes in atmospheric CO_2 concentration is also implemented. As a result, the outgoing longwave radiation, Q_{OLW}, is evaluated as a function of SAT (T_a^*), relative humidity (r), and the atmospheric CO_2 concentration:

$$Q_{OLW} = a_0 + a_1 T_a^* + a_2 T_a^{*2} + a_3 T_a^{*3} - \Delta F \tag{2.8}$$

and

$$a_n = b_{0n} + b_{1n} r + b_{2n} r^2 \tag{2.9}$$

where $n = 0, 1, 2, 3$, and b_{mn} ($m = 0, 1, 2$) are empirically derived constants given by Thompson and Warren (1982), and ΔF is a perturbation to the radiative forcing due to a departure of CO_2 from its present value of 350 ppmv. Note that this treatment neglects the second-order effect of overlapping H_2O and CO_2 absorption bands. The SAT (T_a^*) is calculated from the sea level air temperature (T_a) with a realistic topography and a constant lapse rate of 6.5°C km^{-1}. ΔF at the concentration of C is calculated as follows:

$$\Delta F = \frac{\Delta F_{2\times}}{\ln 2} \ln \frac{C}{C_0} \tag{2.10}$$

where $C_0 = 350$ ppmv is the present-day CO_2 concentration, and $\Delta F_{2\times} = 4$ W m^{-2} is the radiative forcing at a doubling of atmospheric CO_2 (Ramanathan et al. 1987). The equilibrium response of the coupled climate model for CO_2 doubling is a 3°C increase in global mean SAT, so that the model climate sensitivity is 0.75°C W^{-1} m^2 (Weaver et al. 2001).

Net upward longwave radiation at the surface is given by the sum of the upward longwave radiation emitted by the surface and the downward longwave radiation emitted by the atmosphere.

$$Q_{LW} = \begin{cases} \varepsilon_o \sigma T_o^4 - \varepsilon_a \sigma T_a^4 & \text{if over open ocean} \\ \varepsilon_i \sigma T_i^4 - \varepsilon_a \sigma T_a^4 & \text{if over sea ice} \\ Q_{SW} & \text{otherwise} \end{cases} \tag{2.11}$$

where ε_a, ε_o and ε_i are emissivity of the atmosphere, ocean, and sea ice, respectively. Over land, all shortwave radiation intercepted is assumed to return to the atmosphere via black body radiation, and hence

$$Q_{SW} = (1 - C_a)\, Q_{TSW}. \tag{2.12}$$

Note that the energy balance equation over land is, therefore, independent of the value of the absorption parameter C_a.

Sensible heat flux is calculated from the following bulk formula:

$$Q_{SH} = \begin{cases} \rho_a C_H C_{pa} U (T_o - T_a) & \text{if over open ocean} \\ \rho_a C_H C_{pa} U (T_i - T_a) & \text{if over sea ice} \\ 0 & \text{otherwise} \end{cases} \tag{2.13}$$

where $C_H = 0.94 C_E$ is the Stanton number (Isemer et al. 1989) and C_E is the time-dependent Dalton number (Eq. 18 of Fanning and Weaver 1996), and U is the surface wind speed. Setting the sensible heat flux zero over land in conjunction with Eq. 2.11 is consistent with the assumption of no heat capacity for the land surface.

Latent heating is expressed as

$$Q_{LH}^P = \rho_o L_s P_s + \rho_o L_v P_r \tag{2.14}$$

and

$$Q^M_{LH} = \rho_o L_f S_m \tag{2.15}$$

where ρ_o is a representative density of water, P_s is snowfall, P_r is rain, and S_m is the water equivalent surface melting of snow over land, and L_s, L_v, and L_f are the latent heat of sublimation, vaporisation, and fusion for water, respectively.

In each grid cell, snow/ice cover is expressed by areal fraction. For sea ice, the areal fraction (compactness) is introduced to express the existence of numerous ice floes with a variety of ice thicknesses, smaller pieces of sea ice, polynyas and leads on sub-grid scale in nature, which cannot be treated individually. The formulation of this for sea ice is given in the description of sea ice component (see below). Similarly over land, to model the masking effect by terrestrial plants and other objects, and nonuniform distribution of snow caused by wind sweep, the areal fraction, A, is parameterised as a function of snow thickness (H_s) and SAT:

$$A = \begin{cases} \max\left(H_s, (T_a^* - T_s) / (T_e - T_s)\right) & \text{if } H_s < 1 \text{ m or } T_e < T_a^* < T_s \\ 1 & \text{otherwise} \end{cases} \tag{2.16}$$

where T_e and T_s are set to be -10°C and -5°C, respectively.

Moisture balance equation

Similar to the energy balance equation, the vertically integrated moisture balance equation is expressed as

$$\rho_a H_q \frac{\partial q_a}{\partial t} = M_{HT} + M_{VT} \tag{2.17}$$

where H_q is a scale height for specific humidity chosen to be 1.8 km as in Gill (1982), and M_{HT} and M_{VT} are net horizontal transport of moisture and vertical flux of moisture at the surface, respectively.

The net horizontal moisture transport is parameterised by an eddy diffusion:

$$M_{HT} = \rho_a H_q \nabla_H \cdot (\kappa \nabla_H q_a) \tag{2.18}$$

where κ is a latitude-dependent, horizontal eddy diffusivity coefficient for moisture. Again, in the presence of eddy diffusion, the effect of molecular diffusion is negligible.

The vertical flux of moisture is expressed as

$$M_{VT} = \rho_o (E + S - P) \tag{2.19}$$

where E, S and P are the rate of evaporation, sublimation and precipitation, respectively. Evaporation and sublimation are calculated from the following bulk formula:

$$E = \begin{cases} \rho_a C_E U \Delta q(T_o)/\rho_o & \text{if over open ocean and } \Delta q > 0 \\ 0 & \text{otherwise} \end{cases} \tag{2.20}$$

$$S = \begin{cases} \rho_a C_E U \Delta q(T_i)/\rho_o & \text{if over sea ice and } \Delta q > 0 \\ 0 & \text{otherwise} \end{cases} \tag{2.21}$$

where $\Delta q(T) \equiv q_s(T) - q_a$ and $q_s(T)$ is the saturation specific humidity at temperature T (calculated from the empirical formula of Bolton 1980 based on the Clausius-Clapeyron equation).

Precipitation occurs whenever the relative humidity exceeds 85%:

$$P = \frac{\rho_a H_q}{\rho_o \Delta t} \delta(r) \left(q_a - 0.85 q_s(T_a^*)\right) \tag{2.22}$$

where Δt is the EMBM time step, and

$$\delta(r) = \begin{cases} 1 & \text{if } r > 0.85 \\ 0 & \text{otherwise} \end{cases} . \tag{2.23}$$

Precipitation falls as snow over land and sea ice if the SAT is below -5°C, and rain otherwise. The maximum allowable snow thickness before turning to runoff is set at a limit of 10 m. Rain is instantaneously drained into the ocean as runoff according to a realistic predetermined river basin map (Weaver et al. 2001). The melting rate of snow over land is a function of SAT, such that when the SAT rises above -5°C, snow starts melting at the rate of 0.5 cm $°\mathrm{C}^{-1}$ day^{-1} in water equivalent, and the meltwater is instantaneously drained into the ocean. The justification for the use of this threshold value comes from the lack of a diurnal cycle in the model. For example, under daily mean temperature of 0°C, large amounts of snow can melt during daytime while snowfall during night time is limited to the amounts of precipitation, resulting in a negative mass balance in reality. Therefore, zero mass balance should occur below the freezing point in terms of daily mean temperature. Note that the -10°C isotherm has been traditionally used to represent an equilibrium line in models without annual cycle (e.g., Budyko 1969; Oerlemans 1991).

2.1.2 The ocean component

The ocean component of the coupled model is the NOAA-GFDL (see Glossary of Acronyms) Modular Ocean Model version 2 — MOM2 (Pacanowski 1996). It is a three-dimensional primitive equation ocean general circulation model (OGCM) with 19 vertical levels, in which the Boussinesq approximation and the hydrostatic approximation are employed. The ocean is driven by the heat and freshwater (salt) fluxes predicted by the atmosphere and sea ice components, as well as a prescribed monthly wind stress. The energy flux is calculated from radiative transfer, sensible heat flux, and latent heat flux through evaporation. The salt flux is calculated from precipitation, evaporation, runoff, brine rejection occurring in sea ice formation, and melting of sea ice.

Mass balance equation

Under the Boussinesq approximation, the equation for the conservation of mass becomes

$$\nabla \cdot \mathbf{v} = 0. \tag{2.24}$$

Under the hydrostatic approximation, the vertical velocity is diagnosed from the continuity equation.

The boundary condition at the surface is given by

$$w = 0 \quad \text{at} \quad z = 0 \tag{2.25}$$

and the boundary condition at the bottom is given by

$$w = 0 \quad \text{at} \quad z = -H \tag{2.26}$$

where H is the ocean depth. Equation (2.25) is known as the rigid-lid approximation, in which the external gravity waves are filtered out for computational efficiency.

Equations of motion

Under the Boussinesq approximation, the local density (ρ) is replaced by a constant representative density of seawater ($\rho_o = 1035$ kg m^{-3}) except when it is coupled to the gravitational acceleration in the buoyancy force term. To parameterise the exchange of momentum through subgrid-scale mixing, Reynolds stress, arising from the time-averaging of the momentum equations, are assumed to be proportional to the spatial gradients of the large scale (grid scale) velocity. Constant eddy viscosity coefficients are used both in the horizontal ($A_h = 2.0 \times 10^5$ m^2 s^{-1}) and vertical ($A_v = 1.0 \times 10^{-5}$ m^2 s^{-1}) directions. The horizontal component of the momentum equation becomes:

$$\frac{D\mathbf{v}_h}{Dt} + f(\mathbf{k} \times \mathbf{v})_h = -\frac{1}{\rho_o}\nabla_h p + \nabla_h \cdot (A_h \nabla_h \mathbf{v}_h) + \frac{\partial}{\partial z}\left(A_v \frac{\partial \mathbf{v}_h}{\partial z}\right) \tag{2.27}$$

where $\mathbf{v}_h = (u, v)$ is the horizontal velocity, f is the Coriolis parameter, p is the pressure, and

$$\frac{D}{Dt} = \frac{\partial}{\partial t} + \mathbf{v}_h \cdot \nabla_h. \tag{2.28}$$

Under the hydrostatic approximation, a vertical component of momentum equation becomes

$$\frac{\partial p}{\partial z} = -g\rho \tag{2.29}$$

where $g = 9.81$ m s^{-2} is the gravitational acceleration.

A number of conditions need to be prescribed at the boundaries of the ocean, that is, the ocean surface, the ocean floor, and along coastlines. The boundary conditions at the surface ($z = 0$) are expressed as

$$\rho_o A_v \frac{\partial \mathbf{v}_h}{\partial z} = \boldsymbol{\tau}_a \tag{2.30}$$

where $\boldsymbol{\tau}_a = \left(\tau_a^\lambda, \tau_a^\phi\right)$ is the horizontal stress vector at the surface. The exerted surface stress is taken from the reanalysis of observational data (Kalnay et al. 1996). The boundary conditions at the bottom ($z = -H$) are expressed as

$$\rho_o A_v \frac{\partial \mathbf{v}_h}{\partial z} = \boldsymbol{\tau}_b \tag{2.31}$$

where $\boldsymbol{\tau}_b = \left(\tau_b^\lambda, \tau_b^\phi\right)$ is the horizontal stress vector at the bottom. The exerted bottom stress is calculated from

$$\boldsymbol{\tau}_b = \rho_o C_{DB} \left|\mathbf{v}_h^b\right| \mathbf{v}_h^b \tag{2.32}$$

where $C_{DB} = 1.3 \times 10^{-3}$ is the dimensionless drag coefficient at the bottom, and $\mathbf{v}_h^b$ is approximated as the velocity at the first depth level from the bottom. The boundary conditions at the sidewall are given by

$$\mathbf{v}_h \cdot \mathbf{n} = 0, \quad \mathbf{v}_h \cdot \mathbf{t} = 0 \tag{2.33}$$

where **n** and **t** are unit vectors normal and tangent to the sidewall (no-slip boundary condition).

Equations for tracers

To parameterise exchange of tracers, potential temperature (θ) and salinity (S), through subgrid-scale mixing, a constant horizontal eddy diffusion coefficient ($k_h = 2.0 \times 10^3$ m^2 s^{-1}), and a depth-dependent vertical eddy diffusion coefficient are used. The vertical diffusion coefficient is modified from Bryan and Lewis (1979) and it varies from 0.6×10^{-4} m^2 s^{-1} in the thermocline to 1.6×10^{-4} m^2 s^{-1} in the deep ocean:

$$k_v = 10^{-4}\left\{1.1 + \frac{1.05}{\pi}\arctan\left[4.5 \times 10^{-3}(z - 2500)\right]\right\}. \tag{2.34}$$

The conservation equations for tracers are

$$\frac{D\theta}{Dt} = \nabla_h \cdot (k_h \nabla_h \theta) + \frac{\partial}{\partial z}\left(k_v \frac{\partial \theta}{\partial z}\right), \tag{2.35}$$

$$\frac{DS}{Dt} = \nabla_h \cdot (k_h \nabla_h S) + \frac{\partial}{\partial z}\left(k_v \frac{\partial S}{\partial z}\right). \tag{2.36}$$

Due to their subgrid horizontal scale and the use of the hydrostatic approximation, vertical convective processes are parameterised using the Rahmstorf (1993) convective scheme. As such, tracers in statically (gravitationally) unstable cells in the water column are explicitly mixed together, and all instabilities are removed completely within each time step.

The boundary conditions at the surface are expressed as

$$\rho_o C_{po} k_v \frac{\partial \theta}{\partial z} = Q_\theta \tag{2.37}$$

$$\rho_o k_v \frac{\partial S}{\partial z} = M_s \tag{2.38}$$

with

$$Q_\theta = \begin{cases} Q_{SW} - Q_{SH} - Q_{LW} - Q_{LH}^E & \text{if ice-free} \\ Q_b & \text{otherwise} \end{cases} \tag{2.39}$$

and

$$M_s = \begin{cases} S_o(E-P-R) & \text{if ice-free} \\ (S_o - S_i)F - S_o(P+R) & \text{otherwise} \end{cases} \tag{2.40}$$

where $C_{po} = 4044$ J kg^{-1} K^{-1} is the specific heat of seawater at constant pressure, and M_s and Q_θ are the freshwater flux in salinity-equivalent at the surface and heat flux, respectively. Q^E_{LH} is the latent heat flux due to evaporation:

$$Q^E_{LH} = \rho_o L_v E. \tag{2.41}$$

Q_b is heat flux from ocean to sea ice. Also, S_o and S_i are representative salinities for the ocean and ice, respectively, R is the runoff, and F is the freshwater flux associated with sea ice formation and melting. F is given by

$$F = \frac{\rho_i}{\rho_o}\frac{\partial H_i}{\partial t} \tag{2.42}$$

where ρ_i and H_i are the density and thickness of sea ice, respectively. The boundary conditions at the bottom are given by

$$\frac{\partial \theta}{\partial \mathbf{n}} = \frac{\partial S}{\partial \mathbf{n}} = 0 \tag{2.43}$$

where $\mathbf{n}$ is a unit vector normal to the bottom or the sidewall.

Equation of state

Density of seawater, a nonlinear function of potential temperature, salinity and pressure, is expressed as

$$\rho = \rho(\theta, S, p). \tag{2.44}$$

It is calculated from empirical formula of UNESCO (1981). The time-evolving ocean circulation is governed by seven equations, Eqs. (2.24), (2.27), (2.29), (2.35), (2.36), and (2.44), which contain seven unknown variables, ρ, u, v, w, θ, S, and p. Note that a two-dimensional vector equation, Eq. (2.27), is equivalent to two scalar equations.

2.1.3 The sea ice component

The sea ice component of the coupled model consists of three parts: an ice thickness distribution, thermodynamics, and dynamics, in which sea ice is treated as two-dimensional continuum. A two-level representation of the ice thickness distribution (Hibler 1979), an equilibrium ice-snow system model for thermodynamics (Parkinson and Washington 1979; Semtner 1976), and an elastic-viscous-plastic model for dynamics (Hunke and Dukowicz 1997) are employed.

Ice thickness distribution

To parameterise the existence of ice with a variety of thicknesses in a grid cell, two idealised thickness levels are used: thick and thin. Two quantities, the mean ice thickness (H_i) and the compactness (A), which is defined as the fraction of the grid cell area covered by thick ice, are introduced to describe them. The thickness of thin ice is set to be zero, assuming that open water approximately represents the combined effect of both open water and thin ice up to a demarcation thickness (H_0). The change in the mean ice thickness is given by the vertically-integrated mass balance equation:

$$\frac{\partial H_i}{\partial t} + (\mathbf{v}_h \cdot \nabla_h)\, H_i = S_H \qquad (2.45)$$

where S_H is a source term (net growth of ice) and is calculated from

$$S_H = f_i\,(H_i/A)\, A + f_i\,(0)\,(1 - A) \qquad (2.46)$$

with $f_i\,(H_i)$ being the thermodynamically determined growth rate of ice of thickness H_i.

In a similar fashion, the change in the compactness is given by

$$\frac{\partial A}{\partial t} + (\mathbf{v}_h \cdot \nabla_h)\, A = S_A^+ + S_A^- \qquad (2.47)$$

where S_A^+ and S_A^- are source (formation) and sink (melting) terms, respectively. The source term is calculated from

$$S_A^+ = \begin{cases} (f_i\,(0)\,/H_0)\,(1 - A) & \text{if } f_i\,(0) > 0 \\ 0 & \text{otherwise} \end{cases} . \qquad (2.48)$$

This equation parameterises the phenomenon that, under freezing conditions, the fraction of open water $(1 - A)$ decays exponentially with a time constant of $(H_0/f_i\,(0))$. The sink term is calculated from

$$S_A^- = \begin{cases} (A/2H_i)\,S_H & \text{if } S_H < 0 \\ 0 & \text{otherwise} \end{cases} . \tag{2.49}$$

Here, it is assumed that the thick ice is uniformly distributed between 0 and $2H_i/A$ in thickness, and melting occurs at the same rate. Over a time period of Δt, the ice of thickness less than $S_H \Delta t$ will melt and form open water. By the assumption of uniform distribution, this ice covers a fraction of area equal to $(A/2H_i)\,S_H \Delta t$.

Thermodynamics

An equilibrium ice-snow system model assumes that ice and snow have no heat capacity, and hence their surface temperature is instantaneously in balance with external forcing. The growth rate of ice is calculated differently under three conditions: open water, ice covered ocean without snow on top, and ice covered ocean with snow on top.

In open water, the ice formation rate is calculated from the energy balance at the surface expressed as:

$$Q_t = -Q_{SW} + Q_{LW} + Q_{SH} + Q_{LH}^E \tag{2.50}$$

where Q_t is the heat flux from the atmosphere (positive downward). The heat flux from the ocean (Q_b — positive downward), under freezing condition, is calculated following McPhee (1992):

$$Q_b = c_b u_\tau \rho_o C_{po} \left(T_f - T_o\right) \tag{2.51}$$

where $c_b = 0.0058$ is an empirical constant and $u_\tau = 0.02$ m s^{-1} is the friction speed at the ice-ocean interface. Note that this evaluation is equivalent to relaxing the temperature of the uppermost ocean grid box, with thickness 50 m, to the salinity-dependent freezing point with a time constant of 5 days. The growth rate of ice is calculated from

$$f_i(0) = \begin{cases} \left(Q_b - Q_t\right)/\rho_i L_f & \text{if } Q_b > Q_t \\ 0 & \text{otherwise} \end{cases} \tag{2.52}$$

In an ice-covered region of the ocean without snow on top, the energy balance at the surface is expressed as

$$Q_t = -Q_{SW} + Q_{LW} + Q_{SH} + Q_{LH}^S \tag{2.53}$$

where Q_{LH}^S is the latent heat flux due to sublimation and is

$$Q_{LH}^S = \rho_o L_f S. \tag{2.54}$$

The conductive heat flux through the ice layer (Q_i) is given by:

$$Q_i = \frac{k_i}{H_i}\left(T_o - T_i\right), \tag{2.55}$$

where $k_i = 2.166$ W m^{-1} K^{-1} is the thermal conductivity of ice, H_i is ice thickness, and T_i is ice surface temperature. The surface temperature is calculated by equating the conductive heat flux through the ice with the energy flux at the surface, i.e., $Q_i = Q_t$. If the surface temperature, calculated in this way, exceeds the freezing point ($T_f = 0$°C), it is reduced to the freezing point. After the heat flux from the atmosphere, Q_t, is re-evaluated with the corrected surface temperature, the growth rate of ice is calculated from

$$f_i\left(H_i\right) = \max\left[\left(Q_b - Q_t\right)/\rho_i L_f - S, -H_i/A\Delta t\right]. \tag{2.56}$$

In case sea ice is covered by snow, the surface energy balance and conductive heat flux through the ice layer are also given by Eqs. 2.53 and 2.55, respectively. The conductive heat flux through the snow layer (Q_s) is given by:

$$Q_s = \frac{k_s}{H_s}\left(T_i - T_s\right), \tag{2.57}$$

where $k_s = 0.31$ W m^{-1} K^{-1} is the thermal conductivity of snow, H_s is snow thickness, and T_s is snow surface temperature. The surface temperature is calculated by equating the conductive heat flux through the ice, as well as that through the snow, with the energy flux at the surface, i.e., $Q_i = Q_s = Q_t$. It is assumed that heat from the atmosphere is preferentially used for melting of snow, while heat from the ocean preferentially used for melting of ice. As such,

$$\begin{aligned} f_i\left(H_i\right) &= \max\left[\left(Q_b - Q_t\right)/\rho_i L_f - S, -H_i/A\Delta t\right], & (2.58)\\ f_s\left(H_s\right) &= \begin{cases} \max\left[\left(Q_s - Q_t\right)/\rho_s L_f, -H_s/A\Delta t\right] & \text{if } Q_t > Q_s \\ 0 & \text{otherwise} \end{cases}. & (2.59)\end{aligned}$$

Excessive heat for the melting of snow is utilised for melting of ice, and vice versa. If all of the ice melts, snow is converted to water and placed in the ocean, with necessary latent heat coming from the atmosphere. If the weight of accumulated snow is sufficient to push the ice-snow interface below the ocean surface, then the snow that would otherwise to be submerged is converted to ice.

Dynamics

The vertically-integrated momentum balance equations are

$$mf\,(\mathbf{k}\times\mathbf{v})_h = \nabla_h\cdot\boldsymbol{\sigma} + \boldsymbol{\tau}_a + \boldsymbol{\tau}_w - mg\nabla_h D \tag{2.60}$$

where m is the ice mass per unit area, f is the Coriolis parameter, $\mathbf{k}$ is the unit normal vector in the vertical, $\mathbf{v}_h$ here is the horizontal ice velocity, $\boldsymbol{\sigma}$ is the internal stress tensor, $\boldsymbol{\tau}_a$ and $\boldsymbol{\tau}_w$ are the atmospheric and oceanic stresses, and D is the dynamic height of sea surface. Acceleration and nonlinear advection terms are neglected. The strain rate tensor, $\dot{\epsilon}_{ij}$, is defined as

$$\dot{\epsilon}_{ij} = \frac{1}{2}\left(\frac{\partial v_i}{\partial x_j} + \frac{\partial v_j}{\partial x_i}\right). \tag{2.61}$$

The internal stress tensor is linked to the strain rate tensor through an elastic-viscous-plastic constitutive equation:

$$\frac{1}{E}\frac{\partial\sigma_{ij}}{\partial t} + \frac{1}{2\eta}\sigma_{ij} + \frac{\eta-\zeta}{4\eta\zeta}\sigma_{kk}\delta ij + \frac{P}{4\zeta}\delta_{ij} = \dot{\epsilon}_{ij} \tag{2.62}$$

where E is Young's modulus (dependent on the model resolution), P is the pressure (which is a function of ice thickness and compactness), η and ζ are, respectively, shear and bulk viscosities (which depend on the strain rate and the pressure), and δ_{ij} is the Kronecker delta function. This formulation adds an elastic component to the viscous-plastic rheology forcing through the inclusion of artificial elastic waves that allow for an efficient numerical solution technique using an explicit time step.

The oceanic stress is given by:

$$\boldsymbol{\tau}_w = \rho_o C_{DW}\left|\mathbf{v}_h^w - \mathbf{v}_h\right|\left\{(\mathbf{v}_h^w - \mathbf{v}_h)\cos\theta + [\mathbf{k}\times(\mathbf{v}^w - \mathbf{v})]_h\sin\theta\right\} \tag{2.63}$$

where $C_{DW} = 0.0055$ is the dimensionless water drag coefficient, $\mathbf{v}_h^w$ is the horizontal velocity of geostrophic ocean currents and $\theta = 25°$ is a turning angle. The tilt term $(mg\nabla_h D)$ is calculated using geostrophy and $\mathbf{v}_h^w$, which is approximated as the velocity at the second depth level from the surface.

2.2 The ice sheet model

The continental ice dynamics model (CIDM) used in this study was developed at the University of British Columbia (Marshall 1996; 1997; Marshall and Clarke 1997a). In general, glaciers can move due to superposition of three mechanisms (Marshall 1996; 1998; Paterson 1994): 1) internal deformation of ice (creep); 2) basal sliding; and 3) deformation of subglacial sediment (bed) (Alley 1989). Flow in most regions of an ice sheet is through internal deformation, whereas ice streams and surge lobes flow by the last two mechanisms. The CIDM models the first mechanism based on the vertically-integrated mass balance equation and three dimensional momentum equations under the shallow ice approximation, in which the flow is approximated as simple shear deformation (Marshall 1997). As an ice rheology in the constitutive equations, the traditional Glen's flow law is employed (Glen 1955; 1958).

2.2.1 Dynamics

Mass balance equation

The vertically integrated mass balance equation is expressed as

$$\frac{\partial H_i}{\partial t} + \nabla_h \cdot (\bar{\mathbf{v}}_h H_i) = \dot{b} \tag{2.64}$$

where H_i is ice thickness, $\bar{\mathbf{v}}_h$ is the vertically-averaged horizontal velocity, $\dot{b}$ is the net accumulation rate.

Constitutive equation

The strain rate tensor is defined by Eq. (2.61). Since deformation of ice, to a good approximation, is unaffected by hydrostatic pressure, it is convenient to introduce the deviatoric stress tensor (Paterson 1994, p.78-102). It is obtained by subtracting the amplitude of the hydrostatic pressure (the mean normal stress) from each normal-stress component, leaving the shear-stress components unchanged:

$$\sigma'_{ij} = \sigma_{ij} - \frac{1}{3}\sigma_{kk}\delta_{ij} = \sigma_{ij} + p\delta_{ij}. \tag{2.65}$$

The strain rate is linked to the stress tensor through a nonlinear constitutive equation, known as Glen's flow law (Glen 1955; 1958):

$$\dot{\epsilon}_{ij} = B(T_i)\left(\Sigma_2'\right)^{(n-1)/2}\sigma_{ij}' \tag{2.66}$$

where Σ_2' is the second invariant of the deviatoric stress tensor:

$$\Sigma_2' = \frac{1}{2}\sigma_{ij}'\sigma_{ij}', \tag{2.67}$$

n is the flow law exponent, and $B(T_i)$ represents a strain hardness, which is a function of ice temperature (T_i). In the case of a linear viscous fluid ($n = 1$), this coefficient is equivalent to inverse viscosity. $B(T_i)$ is determined from the Arrhenius relation:

$$B(T_i) = mB_0 \exp\left(-Q/RT_i\right) \tag{2.68}$$

where $R = 8.314$ J mol^{-1} K^{-1} is the ideal gas constant, B_0 is 1.14×10^{-5} Pa^{-3} yr^{-1} ($T_i < 263.15$ K) and 5.47×10^{10} Pa^{-3} yr^{-1} ($T_i \geq 263.15$ K), and Q, the activation energy, is 60 kJ mol^{-1} ($T_i < 263.15$ K) and 139 kJ mol^{-1} ($T_i \geq 263.15$ K). The enhancement factor m accounting for the softening of ice due to impurities, meltwater, and crystal fabric is set to be 3 (van de Wal 1999). As a representative temperature of the lower ice column, where most internal deformation occurs, a uniform (effective) ice temperature of -15°C is specified. Although this value is too cold and makes the ice too stiff in some regions, it is within an acceptable range for the average of warm- and cold-based regions, considering large uncertainties in ice rheology.

Equation of motion

The three-dimensional momentum equations are written as

$$\nabla \cdot \boldsymbol{\sigma} = \rho_i \mathbf{g} \tag{2.69}$$

where ρ_i is the density of ice. Acceleration, nonlinear advection, and the Coriolis terms are small and hence neglected. Under the shallow-ice approximation (where the horizontal length scale is much larger than vertical length scale), the vertically-integrated momentum equations and Glen's flow give the vertically-integrated horizontal ice volume flux:

$$\bar{\mathbf{v}}_h H_i = -\frac{2B(T_i)}{n+2}\left(\rho_i g\right)^n H_i^{n+2}|\nabla_h h_s|^{n-1}\nabla_h h_s \tag{2.70}$$

where h_s is the surface elevation. The exponent n of Glen's flow law is set to be 3, which is typical for ice sheet studies (Paterson 1994, p.86). Therefore, the volume flux varies with ice thickness to the power 5 and surface slope to the power 3. As $H_i = h_s - h_b$ with h_b being the bedrock elevation, substitution of Eq. (2.70) into Eq. (2.64) produces a single equation containing one unknown variable, h_s.

2.2.2 Glacio-isostacy

In general, the bedrock responds to the varying ice load through an elastic deformation of the lithosphere and a viscous flow in the asthenosphere. In this study, the resulting uplift and depression of the bedrock is approximated by local displacement of mantle material, neglecting the lithosphere flexure. A local response type isostatic adjustment is applied, in which the response is relaxed to a local isostatic equilibrium:

$$\frac{\partial h_b}{\partial t} = -\frac{1}{\tau}\left(h_b + r_\rho H_i - h_b^0\right) \tag{2.71}$$

where r_ρ is the ratio of ice density to bedrock density, h_b^0 is the undisturbed (ice-free) equilibrium bedrock elevation, and τ is the relaxation time set to be 3000 years in this study (Peltier and Marshall 1995; Tarasov and Peltier 1997a).

2.3 Atmospheric general circulation model

The second generation AGCM of the CCCma (see Glossary of Acronyms), which is referred to as GCMII, is used in this study. This model and its present-day climate are described in detail in McFarlane et al. (1992).

The AGCM employs a spectral formulation for the representation of the horizontal variation of prognostic variables, and a piecewise-constant finite-element formulation on a hybrid coordinate system for vertical discretization (Laprise and Girard 1990). Horizontal resolution is defined in terms of the wavenumber truncation of 32, in which triangular truncation is applied (T32). The associated Gaussian grid has a mesh size of approximately 3.75° and 3.75° in latitude and longitude, respectively. There are 10 unevenly spaced hybrid coordinate levels (L10) between the surface and 12 hPa, following the terrain at the low levels and the pressure at the higher levels.

As described in McFarlane et al. (1992), radiative fluxes and heating rates in the model are evaluated using the radiative transfer schemes of Morcrette (1990; 1991) for terrestrial radiation. The solar radiation is calculated following Fouquart and Bonnel (1980), in which the upward and downward irradiance profiles are evaluated. Clouds and cloud water are determined diagnostically as functions of relative humidity and temperature. Concentration of carbon dioxide is specified by a constant mixing ratio throughout the atmosphere while that of ozone is prescribed as a function of latitude, height, and month.

The horizontal fluxes of momentum, heat, and moisture due to unresolved transfer processes are parameterised by scale-dependent eddy diffusive formulations. The vertical fluxes due to turbulent transfer in the free atmosphere are parameterised by stability-dependent eddy diffusive formulations, while at the surface they are parameterised by stability-dependent aerodynamic bulk formulae. The depth of the planetary boundary layer is not explicitly calculated. The vertical flux of momentum through unresolved, orographically-excited, vertically-propagating gravity waves is also parameterised as an additional drag force on the resolved flow, since the effect of these waves is sufficiently large to modify the large-scale mean flow (McFarlane 1987). The effects of moist convection are parameterised through an adjustment procedure which is applied on pairs of vertical layers whenever the local lapse rate exceeds a critical value.

Condensation occurs and latent heat is released under the condition of local supersaturation, and all condensed liquid water falls to the surface as precipitation. If the SAT is below the freezing point, the precipitation is assumed to fall as snow, otherwise it is assumed to fall as rain.

The land surface is represented by a single soil layer covered by bare soil, primary vegetation, and secondary vegetation. The properties of the layer vary with location. There are 21 soil categories and 24 vegetation types, which are taken from Wilson and Henderson-Sellers (1985). The areal fraction of bare soil is specified in each grid, two-thirds of the rest of the area is occupied by primary vegetation and one-third by secondary vegetation. Surface temperature is calculated to ensure the energy balance at the surface by equating the net heat flux from the atmosphere with the conduction of heat through the soil (and snow) layer. The energy balance at the surface is expressed as

$$H_G = (1-\alpha)\,S - Q_{LW} - Q_{SH} - L_v E - L_f\,(M_F + M_L + M_S) \tag{2.72}$$

where H_G represents the variations of heat storage, α is the surface albedo, S is the flux of solar radiation reaching the surface, Q_{LW} is the net upward flux of terrestrial radiation at the surface, and Q_{SH} and $L_v E$ are the sensible and latent heat fluxes at the surface, respectively. M_F and M_S are the melting rate of frozen soil moisture and snow, respectively, and M_L is the freezing rate of liquid soil moisture, with L_f being the latent heat of fusion. The heat storage in the soil layer is calculated from the force-restore method of Deardorff

(1978):

$$H_G = \frac{C_*}{2}\left[\frac{\partial T_g}{\partial t} + \omega\left(T_g - T_0\right)\right] \tag{2.73}$$

where ω is the diurnal frequency, T_g is the ground temperature, and T_0 is the mean temperature of T_g in the previous 24 hours period. The effective heat capacity C_* of the soil layer is a function of soil heat capacity (C_g) and the thermal conductivity of the soil (λ_g), which are also functions of soil type, soil moisture content, and snow cover. Soil moisture is predicted by a "bucket" model which has a field capacity and evapotranspiration slope factor varying with soil categories and vegetation types. Soil moisture includes both liquid and frozen water. When the local water content of the soil layer exceeds the local field capacity, the excess water is assumed to be runoff. The evapotranspiration rate is parameterised as

$$E = \left\{\min\left[W/\left(sW_c\right), 1\right] \times \left(1 - \delta_s\right) + \delta_s\right\} E_p \tag{2.74}$$

where s is the evapotranspiration slope factor, W is the soil moisture amount, W_c is the soil moisture field capacity, δ_s is the fractional snow cover, and E_p is the potential evapotranspiration rate.

The surface albedo is determined for the two spectral intervals used in the solar radiation scheme. Over dry land a local value is specified as a weighted average for each of the 24 vegetation types; for wet soil, albedos are reduced up to 7%. The local land albedo also depends on the fractional snow cover and its age. Over the ocean, latitude-dependent albedos which range between 0.06 and 0.017 are specified independent of the spectral interval. The background albedos for sea ice are 0.55 in the near-infrared and 0.75 in the visible; these values are modified by snow cover. The longwave emissivity is prescribed as unity for all surfaces.

Chapter 3

Glacial termination: Changes in thermohaline circulation

3.1 Introduction

Although there is an interaction between the wind-driven and thermohaline components of ocean circulation, ocean circulation is generally conceptualised by considering them separately. The wind-driven circulation encompasses flow in the surface layer that is driven by the wind stress, and leads to stretching and squeezing of the water column, which in turn drives flow in the interior ocean so that it approximately conserves potential vorticity. Frictional forces come into play near the boundaries. On the other hand, the thermohaline circulation is driven by the horizontal pressure gradients produced by temperature and salinity fields through changes in sea water density. In the present-day Atlantic, the meridional temperature gradient drives a northward flow near the surface, while the meridional salinity gradient works as a brake.

The significance of the thermohaline circulation in climate lies in its role in heat transport. Direct estimates of ocean heat transport indicate that the present-day ocean carries 2.0 PW (1 PW $\equiv 10^{15}$ W) of heat poleward across 24°N, compared to a total energy transported by the planet estimated at 5.2 PW across the same latitude (Bryden 1993). Note that residual estimates (the difference in heat transport between the planet and the atmosphere) support the values obtained by the direct estimate (Trenberth and Solomon 1994). At 24°N in the Pacific, where no deep water is formed in high latitudes, 0.38 PW of heat is transported poleward via a vertical circulation cell while 0.38 PW is transported via a horizontal circulation cell (Bryden 1993). On the other hand, at 24°N in the Atlantic, where deep water is formed in high latitudes, 1.28 PW of heat is transported poleward via a vertical circulation cell while -0.06 PW is transported via a horizontal circulation cell (Bryden 1993). The profound impact on climate, resulting from the collapse of thermohaline circulation, has been demonstrated in model simulations (e.g., Manabe and Stouffer 1988; Rind et al. 1986).

The present-day meridional circulation in the Atlantic is considered to be a part of global ocean circulation with time scale for recirculation of thousands of years, popularly called the ocean's 'conveyor belt' (Gordon 1986; Broecker 1991). The 'conveyor belt' is characterised by highly-localised deep convection and broad upwelling, in which the latter counteracts the downward diffusion of heat and maintains the thermocline. Today's major convection regions are located in the Greenland-Iceland-Norwegian (GIN/Nordic) Seas, in the Labrador Sea, in the Weddell Sea and in the Ross Sea (Killworth 1983; Marshall and Schott 1999; Weaver et al. 1999). As a consequence of the water mass modification by convective mixing and downward diffusion of heat, density and pressure gradients develop in the Atlantic such that deep water formed in the northern high latitudes flows southward and relatively warm thermocline water flows northward. As noted by Weaver and Hughes (1992), and Marotzke and Scott (1999), convective mixing and downwelling are two fundamentally different processes, and convection does not necessarily accompany the downwelling (Send and Marshall 1994). At 24°N in the Atlantic, it is estimated that 17±4 Sv thermocline water flows northward, 20±5 Sv North Atlantic Deep Water (NADW) flows southward below it (as a deep western boundary undercurrent), and 3±3 Antarctic Bottom Water (AABW) flows northward further below the NADW (Roemmich and Wunsch 1985).

Geochemical reconstructions suggest that Atlantic meridional overturning may have been shallower during the LGM (Boyle 1995): 1) δ^{13}C in benthic foraminifera indicates that the glacial NADW did not penetrate as far south (e.g., Duplessy et al. 1988); 2) Cd/Ca ratio in benthic foraminifera indicates that the NADW was diminished relative to the AABW in the North Atlantic (Boyle and Keigwin 1982), and it also suggests that more intensive production of intermediate water instead of deep water occurred in the North Atlantic (Boyle and Keigwin 1987); 3) δ^{18}O in benthic foraminifera indicates that the Gulf Stream weakened in the Florida Straits (Lynch-Stieglitz et al. 1999); 4) The ^{231}Pa/^{230}Th ratio in the sediments indicates that the glacial North Atlantic Intermediate Water (NAIW) was exported at a similar rate to the present-day NADW (Yu et al. 1996); and 5) the vertical ^{14}C contrast between planktonic and benthic foraminifera indicates that ventilation of the deep North Atlantic remained the same as today (Broecker 1989).

While a large number of model studies have been conducted on changes in atmospheric circulation at the LGM, much fewer have been conducted on changes in ocean circulation. In the early studies, AGCM output was used to infer the paleoceanographic conditions (Keffer et al. 1988; Miller and Russell 1989). Keffer et al. (1988), analysing the wind field obtained from an AGCM simulation, suggested that the position of the boundary between subtropical and subpolar gyres in the North Atlantic, and hence the position of the Gulf Stream-

North Atlantic Current system were more zonal during the LGM than today. Miller and Russell (1989), on the other hand, from the analysis of surface heat fluxes obtained from an AGCM simulation, suggested that northward heat transport in the Atlantic was significantly reduced at the LGM. In later studies, AGCM output was used to drive ocean-only models (Lautenschlager et al. 1992; Fichefet et al. 1994; Bigg et al. 1998). Lautenschlager et al. (1992) found that deep water production completely stopped in the North Atlantic, and that thermohaline overturning started intensively (more than 52 Sv) in the North Pacific, using the MPI (see Glossary of Acronyms) geostrophic global ocean model driven by CLIMAP (see Glossary of Acronyms) SST (CLIMAP 1981), and wind stress and freshwater flux derived from an AGCM simulation. Bigg et al. (1998), using a global OGCM, showed that two stable states existed under glacial boundary conditions derived from an AGCM simulation: the state in which deep water formation occurs in the North Atlantic (55.7 Sv) and the state in which it occurs in the Southern Ocean (12.1 Sv). Both results of Lautenschlager et al. (1992) and Bigg et al. (1998) are, however, unrealistic compared to geochemical reconstructions. Fichefet et al. (1994) showed that the Atlantic meridional overturning reduced to 11 Sv from the present-day 17 Sv, using a three-basin, zonally-averaged ocean model driven by wind stress anomalies derived from an AGCM simulation, and SST and salinity anomalies taken from the differences between reconstructions and present-day observations. The weakening of the overturning was accompanied by the shallowing of the overturning, and southward shift of the deep water formation region.

In the above model studies, uncertainty and limitation arises from the use of the CLIMAP SST reconstruction (CLIMAP 1981) in driving the AGCM as the validity of the reconstruction has been questioned (Rind and Peteet 1985; de Vernal and Hillaire-Marcel 2000; de Vernal et al. 2000). In the recent studies, coupled climate models of intermediate complexity have been used (Ganopolski et al. 1998; Weaver et al. 1998). Ganopolski et al. (1998) found a shallower meridional overturning and southward shift of deep water formation region in the Atlantic. The strength of the overturning was, however, only slightly reduced. Weaver et al. (1998), on the other hand, displayed a weaker and shallower meridional overturning, but the southward shift of the deep water formation regions was not observed. Although the shallowing of the overturning without weakening, in Ganopolski et al. (1998), is consistent with Cd/Ca and ^{231}Pa/^{230}Th records, the validity of these proxies has recently been questioned in conjunction with a possible biological activity (Rutberg et al. 2000). Moreover, it has been pointed out that the southward shift of the deep water formation region in Ganopolski et al. (1998) and Fichefet et al. (1994) may result from the coupling of convection and downwelling, inherent in the two-dimensional models

(Schmittner et al. 2001).

Several LGM simulations have been conducted using fully coupled atmosphere-ocean GCMs (Bush and Philander 1998; Hewitt et al. 2001; Kitoh et al. 2001). In Bush and Philander (1998), only 15 years of integration, including the model spin-up, was done. Their results therefore cannot address issues related to the changes in thermohaline circulation. Although a longer integration (700 years) was conducted by Hewitt et al. (2001) without flux adjustments, they pointed out that the reults may still be in a transient stage. Kitoh et al. (2001) integrated for 70 years with an oceanic acceleration technique (1680 years for deep oceans) and for a further 140 years without the acceleration technique. The use of flux adjustments in their study (for heat and freshwater) is, however, the largest concern. In addition, both Hewitt et al. (2001) and Kitoh et al. (2001) found a stronger Atlantic meridional overturning, which is inconsistent with paleoceanographic reconstructions.

Since the time period of focus in these studies is the LGM and not the glacial termination, few studies regarding changes in thermohaline circulation have been conducted under different orbital forcing (see Brickman et al. 1999). In addition, the mechanisms responsible for the changes in Atlantic meridional overturning have not been sufficiently investigated (Crowley and Häkkinen 1998). In this chapter, the potential mechanisms which might have affected the thermohaline circulation during the last deglaciation are explored. The model used in this study is similar to the one used by Weaver et al. (1998) for their LGM simulation except that the dynamic sea ice model is now incorporated in the present model.

3.2 Experimental design

To investigate the response of thermohaline circulation to changes in the atmospheric CO_2 concentration and orbital geometry during the last deglaciation, the coupled climate model was integrated under four different sets of external forcing in addition to the present-day control simulation (Table 3.1). The time period of interest in these experiments is centred around 11 kaBP, when the NH summer insolation was at a maximum during the last deglaciation, and 21 kaBP (LGM), when it was close to a minimum (Fig. 3.1). The orbital parameters specified in the experiments are summarised in Table 3.2. Two different atmospheric CO_2 concentration, 200 ppmv (LGM level) and 280 ppmv (pre-industrial level), were used for the purpose of conducting a sensitivity analysis. It is important to note that the experimental results under perpetual 11 kaBP orbital forcing do not represent the actual environment at 11 kaBP since the actual 11 kaBP climate is in a transient stage and far from steady state in terms of ocean circulation. In particular, it is in the midst of the Younger Dryas, which is not being simulated here as no freshwater perturbations from retreating ice sheets has been externally imposed.

Table 3.1: **Experimental design for CO_2 perturbation**

Experiments	Orbital geometry	CO_2 concentration (ppmv)	Relative CO_2 radiative forcing (W m^{-2})
A1	present-day	350	0.0
A2	11 kaBP	280	-1.3
A3	11 kaBP	200	-3.2
A4	21 kaBP	280	-1.3
A5	21 kaBP	200	-3.2

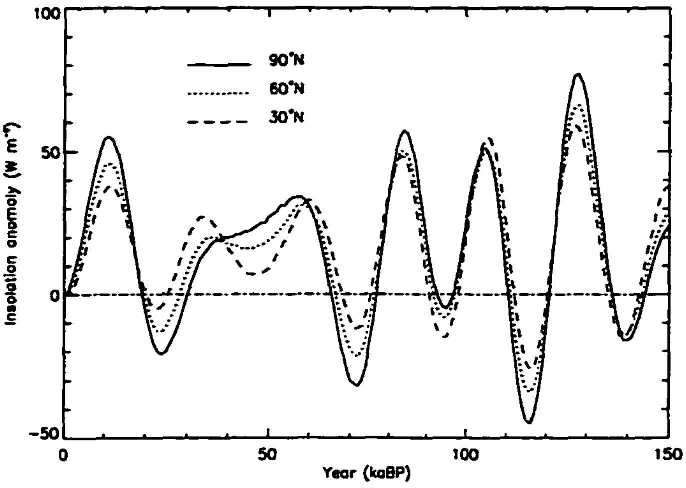

Figure 3.1: **Summer (mid-June) insolation anomaly relative to the present at 90°, 60°, and 30°N after Rind et al. (1989), and based on data from Berger (1978).**

The coupled climate model was integrated for 2000 years until a quasi-steady state was reached, and the same initial-conditions were used in all integrations. For the oceanic component, these initial conditions consisted of a resting ocean, with an idealised temperature profile, varying with latitude and depth that roughly approximates the present-day annual-mean observations, and a uniform salinity (34.9 psu). Similarly, for the atmospheric component, a horizontally-uniform SAT (10°C) and a dry atmosphere (zero specific humidity) are assumed. No initial sea ice/snow and land ice/snow were specified, but present-day ice sheets are implicitly incorporated by using a present-day surface elevation. No wind

Table 3.2: **Orbital parameters used in the experiments**

Ages	Perihelion (°)	Obliquity (°)	Eccentricity
present-day	283.0	23.44	0.01668
11 kaBP	89.13	24.21	0.01950
21 kaBP	295.0	22.95	0.01898

Perihelion: longitude of perihelion relative to the moving vernal equinox

stress feedback was employed in any experiments because of its negligible effect in this application of the model (Weaver et al. 1998).

The above sensitivity experiments revealed (see later) that the strength of the Atlantic meridional overturning is affected by orbital forcing when the CO_2 level is low enough ($\sim$ 200 ppmv). However, it was not clear which orbital parameter is responsible for, or more influential on, the changes in the meridional overturning strength. To address these questions, additional experiments were conducted. The model was integrated under four different orbital configurations (Table 3.3). The configurations are rather extreme within a reasonable range during the last glacial cycle, and are similar to values used by Gallimore and Kutzbach (1995) and Phillipps and Held (1994) in their AGCM experiments. Eccentricity was fixed at the approximate largest value (0.04) during the last glacial cycle so that the effect of precession is emphasised. Note that this value is about half of the typical value during the last deglaciation (Table 3.2). The CO_2 level is also fixed at the approximate lowest value (200 ppmv) during the last glacial cycle.

Table 3.3: **Experimental design for orbital perturbation**

Experiments	Obliquity (°)	Perihelion (°)	CO_2 concentration (ppmv)
A6	22	270	200
A7	22	90	200
A8	25	270	200
A9	25	90	200

3.3 Results

3.3.1 Meridional overturning streamfunction

The thermohaline circulation in the Atlantic is characterised by the meridional-vertical circulation, which is conveniently described by the zonally-averaged meridional overturning streamfunction ψ. The streamfunction is constructed by integrating zonally between either two fixed meridional boundaries, on which the zonal velocity is assumed to vanish, or over a zonally periodic domain (Pacanowski and Griffies 1999, p.521-529). Define the zonally-averaged meridional velocity and vertical velocity as

$$\mathcal{V}(\phi, z, t) = \int_{\lambda_w}^{\lambda_e} v\, dx, \tag{3.1}$$

$$\mathcal{W}(\phi, z, t) = \int_{\lambda_w}^{\lambda_e} w\, dx, \tag{3.2}$$

where λ_w and λ_e are longitudes of the meridional boundaries at the western and eastern sides, respectively, and $dx = a\cos\phi\, d\lambda$. The zonal-integration of the continuity equation yields

$$\int_{\lambda_w}^{\lambda_e} \nabla\cdot\mathbf{v}\, dx = 0,$$

$$\Rightarrow \quad \frac{\partial\mathcal{V}}{\partial y} + \frac{\partial\mathcal{W}}{\partial z} = 0. \tag{3.3}$$

Therefore, it is possible to define a streamfunction such that

$$\frac{\partial\psi}{\partial y} = \mathcal{W}, \quad \frac{\partial\psi}{\partial z} = -\mathcal{V}. \tag{3.4}$$

It is easily shown that the streamfucntion, defined in this way, satisfies the Eq. (3.3), and also that lines of constant ψ are parallel to the zonally-averaged velocity vector. The streamfunction is then calculated from

$$\psi(\phi, z, t) = -\int_{-H(\lambda,\phi)}^{z} \mathcal{V}\, dz', \tag{3.5}$$

so that the streamfunction at the bottom is zero. Note that the streamfucntion becomes zero at the surface as well under the rigid lid approximation, since the total volume of meridional flow at any given latitude must be conserved:

$$\int_{-H(\lambda,\phi)}^{0} V\, dz' = 0. \tag{3.6}$$

The simulated present-day meridional overturning streamfunction in the Atlantic (A1) is shown in Fig. 3.2. It is seen that AABW intrudes into the NH near the bottom between about 3000 m and 4000 m in depth, NADW penetrates into the SH between about 2000 m and 3000 m in depth, and there is a northward flow in the upper layer above about 1000 m in depth. The structure and flow rates are comparable to observations, although the formation of deep water occurring near 60°N is too far south.

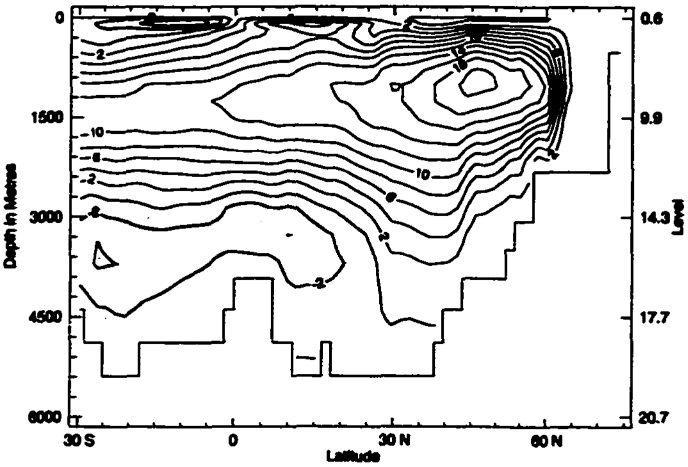

Figure 3.2: **Simulated annual mean, present-day, zonally-averaged meridional overturning streamfunction in the Atlantic Ocean (A1). Contour interval is 2 Sv (1 Sv ≡ 10^6 m^3 s^{-1}), and counterclockwise circulation is shaded.**

3.3.2 Depth-integrated steric height

In studies using box models, it has been assumed that the rate of the meridional flow is proportional to the meridional density contrast in the upper layer ocean (e.g., Stommel 1961; Rahmstorf 1996), with which the existence of the cross-equatorial flow in the Atlantic can be understood. The theoretical basis of this assumption comes from the fact that the large scale ocean circulation is approximated by geostrophic flow, in which the pressure gradient force and Coriolis force are in balance. The meridional density gradient, mainly arising from the equator-to-pole temperature gradient, develops an east-west pressure gradient in the presence of meridional boundaries, which in turn leads to a northward geostrophic flow (Weaver and Hughes 1992; Colin de Verdiére 1993). Hughes and Weaver (1994) demonstrated that the strength of the meridional overturning is proportional to the meridional contrast in depth-integrated steric height, using a two-basin OGCM, and hence the assumption is reasonable. Further support of the idea, which links the meridional overturning strength to the meridional density contrast, was given by Fichefet et al. (1994) using a three-basin, zonally-averaged ocean model, and Wiebe and Weaver (1999) using a global OGCM with realistic geography and bathymetry. Note that, however, Fichefet et al. (1994) examined the surface density contrast, rather than depth-integrated steric height, and also parameterised the zonal density gradient in their model as being proportional to the meridional gradient of zonally-averaged density.

The depth-integrated steric height, $\mathcal{P}$, is a measure of the depth-integrated pressure above a reference level z_0, and is defined as

$$\mathcal{P} = \int_{p(z_0)}^{0} \int_{p(z_0)}^{p} g^{-2} \delta' \left(T, S, p'\right) \, dp' \, dp \tag{3.7}$$

where g is the gravitational acceleration, p is the hydrostatic pressure, and δ' the specific volume anomaly (Godfrey 1989). The specific volume anomaly is given by

$$\delta' \left(T, S, p\right) = \delta \left(T, S, p\right) - \delta \left(0, 35, p\right) \tag{3.8}$$

with δ representing specific volume (reciprocal density), i.e., $\delta = 1/\rho$. Applying the hydrostatic approximation:

$$g^{-1} \, dp = -\rho \, dz, \tag{3.9}$$

equation (3.7) can be expressed as

$$\begin{aligned} \mathcal{P} &= \int_{z_0}^{0} \int_{z_0}^{z} \delta' \left(T, S, z'\right) \left\{\rho \left(T, S, z'\right)\right\}^2 dz' \, dz \\ &= -\int_{z_0}^{0} \int_{z_0}^{z} \frac{\rho \left(T, S, z'\right) - \rho \left(0, 35, z'\right)}{\rho \left(0, 35, z'\right)} \rho \left(T, S, z'\right) \, dz' \, dz, \end{aligned} \tag{3.10}$$

qualitatively representing a cumulative density anomaly in the vertical direction.

The simulated present-day depth-integrated steric height in the Atlantic (A1), with a reference level at 1257 m, is shown in Fig. 3.3. Only latitudes between 40°S and 80°N, covering the area bounded by meridional land boundary, that is, between southern tip of Africa (Cape of Good Hope) and NADW formation region, are presented. Ideally, the reference level should be taken from at a level of no motion. It is, however, difficult to find a definitive level at all latitudes. Hughes and Weaver (1994) used the mid-depth of each overturning cell as a reference level in their analysis, while Wiebe and Weaver (1999) and Weaver et al. (2001) used fixed reference levels of 925 m and 1257 m, respectively. In this study, a fixed reference level of 1257 m (level 9 of the model), which is approximately the mid-depth of the overturning cells, is adopted to facilitate the analysis discussed later unless otherwise noted. The zonally-averaged depth-integrated steric height field (Fig. 3.3) is relatively flat in the tropics, and a steep gradient exists in the mid-latitude of North Atlantic. This steep gradient reflects the equator to pole temperature gradient as the salinity field tends to drive flow in the opposite direction. This is why the present-day thermohaline circulation is sometimes described as a thermally-direct circulation. As discussed in the next paragraph, the relation between the meridional gradient in the depth-integrated steric height and the meridional flow is only applicable for the basin-scale gradient in the depth-integrated steric height. For example, the cross-equatorial flow is only consistent with the difference in the depth-integrated steric height between the SH and NH, rather than the local gradient in the tropics.

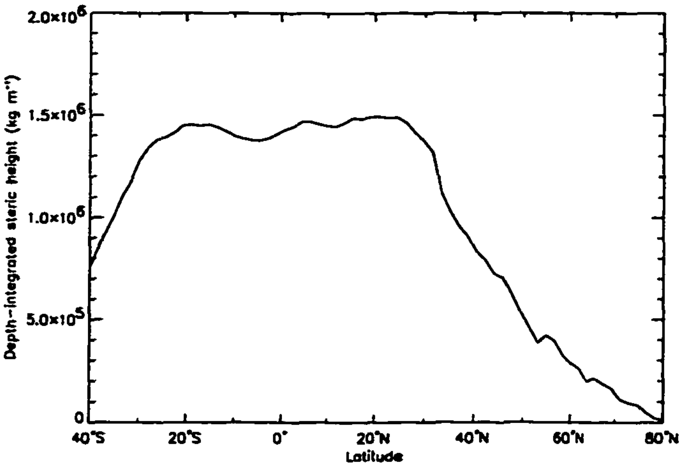

Figure 3.3: **Simulated present-day, annual mean, zonally-averaged depth-integrated steric height in the Atlantic Ocean (A1).**

Figure 3.4 shows the relationship between the meridional contrast of depth-integrated steric height and the strength of the meridional overturning at equilibrium of all experiments in this study (A1–A9). The meridional difference is taken between 30°S and 60°N. Hughes and Weaver (1994) used the difference between 47.25°S, where the South Atlantic connected to the South Pacific in their model, and the latitude of maximum surface density, while

Wiebe and Weaver (1999) used the difference between the equator and the latitude of maximum surface density. Small latitudinal fluctuations in surface density tend to produce large shifts in the choice of the latitude of maximum surface density, despite there being no changes in the latitude of deep water formation. Therefore, the latitude of maximum surface density is not adopted in the study. Note that Weaver et al. (2001) chose 40°S and 60°N.

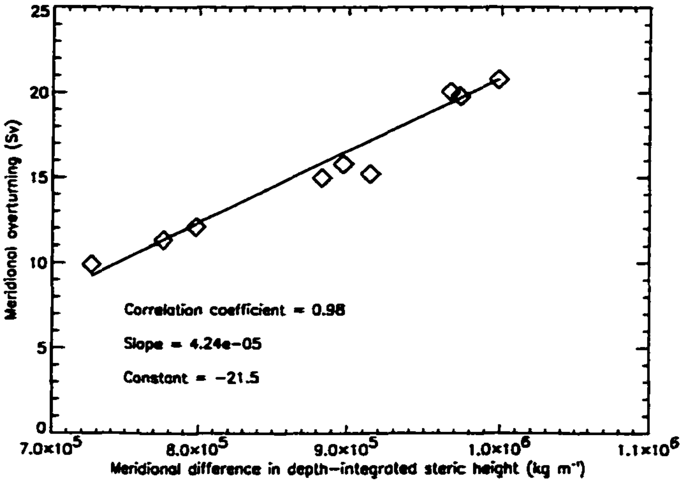

Figure 3.4: **Relationship between the meridional contrast in depth-integrated steric height between 30°S and 60°N, and the strength of the meridional overturning in the Atlantic Ocean.**

3.3.3 Effect of atmospheric CO_2 concentration

The annual mean response of global SST and the Atlantic meridional overturning to changes in atmospheric CO_2 concentration is summarised in Table 3.4. The meridional overturning streamfunction in each experiment is displayed in Fig. 3.5a–3.5d. It is seen that the strength of the meridional overturning can be strongly affected by variations in atmospheric CO_2 concentration. However, the magnitude of the response is not straightforward: there is little difference in the overturning strength between 350 ppmv CO_2 forcing (A1) and 280 ppmv CO_2 forcing (A2 and A4), while there is relatively large difference between 280 ppmv CO_2 forcing (A2 and A4) and 200 ppmv CO_2 forcing (A3 and A5). These results cannot be explained by a linear response of the thermohaline circulation to CO_2 radiative forcing. In addition, the thermohaline circulation responds differently to CO_2 forcing under different orbital geometry: the reduction of the overturning due to decreased CO_2 (280 ppmv to 200 ppmv) under the 11 kaBP orbit (from A2 to A3) is about 25%, while under the 21 kaBP orbit (from A4 to A5) it is about 40%. As such, the strength of the meridional overturning can also be affected by variations in orbital geometry. The details of the effect of orbital forcing on thermohaline circulation is explored in the next subsection.

Table 3.4: **Annual mean response to CO_2 forcing**

Experiments	Global SST (°C)	Atlantic meridional overturning ψ (Sv)
A1	18.3	20.8
A2	17.4	20.1
A3	16.3	15.0
A4	17.6	19.8
A5	16.4	12.1

To identify the mechanism responsible for the maintenance of the meridional overturning, the depth-integrated steric height is examined at equilibrium. Fig. 3.6a shows the difference in equilibrium depth-integrated steric height between A2 and A3, and represents the effect of CO_2 forcing under the 11 kaBP orbit. Similarly, Fig. 3.6b shows the difference between A4 and A5, representing the effect of CO_2 forcing under the 21 kaBP orbit. The contribution of the temperature difference between the two experiments to the difference in depth-integrated steric height is evaluated by using the temperature field of each experiment with the same salinity field in calculating density fields. Similarly, the contribution of the salinity difference is evaluated by using salinity field of each experiment with the same temperature field in calculating density fields. The sum of the two contributions is confirmed to be virtually identical to the contribution of both temperature and salinity differences.

The depth-integrated steric height contributed by the temperature difference, in both Fig. 3.6a and Fig. 3.6b, have the following features: an increase between 40°S and 10°N; a large increase between 20°N and 50°N; a small increase or decrease between 60°N and 80°N. On the other hand, the depth-integrated steric height contributed by the salinity difference shows a slight increase between 40°S and 30°N; a large decrease between 40°N and 70°N; another slight increase between 70°N and 80°N. The large increase in temperature between 20°N and 50°N corresponds to the latitude of large increase in northward velocity and hence poleward heat transport. The large increase in salinity at about 60°N is maintained by the decrease in net downward freshwater flux at the corresponding latitudes, which is in balance with an increase in the Arctic (Figs. 3.7a and 3.7b). However, increased net

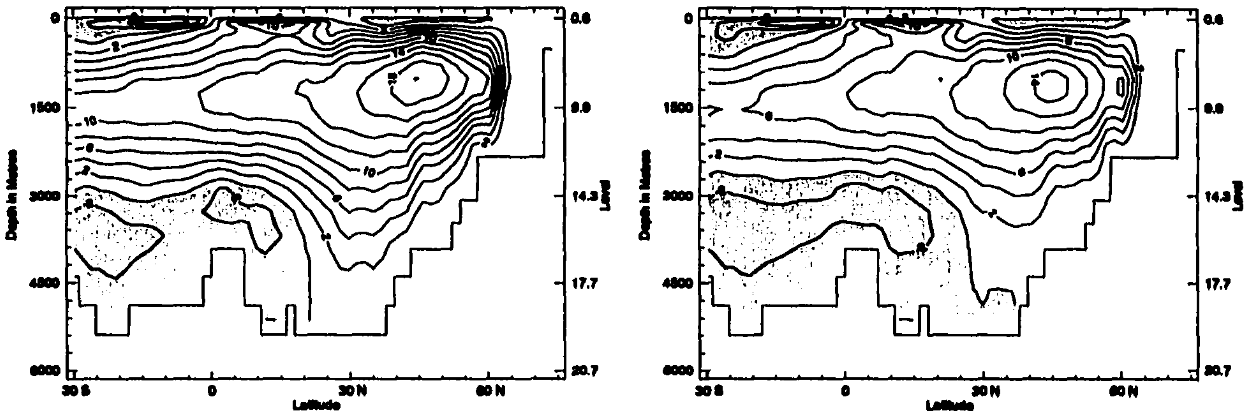

a 11 kaBP orbit and 280 ppmv CO₂ (A2)

b 11 kaBP orbit and 200 ppmv CO₂ (A3)

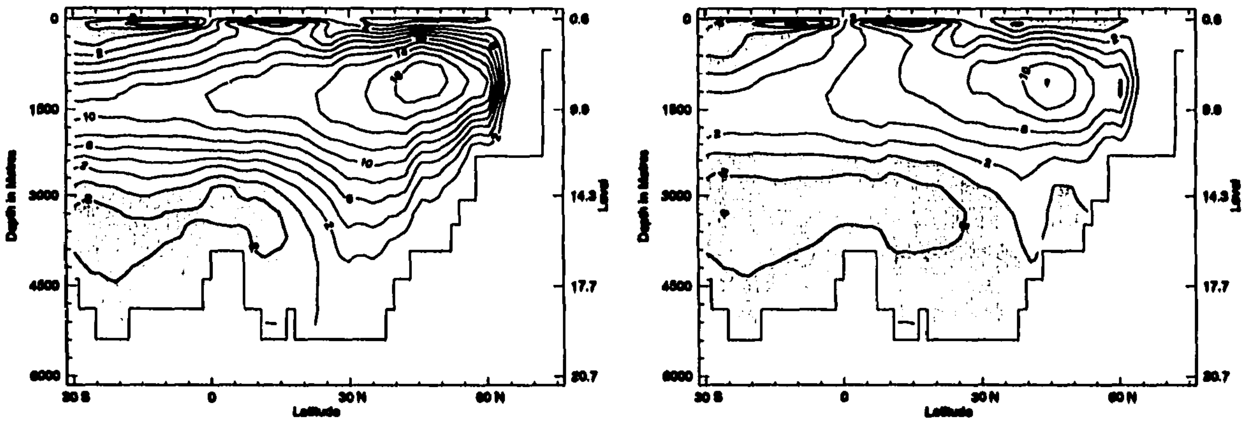

c 21 kaBP orbit and 280 ppmv CO₂ (A4)

d 21 kaBP orbit and 200 ppmv CO₂ (A5)

Figure 3.5: **Simulated annual mean, zonally-averaged meridional overturning streamfunction in the Atlantic Ocean. Contour interval is 2 Sv (1 Sv $\equiv 10^6$ m^3 s^{-1}), and counterclockwise circulation is shaded.**

moisture transport from the northern North Atlantic to the Arctic cannot be explained by the difference in the hydrological cycle between the experiments (Figs. 3.7c and 3.7d). A concurrent decrease of salinity and sea-ice thickness in the Arctic, and smaller winter sea-ice extent in the North Atlantic (Figs. 3.8a–3.8d), therefore, suggest that this salinification occurs through processes involving sea ice. The reduced formation of sea ice in the Arctic, advection from the Arctic to the northern North Atlantic, and the melting in the northern North Atlantic results in a net freshwater transport from the northern North Atlantic to the Arctic through the sea surface. Although a complication arises from feedback mechanisms, which reside in the nature of thermohaline circulation, in determining the cause and effect, the most important implication in the analysis of depth-integrated steric height at equilibrium is the fact that the difference in the meridional gradient of depth-integrated steric height on inter-hemispheric scale is maintained by the difference in the salinity field (Figs. 3.6a and 3.6b).

To separate the primary cause from the secondary amplification (positive feedback), the depth-integrated steric height at an early stage of integration is also examined. Fig. 3.6c shows the difference between A2 and A3 in depth-integrated steric height at 200 years of integration, when the difference in the strength of meridional overturning is only about 2.3 Sv. Similarly, Fig. 3.6d shows the difference between A4 and A5 at 200 years of integration, when the difference in the strength of meridional overturning is only about 1.5 Sv. A reference level of 793 m (level 7 of the model) is adopted in both cases, adjusting to the shallower overturning cell during the early stage. Contrary to the cases of equilibrium (Figs. 3.6a and 3.6b), the difference in meridional gradient of depth-integrated steric height during early stage of integration arises from the temperature difference and not the salinity difference (Figs. 3.6c and 3.6d). The general increase in depth-integrated steric height in low latitudes reflects the global warming due to the raised CO_2 level. There is little warming between 60°N and 80°N where variations in sea water temperature are restricted to be near the freezing point in the presence of a sea ice cover.

3.3.4 Effect of orbital parameters

The effect of the orbital parameter on insolation is shown in Figs. 3.9a–3.9d. Both Figs. 3.9a and 3.9c show the difference between A7 and A6, representing the effect of changes in precession, while both Fig. 3.9b and 3.9d show the difference between A8 and A6, representing the effect of changes in obliquity. Figs. 3.9a and 3.9b are displayed in terms of celestial longitude with respect to the moving vernal equinoxes, which emphasises the seasonal difference in insolation. On the other hand, Figs. 3.9c and 3.9d are displayed in

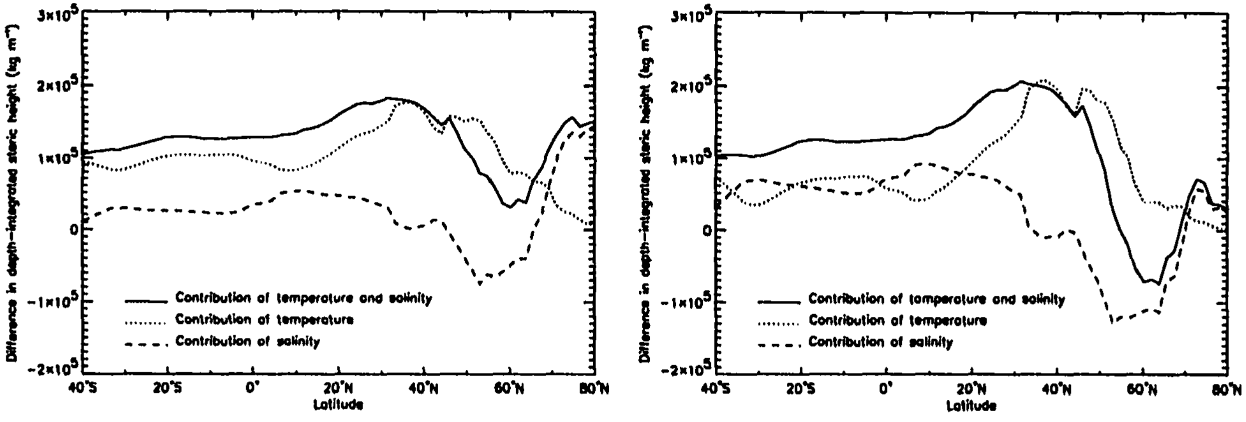

a 11 kaBP equilibrium (A3 minus A2; 2000 years) b 21 kaBP equilibrium (A5 minus A4; 2000 years)

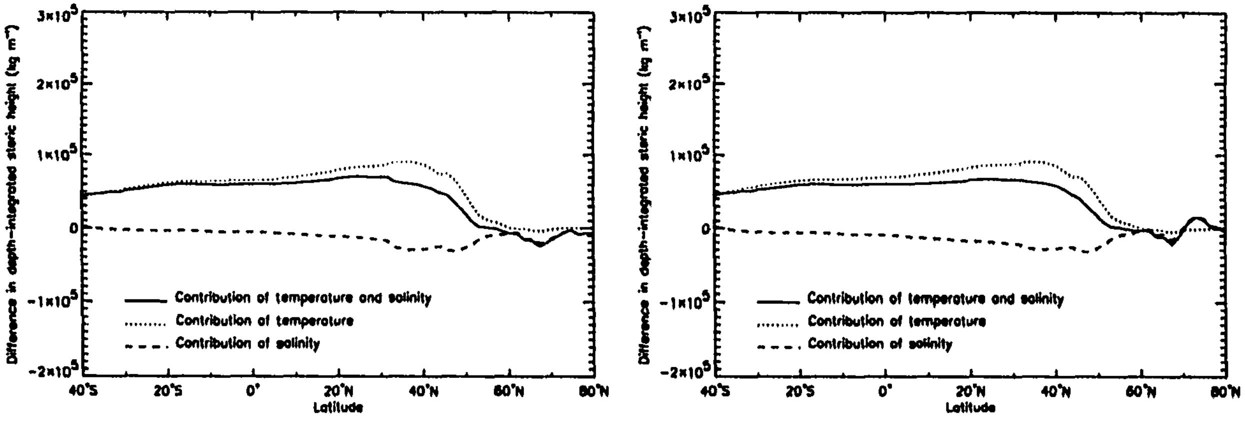

c 11 kaBP early stage (A3 minus A2; 200 years) d 21 kaBP early satge (A5 minus A4; 200 years)

Figure 3.6: **Effect of CO_2 on depth-integrated steric height under 11 kaBP and 21 kaBP orbital geometries. In the contribution of the temperature difference, positive value reflects warmer temperature, while negative value reflects colder temperature. In the contribution of the salinity difference, positive value reflects lower salinity while negative value reflects higher salinity.**

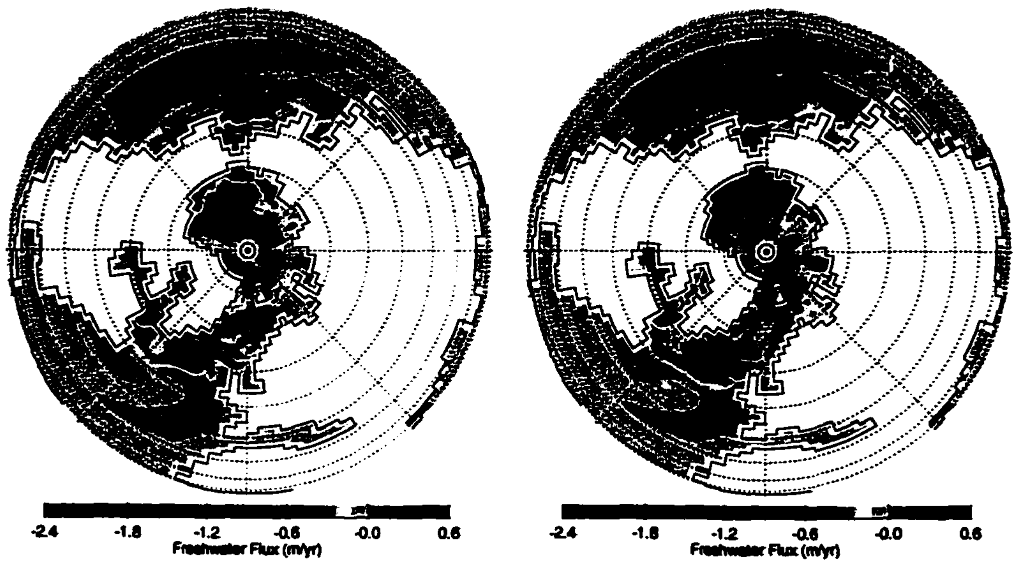

a Net downward freshwater flux under 11 kaBP orbit

b Net downward freshwater flux under 21 kaBP orbit

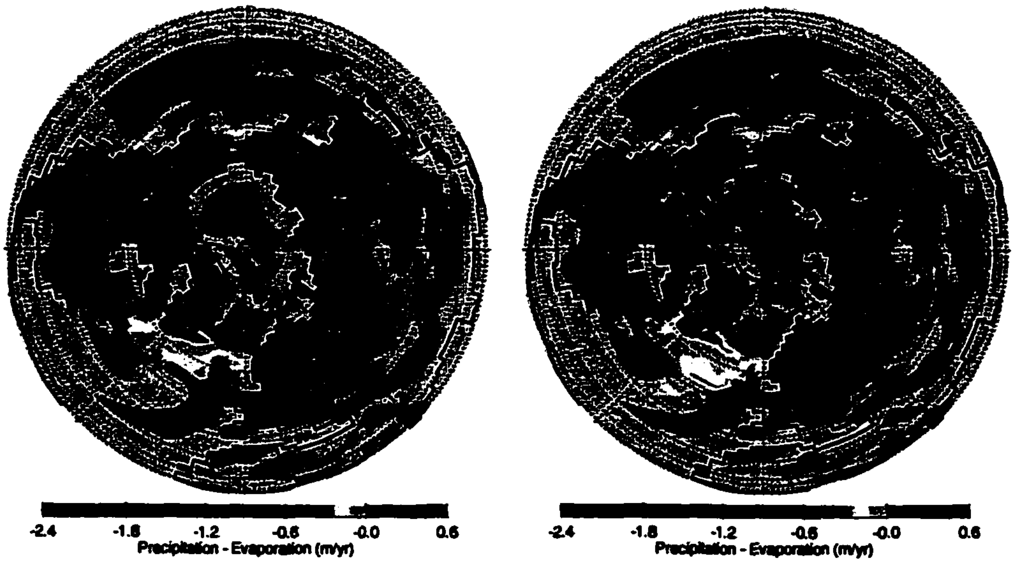

c Precipitation minus evaporation under 11 kaBP orbit

d Precipitation minus evaporation under 21 kaBP orbit

Figure 3.7: **Difference in annual mean, freshwater fluxes (m/yr) at the surface between 280 ppmv and 200 ppmv CO_2 forcing.**

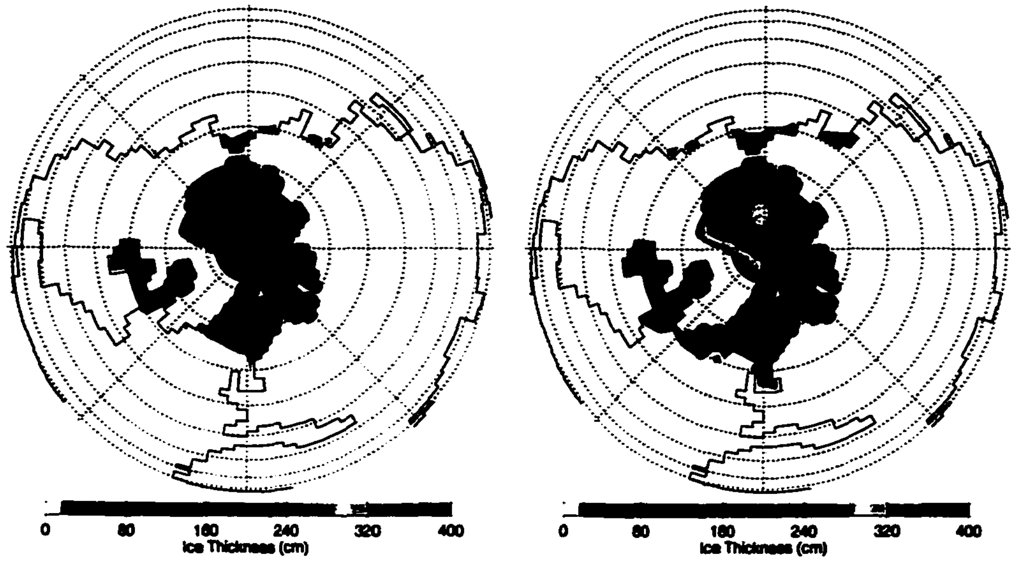

a 11 kaBP orbit and 280 ppmv CO_2 (A2) b 11 kaBP orbit and 200 ppmv CO_2 (A3)

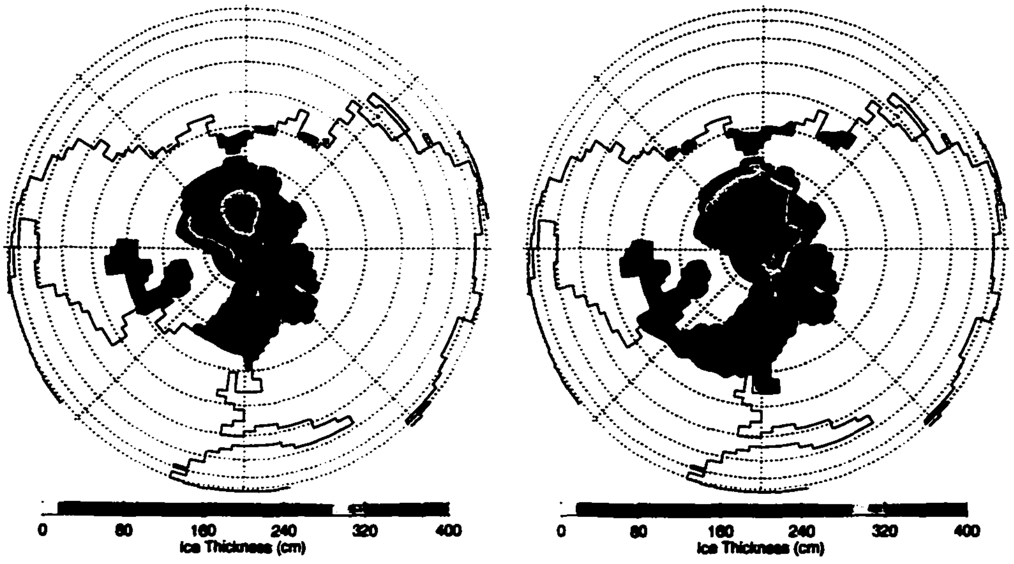

c 21 kaBP orbit and 280 ppmv CO_2 (A4) d 21 kaBP orbit and 200 ppmv CO_2 (A5)

Figure 3.8: **Simulated winter sea ice thickness. Here winter is defined as the period of 30 days following the winter solstice.**

terms of time, in which the Vernal Equinox is defined as March 21.

The annual mean response of global SST and the Atlantic meridional overturning to changes in orbital parameter is summarised in Table 3.5. The meridional overturning streamfunction in each experiment is displayed in Fig. 3.10a–3.10d. It is seen that the strength of the meridional overturning is affected most strongly by variations in precession, rather than obliquity.

Table 3.5: Annual mean response to orbital forcing

Experiments	Global SST (°C)	Atlantic meridional overturning ψ (Sv)
A6	16.6	9.9
A7	16.7	15.2
A8	16.3	11.3
A9	16.2	15.8

To identify the mechanism responsible for the maintenance of the meridional overturning at equilibrium, the depth-integrated steric height is again examined. Figure 3.11**a** shows the difference in equilibrium depth-integrated steric height between A7 and A6, representing the effect of the precessional change. Similarly, Fig. 3.11**b** shows the difference between A8 and A6, representing the effect of changes in obliquity. The depth-integrated steric height contributed by temperature differences in Fig. 3.11**a** show a large decrease between 30°S and the equator, and also near 60°N. The depth-integrated steric height difference contributed by the salinity difference shows a large increase between 30°S and the equator, almost a mirror image of the contribution of the temperature difference, and also a very large decrease near 60°N. The meridional gradient of depth-integrated steric height is maintained by the difference in the salinity field. There is no large meridional gradient seen in Fig. 3.11b, which is consistent with the little difference in the strength of the meridional overturning.

As in subsection 3.3.3, the depth-integrated steric height is also estimated during the early stages of integration. Figure 3.11c shows the difference between A7 and A6 at 300 years of integration, when the difference of the strength of overturning is only about 1.6 Sv. Similarly, Fig. 3.11d show the difference between A8 and A6 at 300 years of integration, when the difference of the strength of overturning is only about -0.3 Sv. A reference level of 1012 m (level 8 of the model) is adopted in both cases, once more accounting for the shallower overturning cell during the early stage. Similar to the equilibrium case, Fig. 3.11c shows that the meridional gradient of depth-integrated steric height is maintained

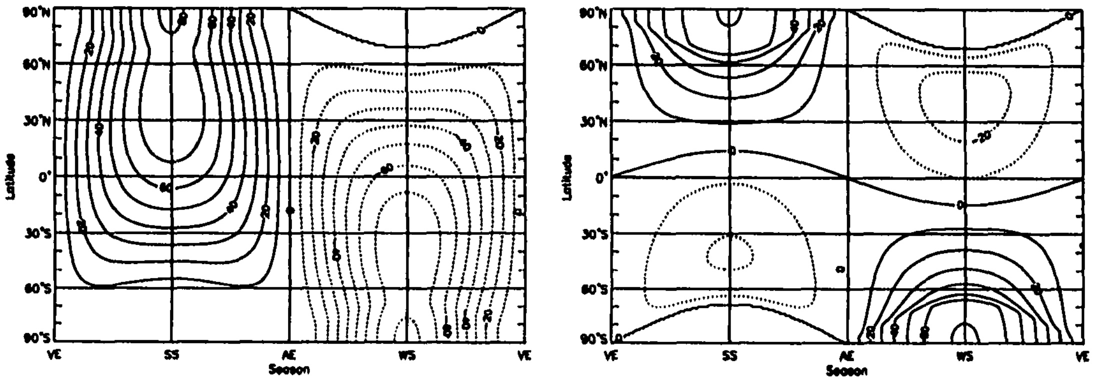

a Effect of precession (A7 minus A6) with respect to season

b Effect of obliquity (A8 minus A6) with respect to season

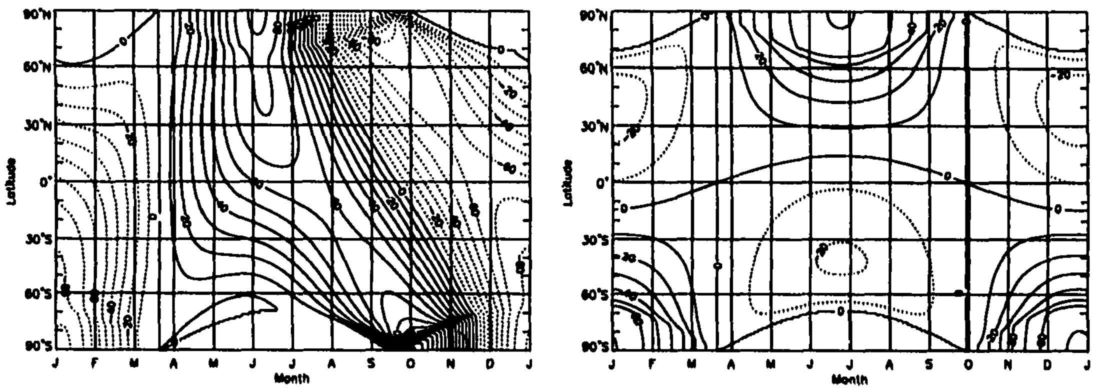

c Effect of precession (A7 minus A6) with respect to calendar

d Effect of obliquity (A8 minus A6) with respect to calendar

Figure 3.9: **The effect of orbital parameters on insolation (W m^{-2}). Contour interval is 10 W m^{-2}, and negative values are dotted. VE, SS, AE, and WS are respectively vernal equinox, summer solstice, autumnal equinox, and winter solstice in the NH.**

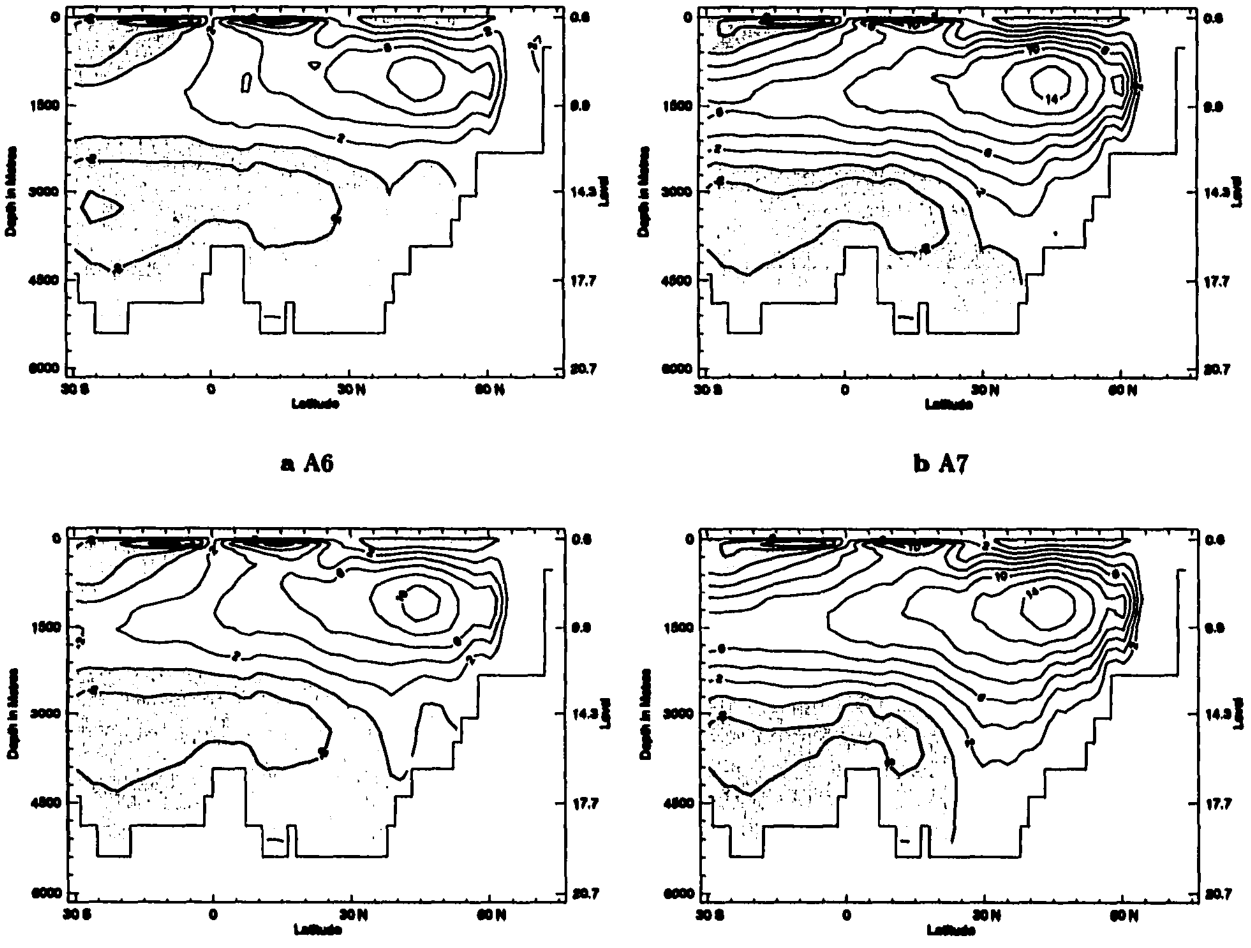

a A6

b A7

c A8

d A9

Figure 3.10: **Simulated annual mean zonally-averaged meridional overturning streamfunction in the Atlantic Ocean. Contour interval is 2 Sv (1 Sv $\equiv 10^6$ m^3 s^{-1}), and counterclockwise circulation is shaded.**

by the salinity difference. The most prominent feature is that the depth-integrated steric height contributed by the salinity difference and temperature difference are of opposite sign between the NH and SH in low latitudes. Between 40°S and 40°N, the temperature is colder in the SH and warmer in the NH; salinity is lower in the SH and higher in the NH.

It is apparent that the salinity difference is maintained by net moisture transport from NH low latitudes to SH low latitudes. To confirm this, the difference in specific humidity is shown in Fig. 3.12a. It is clearly seen that specific humidity increased in the NH and decreased in the SH, implying a decreased gradient between low and high latitudes and hence decreased moisture transport (see Eqs. 2.17 and 2.18) from low to high latitudes in the NH. In addition, an increased gradient and hence increased moisture transport from low to high latitudes occurs in the SH. This interhemispheric changes result in the increase in net moisture transport from NH low latitudes to SH low latitudes.

The changes in specific humidity noted above are a direct consequence of changes in SST (Fig. 3.12b). The colder upper layer in the SH is also reflected in the depth-integrated steric height in Fig. 3.11c. The cooling in the SH and warming in the NH is counter-intuitive, considering there is no net changes in annual mean insolation at any given latitude due to changes in precession. This can be explained by the monthly-varying planetary albedo. Even though net annual mean insolation is the same, seasonally-varying albedo under different seasonal insolation produces a difference in the total amount of absorbed shortwave radiation in a year. The insolation at the top of the atmosphere and absorbed shortwave radiation at the surface are shown in Figs. 3.13a and 3.13b. By comparing these figures as well as Fig. 3.11c and Fig. 3.11d, the reason why the thermohaline circulation is sensitive to the precession rather than obliquity in this model becomes clear: changes in precession produce asymmetric radiative forcing between the NH and the SH through prescribed planetary albedo, and hence produce a salinity contrast through the apparent net moisture transport from the NH to the SH. As a result, the meridional density and pressure gradient is maintained by the meridional salinity gradient. On the other hand, changes in obliquity produces symmetric radiative forcing and therefore produce no net moisture transport and hence no anomalous pressure gradient.

As is the case of CO_2 forcing, the large increase in salinity at about 60°N is maintained by the decrease in net downward freshwater flux at the corresponding latitudes, which is in balance with an increase in the Arctic (Fig. 3.14a). However, increased net moisture transport from the northern North Atlantic to the Arctic cannot be explained by the difference in the hydrological cycle between the experiments (Fig. 3.14b). A concurrent decrease of salinity and sea-ice thickness in the Arctic, and smaller winter sea-ice extent in the North

Atlantic (Figs. 3.15a and 3.15b), therefore, suggest that this salinification occurs through processes involving sea ice.

3.4 Discussion

One way to validate the climate model in terms of ocean circulation is to compare large scale features of a simulated equilibrium ocean to paleoceanographic reconstructions as well as to present-day observations. In this sense, the model used in this study gives some confidence as it captures important features of ocean circulation in both present-day and LGM simulations as described in Weaver et al. (1998; 2001) and in this chapter. However, some discrepancies exist. In the present-day simulation, the insufficiently resolved Gulf Stream separates from the coast too far north and does not penetrate enough into the GIN Seas. Consequently, the ocean carries much less warm and saline water to the north than observed. The resulting cold surface ocean allows for ice cover over the Norwegian Sea where no seasonal ice cover exists in reality, and the fresh surface ocean forces deep water formation to occur too far south. One important question to be considered is whether the results obtained in this study will change if the discrepancy between the present-day simulation and observations, i.e., excess ice in the northern North Atlantic, does not exist.

The mechanism proposed in this study implicates an important role for changes in sea ice cover through freshwater transport variations resulting from changes in the amount of formation, advection, and melting of sea ice. However, the northeastward penetration of Gulf Stream-North Atlantic Current system, and the northward shift of the ice edge and deep water formation region do not necessarily preclude the mechanism that stronger overturning produces less ice cover. Also, as a proper representation of sea ice cover should accompany a proper representation of the deep water formation region, it is expected to result in the northward shift of the whole system involved in the mechanism proposed here although the same mechanism should work. More importantly, changes in the thermohaline circulation are first excited by the meridional temperature gradient in both the case for CO_2 and for orbital forcing, and they are not associated with a particular geographic constraint. Therefore, it is likely that the proposed mechanism would occur in the model with a properly simulated northern North Atlantic, although the magnitude of the change in the Atlantic meridional overturning might be slightly different.

In all experiments in this study, ice sheets (e.g., Laurentide and Fennoscandian) were not prescribed even though they were known to exist. Weaver et al. (1998) investigated the effect of the ice sheet albedo at the LGM on the thermohaline circulation, and showed that it

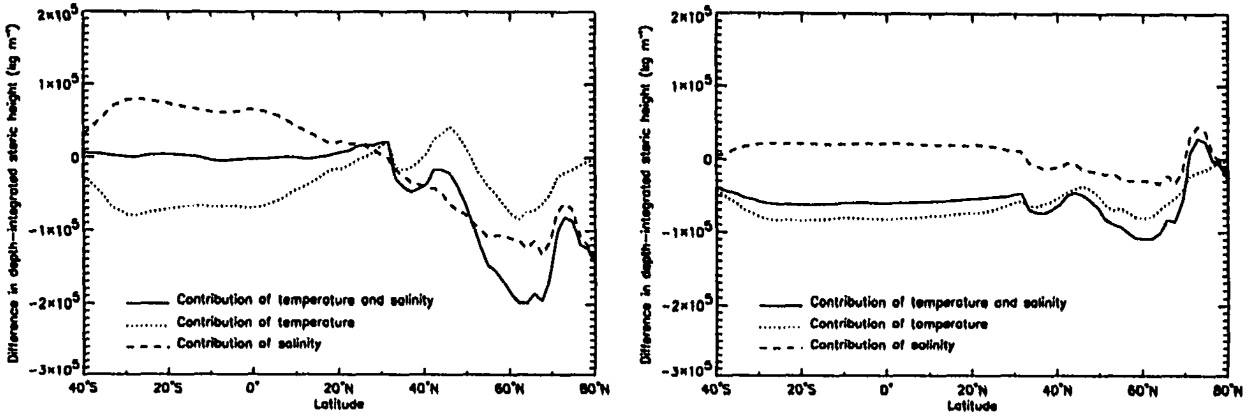

a Equilibrium (A7 minus A6; 2000 years)   **b** Equilibrium (A8 minus A6; 2000 years)

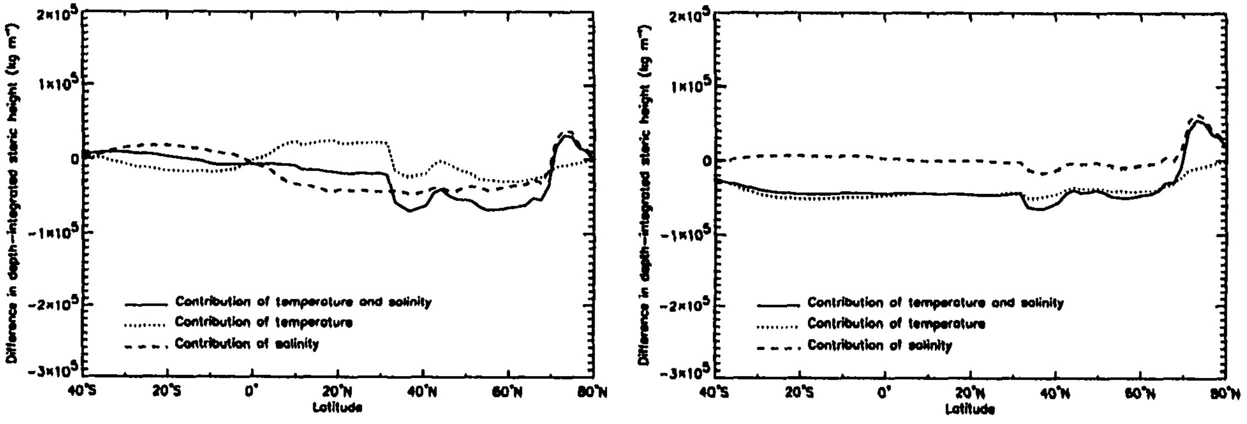

c Early stage (A7 minus A6; 300 years)   **d** Early stage (A8 minus A6; 300 years)

Figure 3.11: **Effect of precession and obliquity on depth-integrated steric height.**

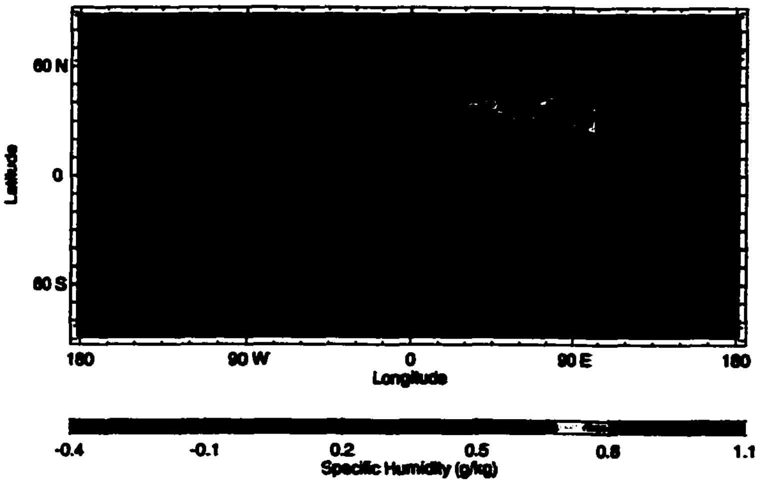

a Difference in specific humidity (g/kg)

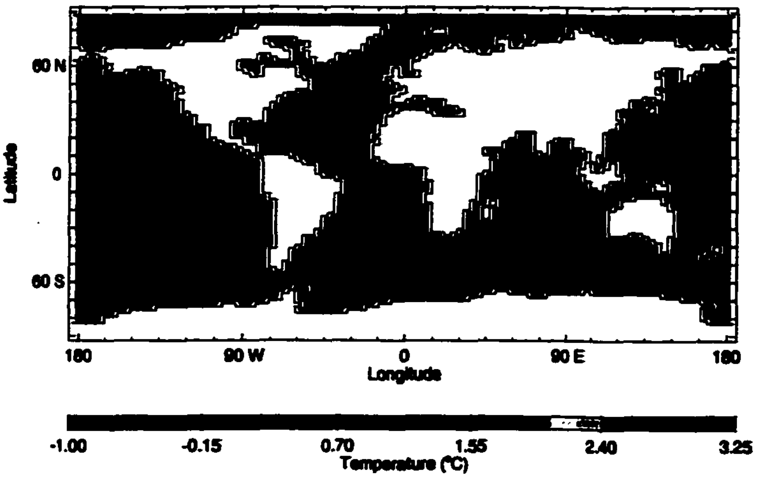

b Difference in sea surface temperature (°C)

Figure 3.12: **Effect of precession (A7 minus A6) on the contrast between the annual mean NH and SH responses at the early stage of integration (300 years).**

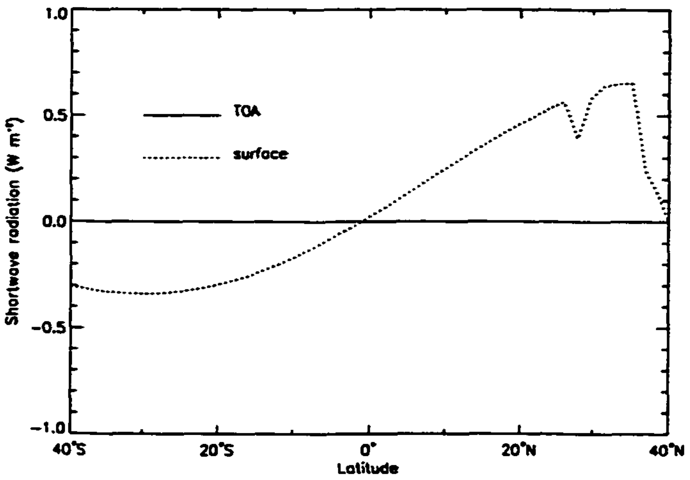

a Effect of precession

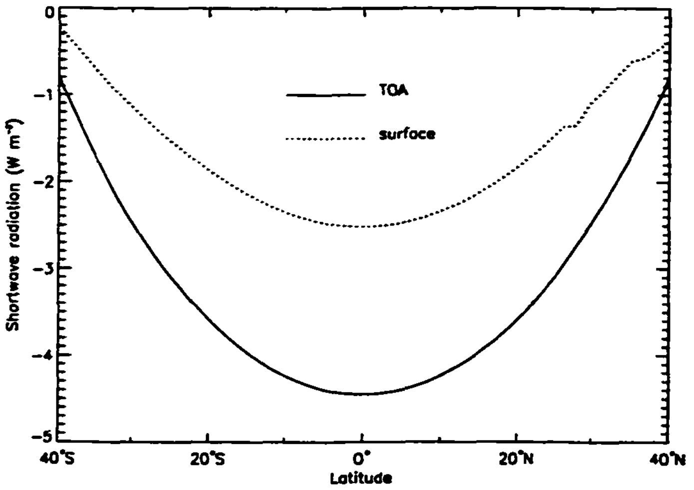

b Effect of obliquity

Figure 3.13: **Annual mean insolation at the top of the atmosphere and absorbed shortwave radiation at the surface (300 years).**

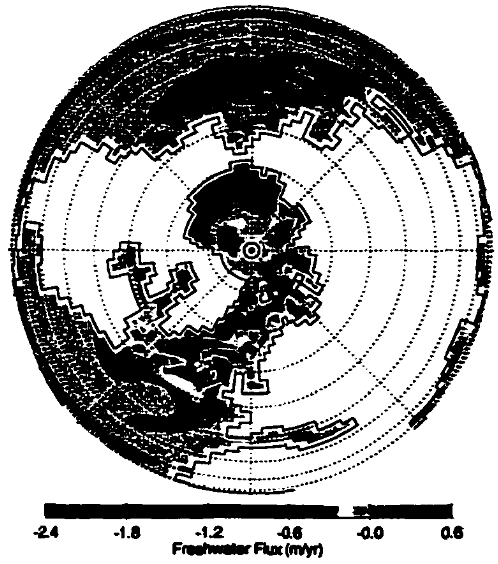

a Net downward freshwater flux

b Precipitation minus evaporation

Figure 3.14: **Difference in annual mean, freshwater fluxes (m/yr) at the surface between A7 and A6.**

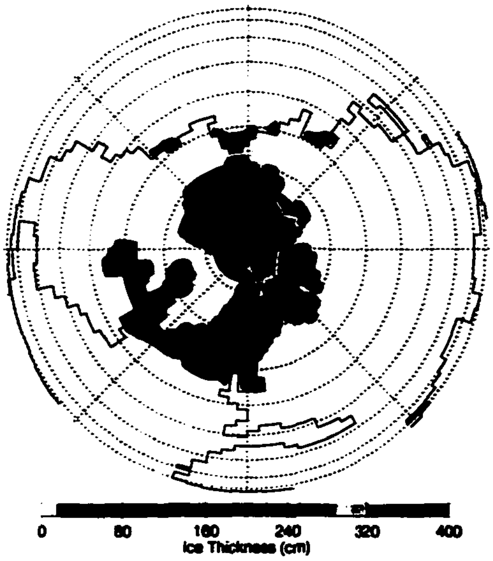

a A6

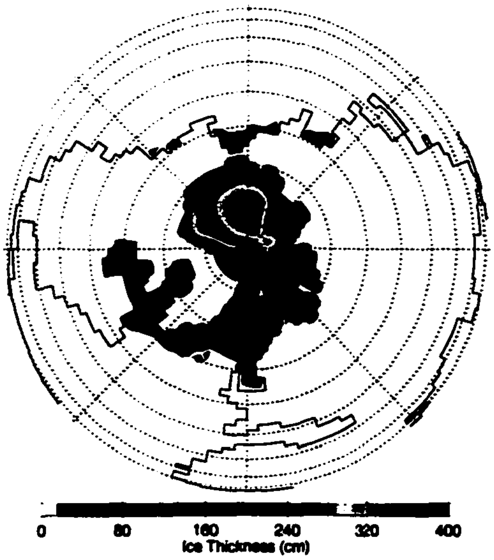

b A7

Figure 3.15: **Simulated winter sea ice thickness. Here the definition of winter is the same as Fig. 3.8.**

was small. As the effect of ice sheets on the thermohaline circulation is due to local cooling through albedo feedback, even smaller ice sheets that occurred at 11 kaBP are expected to have even smaller effect. Therefore, the results obtained in this study should not largely be affected by the specification of ice sheets. There remains the possibility, however, that ice sheets would affect the thermohaline circulation if a dynamical atmospheric model, instead of diffusive atmospheric model, were to have been used. For example, more than 15°C cooling in the vicinity of the Labrador Sea was found in Manabe and Broccoli (1985) and Broccoli and Manabe (1987). In these studies, the Laurentide ice sheet blocked and split the mid-tropospheric jet into northern and southern branches, producing the advection of cold air from the north over the North Atlantic. However, the impact of this cooling on the thermohaline circulation and the magnitude of this cooling itself are not clear as their model did not resolve the thermohaline circulation. The ice sheet topography prescribed in their studies (CLIMAP 1981) also likely overestimates the elevation (Peltier 1994). In addition, the eastward shift of storm tracks is persistently observed in many models (Kageyama et al. 1999). Although the simulated magnitude of the shift and changes in intensity are still model-dependent, the effect of the associated changes in precipitation on thermohaline circulation deserves to be investigated. Furthermore, meltwater and river re-routing, changes in ice calving rate, and the transport and melting of icebergs also have the potential to affect the thermohaline circulation — all of these are neglected in this study. The inclusion of the effect of meltwater discharge requires the synchronous coupling of both climate and ice sheet models with a complete and closed moisture cycle. The inclusion of the effect of river re-routing and the treatment of icebergs requires additional components — i.e., hydraulic and iceberg-drift models.

It has been shown that the thermohaline circulation responds to a CO_2 perturbation in a nonlinear fashion. Under the 11 kaBP orbital configuration, the reduction of CO_2 by 80 ppmv, from 280 ppmv to 200 ppmv, led to a North Atlantic meridional overturning that was reduced by about 25% relative to the present. Similarly, under the 21 kaBP orbital configuration, the same reduction of CO_2 caused about a 40% reduction in the meridional overturning. On the other hand, the thermohaline circulation did not show any significant changes due to a reduction of CO_2 by 70 ppmv, from present-day levels (350 ppmv) to 280 ppmv. The nonlinearity of the radiative forcing of CO_2 alone could not explain this result and it suggests the existence of a threshold level of forcing, between pre-industrial (280 ppmv) and full glacial (200 ppmv) CO_2 levels, past which a reduction of the meridional overturning occurs for further reduction in atmospheric CO_2. This is a plausible explanation for the nonlinearity considering that the thermohaline circulation possesses strong positive feedback mechanisms: 1) oceanic salt advection; 2) atmospheric heat transport; and 3) atmospheric moisture transport (Rahmstorf et al. 1996; Marotzke 1996). The last two mechanisms function in such a way that the meridional ocean temperature contrast decreases as the thermohaline circulation increases, and hence the atmospheric meridional temperature contrast, which drives heat and moisture transport in the atmosphere, decrease.

Although oceanic heat transport is, in general, considered to be a negative feedback, as increased heat transport reduces the meridional temperature and hence density gradient, it is suggested in this study that this could also work as a positive feedback through an interaction of sea ice. Also, the idea of an existing threshold is consistent with an another example of how the robustness of the thermohaline circulation depends on its initial (control-run) strength, which Weaver et al. (1998) discussed in detail in their paper. Furthermore, the fact that little difference was observed in the strength of the meridional overturning between 11 kaBP and 21 kaBP orbital cases under 280 ppmv CO_2, is explained by this threshold hypothesis such that the threshold lies below 280 ppmv CO_2, and hence the thermohaline circulation is too stable to be affected by orbital forcing (precessional forcing). As mentioned earlier, the difference between 11 kaBP orbit and 21 kaBP orbit under 200 ppmv CO_2 is explained by the difference in precession. These arguments lead to the statement that under 11 kaBP orbital conditions, the thermohaline circulation is more stable than under 21 kaBP orbital configuration.

It was also shown that the thermohaline circulation responds to precessional forcing through meridional asymmetry in absorbed shortwave radiation at the sea surface, which is determined by the prescribed planetary albedo. Since there is no ice cover in low and mid latitudes, the planetary albedo there is determined from present-day observations. Therefore, it is not model dependent and other models with prescribed planetary albedo should experience similar meridional asymmetry in the absorbed shortwave radiation at the surface. It is unfortunate that the thermohaline circulation is sensitive to the planetary albedo, and hence cloud albedo, as it is the largest uncertainty in any model including atmospheric GCMs. Uncertainties arise from the use of the observed planetary albedo even under different forcing from the present and the prescribed variation of planetary albedo with calendar date rather than season, both of which are commonly applied in paleoclimate modelling. The interpretation of results gained from the experiments with prescribed planetary albedo, therefore, requires some caution.

It is worthy to address the existence of multiple equilibria for a complete description of the behaviour of thermohaline circulation under CO_2 and orbital forcing. The existence of multiple equilibria is usually investigated using perturbations of the freshwater fluxes at high latitudes. A gradual change in freshwater flux, such that the ocean can continually adjust its equilibrium state, generally leads to a hysteresis curve in phase space of freshwater (buoyancy) flux and the meridional overturning strength. The hysteresis curve then illustrates the possible stable states for thermohaline circulation. The model used in this study is known to have two stable equilibria under both present-day and LGM forcing (Schmittner et al. 2001). Under present-day forcing, they are the one simulated in this study (A1: ~20 Sv) and the total collapse of thermohaline circulation. Similarly, under LGM forcing, there are the one simulated in this study (A5: ~10 Sv) and the total collapse of thermohaline circulation. Although no such study has been conducted under largely different orbital forcing from the present-day (or under the perturbation of orbital parameters or atmospheric CO_2 concentration, rather than freshwater flux), it seems difficult for this model to have multiple equilibria other than the total collapse of thermohaline circulation.

3.5 Conclusion

To investigate the response of the thermohaline circulation to changes in atmospheric CO_2 concentration and orbital geometry during the last deglaciation, the coupled climate model was integrated under different sets of external forcing. It was shown that the thermohaline circulation can be greatly affected by both CO_2 and orbital forcing. The thermohaline circulation responds to CO_2 forcing in a nonlinear fashion, and the existence of a threshold value between 280 ppmv and 200 ppmv for the destabilisation is found. As the thermohaline circulation is closely linked to the oceanic heat transport and global carbon cycle, this result should have large climatic implications.

During the last glacial termination, the CO_2 level rose from 200 ppmv to 280 ppmv. This increase of CO_2 first warms up the ice-free ocean, producing a meridional temperature gradient between the ice-free ocean and the seasonally ice-covered ocean. This temperature gradient is felt by the ocean as a pressure gradient force, strengthening the meridional overturning. As the meridional overturning increases, the ice edge in the northern North Atlantic retreats northward, locally reducing the winter ice cover and summer melting of sea ice, and increasing the net moisture transport from the northern North Atlantic to the Arctic. The saltier water in the northern North Atlantic reduces the meridional salinity gradient and this results in a further strengthening of the meridional overturning.

During the last glacial termination, the orbital geometry changed as well. The two extreme orbital configurations are represented by the 21 kaBP and 11 kaBP orbital configuration. Changes in precession, and hence seasonal redistribution of insolation, cause differences in annually-absorbed shortwave radiation at the sea surface through seasonally-varying planetary albedo, despite the fact that the annual mean insolation at the top of the atmosphere at any given latitude does not change. The resulting cooling in mid latitudes of the SH increases the meridional gradient in specific humidity and hence moisture transport from low to mid latitudes, while warming in mid latitudes of the NH decreases the meridional gradient in specific humidity and hence moisture transport from low to mid latitudes. As a result, the salinity decrease in the SH and increase in the NH lead to an increase in the meridional density and pressure gradient which enhances the meridional overturning. As is the case of CO_2 forcing, a similar positive feedback associated with decreased sea ice extent and further strengthening of the meridional overturning, was found.

Chapter 4

Glacial termination: Changes in climate and ice sheet

4.1 Introduction

It is well established that global ice volume and atmospheric CO_2 concentrations varied inversely on glacial-interglacial time scales such that CO_2 level decreased as glaciation progressed and increased during deglaciations (Barnola et al. 1987; Imbrie et al. 1984; Jouzel et al. 1993; Raynaud et al. 1993). As mentioned in Chapter 1, global ice volume has been constructed from oxygen isotope ratios in marine sediment cores while the atmospheric CO_2 concentration is derived from ice cores. Consequently, difficulty exists in addressing the precise phase relationship between them, due to dating uncertainties in each record. It is, therefore, of great use if one can compare both signals from the same record (Sowers et al. 1991).

The atmospheric O_2 created as a byproduct of photosynthesis has the similar isotopic composition of plant water. This water is ultimately derived from surface water of the ocean through hydrological processes (Broecker and Henderson 1998). The oxygen isotope ratio of surface water of the ocean today is, on average, close to that of the mean ocean water (Bender et al. 1994). As mentioned in Chapter 1, the oxygen isotope ratio of the mean ocean water is largely controlled by global ice volume. Therefore, the oxygen isotope ratio in air trapped in the ice ($\delta^{18}O_{atm}$) should respond to changes in global ice volume on a time scale of the turnover time of O_2 in the atmosphere, which is about 1.2 ka (Broecker and Henderson 1998). The complication arises, however, because the isotope fractionation occurs during photosynthesis, respiration, and hydrological processes. The deviation of the oxygen isotope ratio of atmospheric O_2 from that of sea water due to this fractionation is called the Dole effect. The variations of $\delta^{18}O_{atm}$ during glacial-interglacial cycles have, therefore, contributions from both changes in global ice volume and the Dole effect.

Bender et al. (1994) estimated the magnitude of the Dole effect during the last 130 ka by taking the difference in oxygen isotope ratio between atmospheric O_2 in the Vostok ice core and sea water derived from marine sediment cores ($\delta^{18}O_{sw}$). Although the details of variations in the Dole effect are rather sensitive to relative errors in the ages of the two records, they concluded that changes in oxygen isotope during the last glacial cycle are attributed to changes in global ice volume based on the small variability in the Dole effect. Further support for the validity of $\delta^{18}O_{atm}$ as a proxy for global ice volume is given by Broecker and Henderson (1998), showing that a similar lag between dust flux and $\delta^{18}O_{atm}$ in an ice core is also seen between dust flux and $\delta^{18}O_{sw}$ in a marine sediment core.

The Vostok ice core during the penultimate deglaciation clearly shows that the $\delta^{18}O_{atm}$ lags behind the CO_2 change (Jouzel et al. 1993; Sowers et al. 1991; Sowers and Bender 1995). Broecker and Henderson (1998) estimated that the lag of global ice volume to CO_2 was about 2 ka during the last deglaciation and about 4 ka during the penultimate deglaciation. A recent extension of the Vostok ice core record back to 420 kaBP show similar lags and leads over the last four terminations (Petit et al. 1999).

From these studies, it is apparent that increases in atmospheric CO_2 concentration likely lead deglaciations. The important questions to be answered as a next step for understanding of the climate system are: 1) which mechanism is responsible for the increase of CO_2 level; 2) is the CO_2 forcing triggered by orbital forcing important in deglacial processes? and if so, how much is attributed to CO_2 forcing? Although it is not yet conclusive, the first question has been intensively studied (e.g., Broecker and Peng 1993; Broecker and Henderson 1998; Archer et al. 2000; Sigman and Boyle 2000). On the other hand, few studies, if any, have been conducted regarding the second question. In this chapter, the importance of orbital and CO_2 forcing during the last deglaciation is explored.

In this study, the coupled climate model of Chapter 3 is again used. An earlier version of the model was used by Weaver et al. (1998) to study the relative importance of orbital forcing, ice albedo due to the presence of ice sheets, and carbon dioxide at the LGM. The lack of land ice dynamics in the earlier version of the climate model, however, restricted its application to the study of permanent snow cover (surface mass balance) and prevented the study of ice sheet growth, decay or maintenance (ice column mass balance). The latter is also important as it provides a means of validating the climate model. Removing these restrictions and extending the approach of Weaver et al. (1998), a continental ice dynamics model is coupled to the climate model. An asynchronous coupling strategy is taken and the coupled climate-ice sheet model is integrated under perpetual forcing. Experiments and sensitivity analyses are conducted to address: 1) model performance under present-day, 11 kaBP, and 21 kaBP perpetual forcing; and 2) the ice sheet response to changes in orbital geometry and atmospheric CO_2 concentration, and hence the relative importance of orbital and CO_2 forcing during the last deglaciation. Particular emphasis is given to the interaction with the thermohaline circulation.

4.2 *Coupling of the ice sheet model*

The ice sheet consists of snow, firn, and glacier ice, each having a different characteristic density. Firn is referred to as old snow that has become granular and compacted as the result of surface metamorphoses (Glickman 2000). Firn becomes glacier ice when the interconnecting air passage between the grains are sealed off. Transformation from firn to glacier ice typically occurs at the depth of 60–70 m and 100–300 years after the deposition (Paterson 1994). Since layers of snow and firn are generally much thinner than that of glacier ice, and as deformation of ice mainly occurs near the base, snow is safely assumed, in the model, to be instantly transformed to glacier ice after it falls, without experiencing an intermediate stage as firn. This holds since only the dynamical behaviour of the ice sheet is accounted for.

In reality, accumulation is given by snowfall, blown snow, avalanches, deposition of water vapour in the atmosphere, freezing of rain, and refreezing of melt water, whereas ablation occurs by surface and basal melting, removal of snow by wind, sublimation and iceberg calving. It is assumed that the dominant contributors for mass balance are snowfall, surface melting and calving. Note that basal melting could be important for floating ice (Paterson 1994), but it is not allowed in the model. Infinite calving is, instead, assumed over the ocean. That is, all ice pushed to the ocean is calved and melts instantly. Adaptation of this treatment comes from the poor understanding of the quantitative aspects of the calving mechanisms as well as technical difficulties associated with the interaction with the sea ice model, rather than insignificance of the calving mechanism per se. Hudson Bay is changed to land for the paleo-simulations. As mentioned in Chapter 2, snowfall and surface melting are predicted in the EMBM.

In central Greenland, the accumulation rate today is about 250 mm a^{-1} while in central East Antarctica it is about 25 mm a^{-1} (Paterson 1994). A typical horizontal velocity for ice sheets is 1–10 m a^{-1}, while that of ice streams is 10's–100's m a^{-1} (Marshall 1998). Because of this slow characteristic time of ice sheets relative to other climate system components, an asynchronous coupling strategy is adopted to integrate the coupled climate-ice sheet model. Note that the integration speed of the climate model is about 2000 years per CPU month on the fastest IBM SP2 nodes available for this study. When coupled, the climate model is integrated for 10 years, the net surface accumulation is averaged over this period, and passed to the CIDM as a boundary condition. The CIDM is then integrated for 2000 years and the averaged ice thickness and surface elevation fields are returned to the climate model. This cycle is repeated until both models reach quasi-equilibrium. The overview of the model integration procedures are illustrated in Figs. 4.1a and 4.1b.

When the ice sheet model is asynchronously coupled to the climate model, a different treatment of moisture flux between components is employed (Figs. 4.2a and 4.2b). All precipitation occurring over land in the EMBM is passed instantaneously to the oceanic component regardless of whether it is rain or snow. However, to allow for ice sheet growth, snow is also passed to the CIDM. This implies that the resulting meltwater is not passed to the oceanic component since the snow, the source of the meltwater, was already passed as runoff to the oceanic component when it fell. This treatment is necessary due to the use of the asynchronous coupling. In a segment of CIDM integration (in 2000 years) ice may unrealistically pile up due to differences between the prior climate (the imposed 10-year EMBM integration) and the present climate. Similarly, the EMBM has no limitation on the amount of surface melting as long as ice exists. Therefore, it is possible that the ice accumulated for 2000 years in the warm climate through transport from the colder climate, melts away during one segment of the EMBM integration, i.e., in 10 years. This could cause the oceanic component to become unstable due to unrealistic massive freshwater discharge. The other reason is to allow arbitrary initial conditions for ice thickness. For example, this prevents the oceanic component from becoming unstable due to flooding even when the LGM ice sheets are imposed as an initial condition in an incompatibly warm climate, which is inevitable for sensitivity experiments under perpetual forcing. A disadvantage of this approach is that it results in a different seasonal distribution of runoff, while conserving local total amount of runoff within a year, from the case in which the climate model is run without the CIDM. However, it is confirmed, during the experiments, that it has no significant effect on ocean circulation in the model. Note that a complete closed hydrological (moisture) cycle within the couple climate-ice sheet model, rather than only climate model, is possible and should be applied during the synchronous coupling (Schmittner et al. 2001).

In summary, the net surface accumulation is calculated in the EMBM and passed to the CIDM. Ice thickness and surface elevation are then calculated in the CIDM and passed to the EMBM. There is no direct exchange of freshwater between the CIDM and the oceanic component. As a result, the total amount of moisture is strictly conserved within the atmosphere-ocean-sea ice component of the climate model. Therefore, the model does not include either the effect of changes in continental ice volume on the ocean mean salinity, or the effect of the meltwater discharge on the ocean circulation. These two effects are

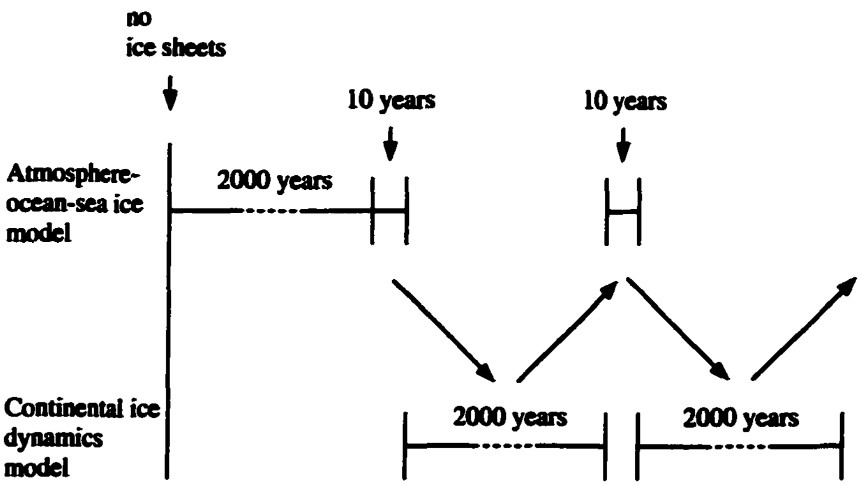

a Present-day simulation (A1)

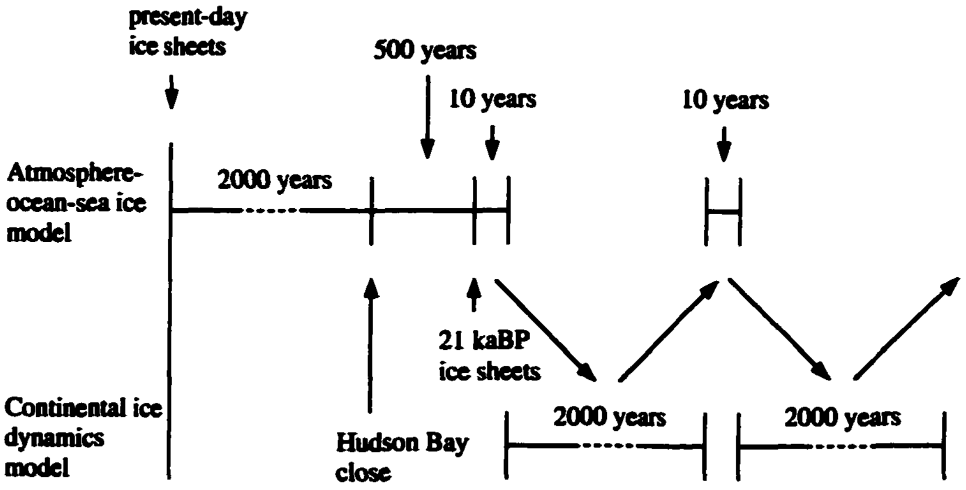

b Paleoclimate experiments (A2–A5)

Figure 4.1: **Model integration procedure.**

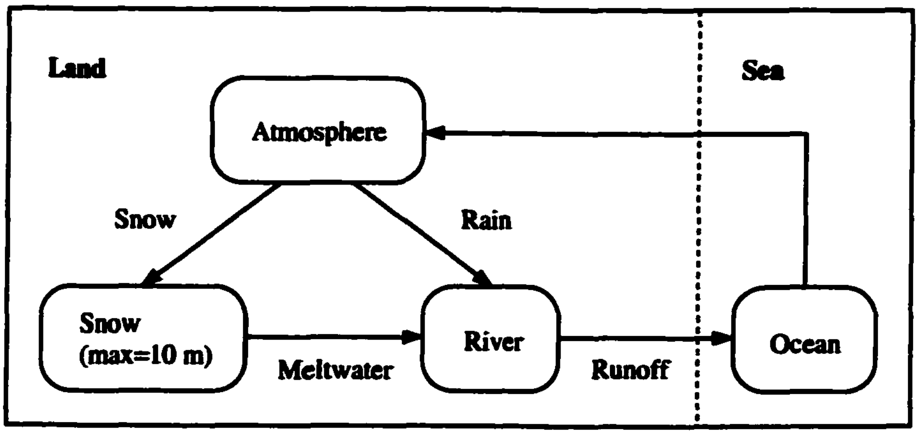

a Without the ice sheet model

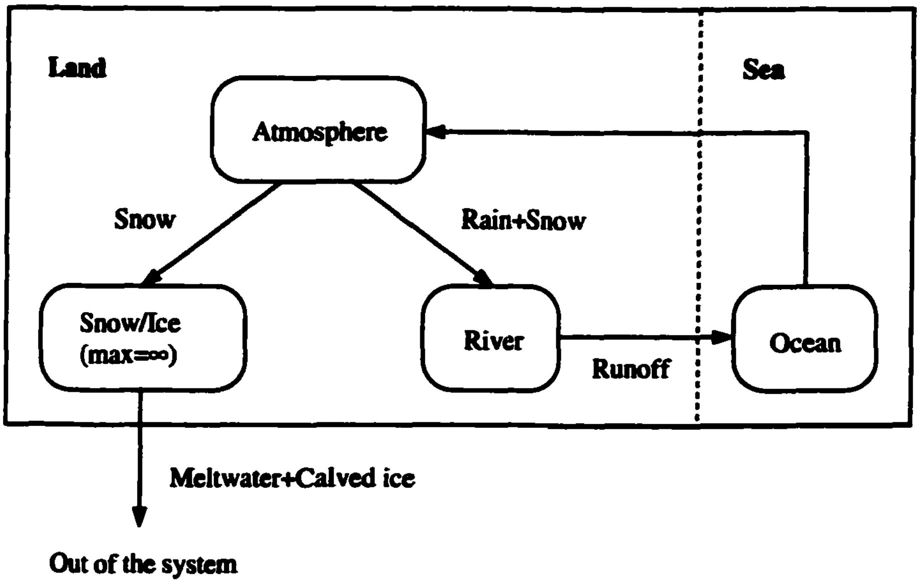

b With the ice sheet model

Figure 4.2: **Flow of moisture between the components of the climate model.**

not the target of the sensitivity experiments conducted in this study, although adoption of the synchronous coupling between subcomponent models, for use in transient glaciation/deglaciation studies, makes it possible to incorporate these effects.

4.3 Experimental design

The same experimental design as Table 3.1 in Chapter 3 was employed for the coupled climate-ice sheet model. The equilibrium climate of the 2000 year integrations of the climate model conducted in Chapter 3 were analysed and are referred to as climate model response.

To explore the performance of the coupled climate-ice sheet model, a present-day simulation was conducted starting from the present-day equilibrium of the climate model through the following procedure: 1) the topography over Greenland and Antarctica was changed from present-day surface elevation to the present-day bed elevation; 2) bedrock was uplifted by about one-third of the present-day ice thickness of Greenland and Antarctica, taking the isostatic adjustment into account; and 3) the asynchronously coupled ice sheet model was integrated for 400 ka to reach quasi-equilibrium, requiring an additional 2000 years of climate model integration. Note that no initial ice was specified over land. Following the approach of Marshall (1996) and assuming that the present-day topography is in isostatic equilibrium, the uplift of bedrock Δh_b is given by

$$\Delta h_b = r_\rho H_i \tag{4.1}$$

where r_ρ is, as in Chapter 2, the ratio of ice density to bedrock density.

After the model performance was evaluated, sensitivity experiments were conducted under four different sets of forcing from four different initial climatologies obtained from the climate model spin-ups. These were accomplished as follows: 1) Hudson Bay was changed to land; 2) the climate model was integrated for another 500 years until the perturbation caused by procedure 1) was settled; 3) the bedrock was depressed by about half of the difference of thickness between 21 kaBP and the present-day surface elevation given by Peltier (1994), taking the isostatic adjustment into account; 4) the difference between the LGM ice thickness and the present-day ice thickness was added; and 5) the asynchronously coupled ice sheet model was integrated under four different sets of forcing (combination of 11 kaBP or 21 kaBP orbital and 200 ppmv or 280 ppmv CO_2 forcing) for 100 ka, which corresponds to 500 years in the climate model.

Again, following the approach of Marshall (1996) and assuming the LGM topography is in isostatic equilibrium, the depression of bedrock is given by:

$$\Delta h_b = -\frac{r_\rho}{1 - r_\rho} \Delta h_s, \tag{4.2}$$

where Δh_s is the surface elevation difference between 21 kaBP and the present-day. The difference between the LGM ice thickness and the present-day ice thickness, ΔH_i is given by:

$$\Delta H_i = \Delta h_s - \Delta h_b. \tag{4.3}$$

4.4 Results

In subsection 4.4.1, the response of the model without ice dynamics to the five different sets of radiative forcing is described (Table 3.1). In particular, the differences in SAT and precipitation, which are important for the mass balance of ice sheets, are discussed. In subsection 4.4.1, the model is integrated without specifying any ice sheets except the present-day Greenland and Antarctic ice sheets, which are implicitly incorporated by using the present-day surface elevation. Therefore, the effect of other ice sheets that existed during the last deglaciation, such as the ice-albedo feedback, is not included. In subsection 4.4.2, the response of the model to the same five different sets of radiative forcing is described as in subsection 4.4.1, but now with an interactive CIDM included.

4.4.1 Climate model response

The orbital geometry at 11 kaBP is characterised by a larger obliquity than today and a perihelion near the NH summer solstice (Table 3.2), both intensifying NH summer seasonality. The resulting distribution of insolation shows a strong positive anomaly relative to the present in the NH high latitudes during the NH summer, and a compensating negative anomaly in the SH low and mid latitudes during the SH summer (Fig. 4.3a). The major difference in orbital geometry between 21 kaBP and today is the magnitude of obliquity (Table 3.2). The small obliquity at 21 kaBP results in less insolation at high latitudes in both hemispheres during their respective summers (Fig. 4.3b). The magnitude of the deviation, however, is small and the effect is not generally important (e.g., Weaver et al. 1998). For reference, the distribution of insolation relative to the present, in terms of the calendar date, is shown in Figs. 4.3c and 4.3d.

SAT is closely related to the mass balance of ice sheets through its effect on melting

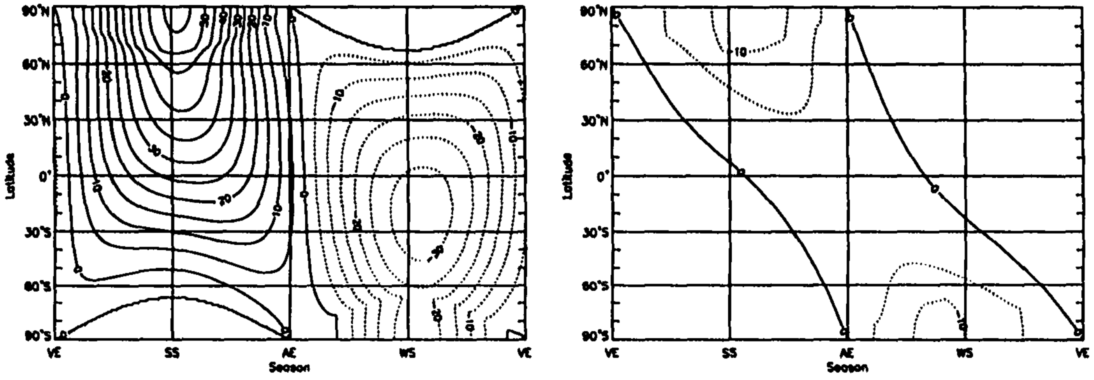

a 11 kaBP with respect to season

b 21 kaBP with respect to season

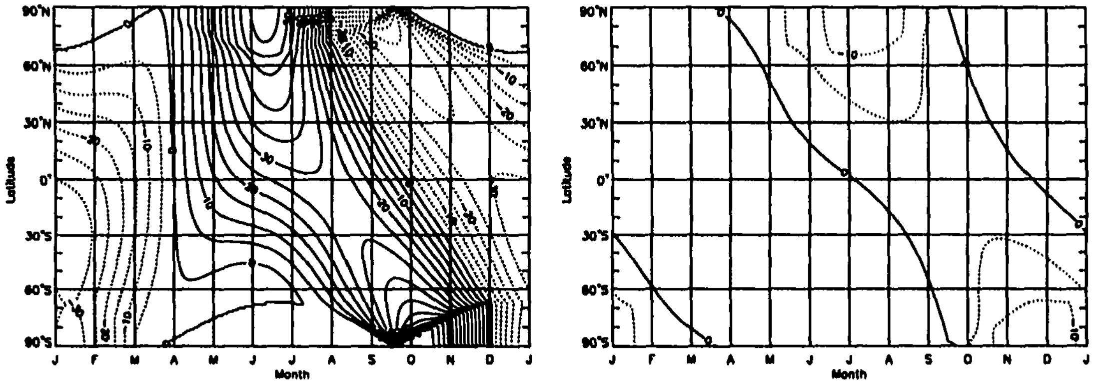

c 11 kaBP with respect to calendar date

d 21 kaBP with respect to calendar date

Figure 4.3: **Insolation at the top of the atmosphere relative to the present (W m^{-2}). Contour interval is 5 W m^{-2}, and negative values are dotted. VE, SS, AE, and WS are respectively vernal equinox, summer solstice, autumnal equinox, and winter solstice in the NH.**

rate, saturation specific humidity, and fraction of snowfall in precipitation. The annual mean, global SAT is summarised in Table 4.1. It is seen that globally-averaged SAT is determined by atmospheric CO_2 concentration rather than orbital geometry. This is not surprising because the globally- and annually-integrated insolation is virtually unaffected by the orbital parameters. Figures 4.4a and 4.4c show the simulated annual mean SAT relative to the present under 11 kaBP and 21 kaBP orbital forcing, respectively, when 280 ppmv CO_2 is imposed. Since the difference in insolation between 21 kaBP and the present is small, the common features seen in both cases are attributed to the lowered CO_2 concentration relative to the present-day simulation (280 ppmv relative to 350 ppmv). These are the globally colder climates (1.1–1.2°C) and the large cooling in polar regions, especially along the coast of Antarctica. The latter suggests a high sensitivity of sea ice and oceanic convection to the CO_2 forcing.

Results for the same experiments, but specifying 200 ppmv CO_2 instead of 280 ppmv, are shown in Figs. 4.4b and 4.4d. Again, the globally colder climates (2.8–2.9°C) compared to the present-day simulation in both cases, are explained by the CO_2 difference of 150 ppmv. Note that the global cooling of 2.8°C under 21 kaBP orbit increases to 3.2°C and 3.6°C through the inclusion of the effect of ice albedo and the effect of both ice albedo and increased elevation associated with the LGM ice sheets, respectively (Weaver et al. 2001). The most outstanding feature is the significant cooling over North America and western Europe, with a peak in the northern North Atlantic. Furthermore, the magnitude of this cooling in the two cases is different (much colder in the case of 21 kaBP orbit), whereas the magnitude of the cooling along the coast of Antarctica is nearly identical. Therefore, considering the negligible effect of 21 kaBP orbital forcing relative to the present, this suggests that the cooling in the northern North Atlantic results from the combination of orbital and CO_2 forcing, while the cooling along the coast of Antarctica results solely from the CO_2 forcing. The cooling in SAT over the northern North Atlantic reflects similar cooling in summer SST (Figs. 4.5a–4.5d) and sea ice expansion in winter (Figs. 3.8a–3.8d and 4.6). These results are accompanied by a reduced meridional overturning as described in detail in Chapter 3 (Figs. 3.2 and 3.5a–3.5d), and the decreased poleward ocean heat transport in the North Atlantic (Fig. 4.7). Note that the greater sea ice cover in the Norwegian Sea during winter (Fig. 4.6) and the weaker Atlantic poleward ocean heat transport in the present-day simulation (Table 4.1), compared to observations, are due to the coarse resolution used in the OGCM.

The cooling in SAT in the two 200 ppmv CO_2 experiments is much more severe during winter than during summer (Figs. 4.8a–4.8d). This becomes important when the mass bal-

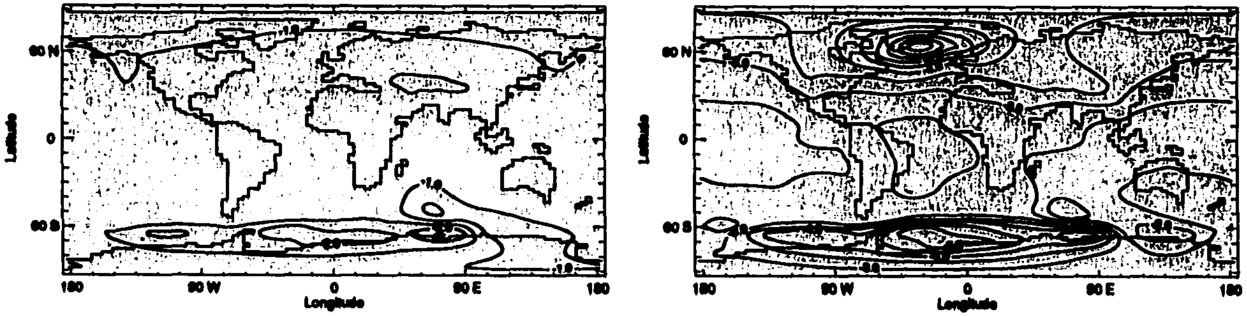

a 11 kaBP orbit and 280 ppmv CO_2 (A2 minus A1)

b 11 kaBP orbit and 200 ppmv CO_2 (A3 minus A1)

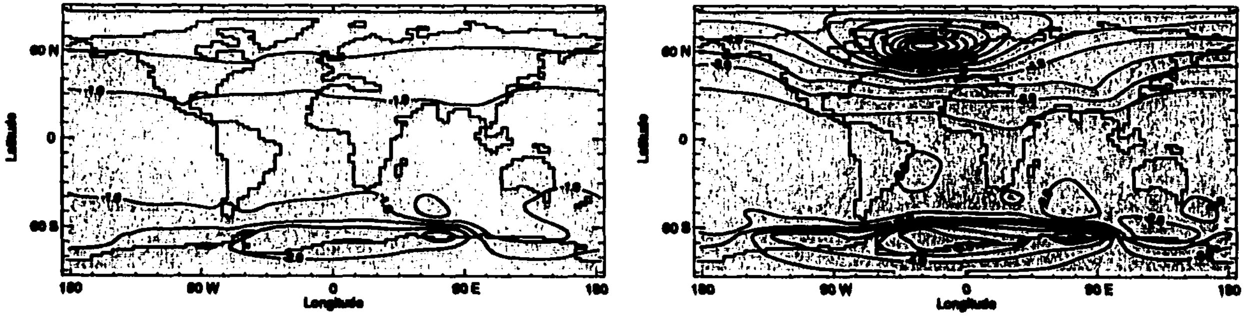

c 21 kaBP orbit and 280 ppmv CO_2 (A4 minus A1)

d 21 kaBP orbit and 200 ppmv CO_2 (A5 minus A1)

***Figure 4.4:* Simulated annual mean surface air temperature relative to the present-day control simulation. Contour interval is 0.5°C, and negative values are shaded.**

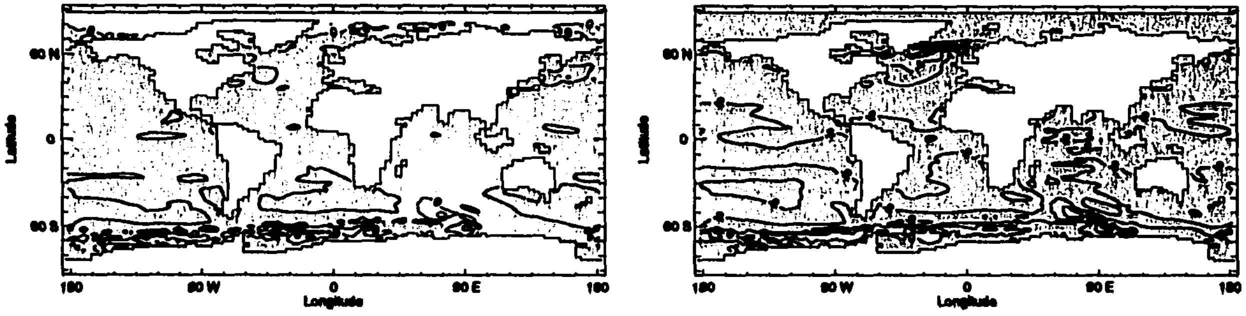

a 11 kaBP orbit and 280 ppmv CO$_2$ (A2 minus A1)

b 11 kaBP orbit and 200 ppmv CO$_2$ (A3 minus A1)

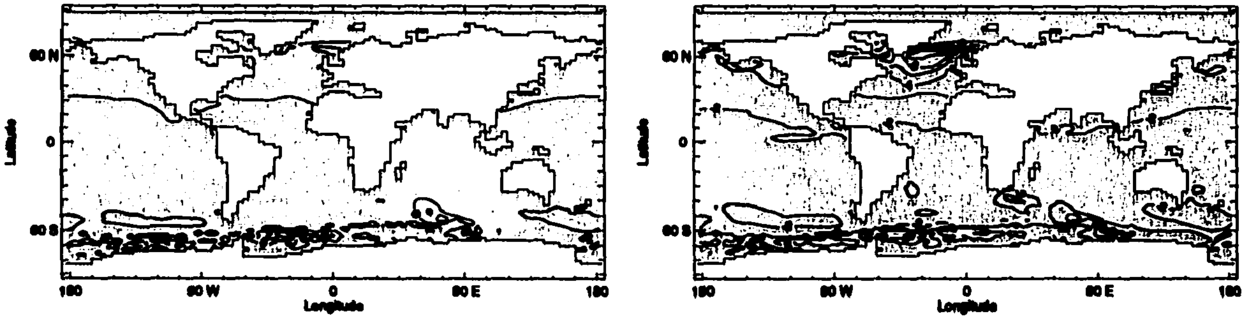

c 21 kaBP orbit and 280 ppmv CO$_2$ (A4 minus A1)

d 21 kaBP orbit and 200 ppmv CO$_2$ (A5 minus A1)

Figure 4.5: **Simulated sea surface temperature relative to the present-day control simulation during the NH summer. Contour interval is 1.0°C, and negative values are shaded. Here summer is defined as the period of 30 days following the summer solstice.**

Table 4.1: **Annual mean response of the climate model**

Experiments	Global SAT (°C)	Atlantic northward heat transport at 24.3°N (PW)
A1	14.0	0.767
A2	12.8	0.747
A3	11.1	0.570
A4	12.9	0.738
A5	11.2	0.480

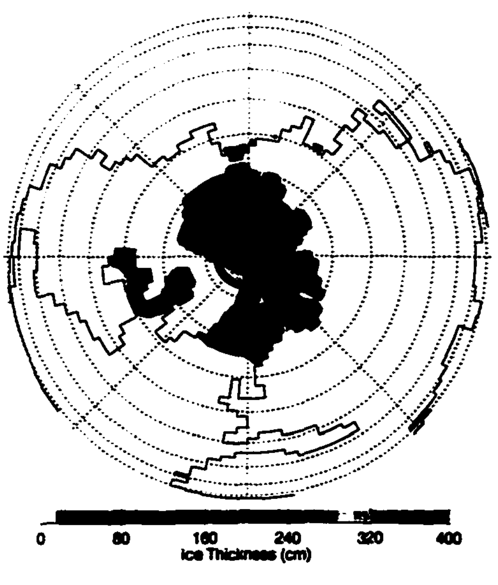

Figure 4.6: **Simulated present-day winter sea ice thickness. Here winter is defined as the period of 30 days following the winter solstice.**

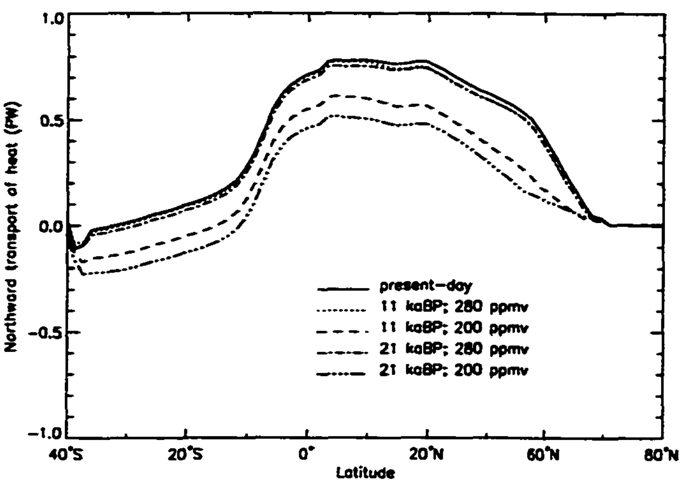

Figure 4.7: **Simulated annual mean northward heat transport in the Atlantic Ocean (1 PW ≡ 10^{15} W).**

ance for ice sheets is considered because summer temperatures are more critical according to the Milankovitch theory (Milankovitch 1941). Contrary to the cooling in SAT, the northward ocean heat transport relative to the present in the Atlantic is similar between summer and winter, or smaller during summer north of 30°N (Figs. 4.9a and 4.9b). Therefore, the cooling over the northern North Atlantic that is emphasised in winter is not attributed to changes in seasonal difference of ocean heat transport, and is attributed to the difference in sea ice cover through ice-albedo feedback and heat insulation from the warm ocean underneath. This interpretation is consistent with the difference in corresponding sea ice extent in Figs. 3.8a–3.8d and 4.6: the more the sea ice cover, the more the cooling.

In summary, the CO_2 forcing has a large impact on SAT, not uniformly or zonally over the globe, but concentrated near the North Atlantic. The effect of CO_2 increase, from 200 ppmv to 280 ppmv, on SAT is more pronounced in NH winter than in NH summer, associated with changes in sea ice extent in the northern North Atlantic. These changes are accompanied by an annual mean enhancement in the intensity of the meridional overturning and poleward ocean heat transport in the North Atlantic. In the NH summer, up to a 3–4.5°C warmer SAT due to orbital forcing (A3 minus A5) is found over the NH continents (Fig. 4.10a), whereas up to a 3.5°C warmer SAT due to CO_2 forcing (A4 minus A5) is found over the North Atlantic (Fig. 4.10b). The pronounced impact of orbital forcing on SAT over the land rather than over the ocean is also found in other studies (e.g., Short et al. 1991). In these results, the influence of large ice sheets, which existed in the past, are not included. This treatment enables one to extract the effect of orbital forcing between 21 kaBP and

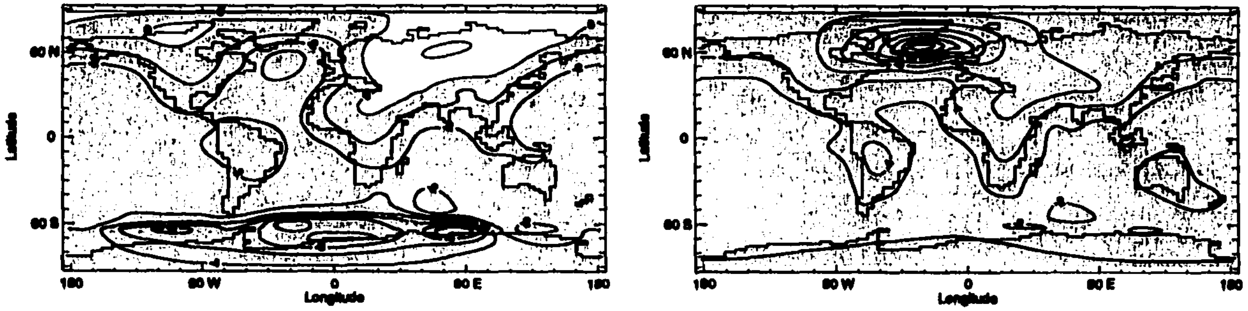

a 11 kaBP orbit and 200 ppmv CO₂ (A3 minus A1; NH summer

b 11 kaBP orbit and 200 ppmv CO₂ (A3 minus A1; NH winter

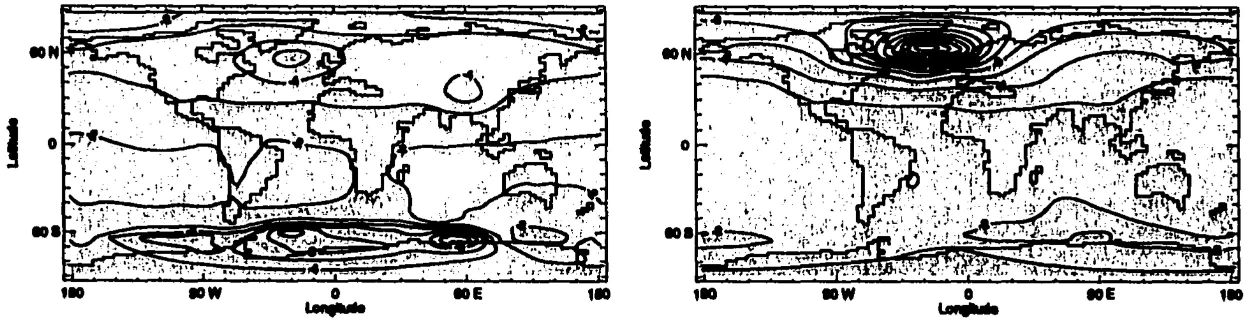

c 21 kaBP orbit and 200 ppmv CO₂ (A5 minus A1; NH summer)

d 21 kaBP orbit and 200 ppmv CO₂ (A5 minus A1; NH winter

Figure 4.8: **Simulated seasonal surface air temperature relative to the present-day control simulation. Contour interval is 1°C, and negative values are shaded. Here the definitions of summer and winter are the same as Figs. 4.5 and 4.6.**

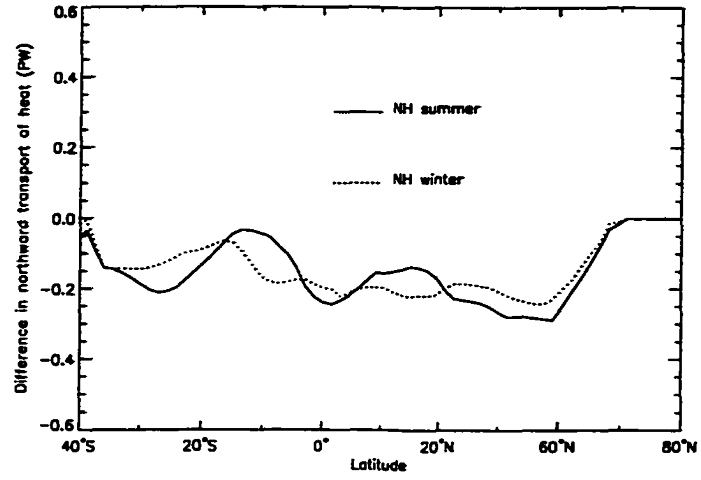

a 11 kaBP orbit and 200 ppmv CO_2 (A3)

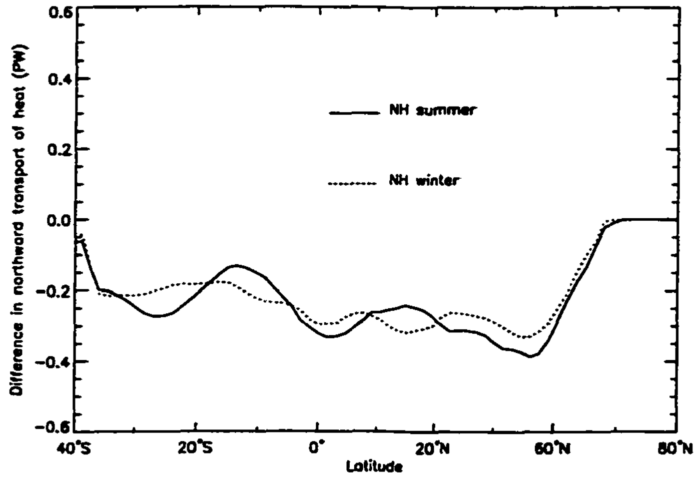

b 21 kaBP orbit and 200 ppmv CO_2 (A5)

Figure 4.9: **Simulated seasonal northward heat transport in the Atlantic Ocean relative to the present-day control simulation (1 PW $\equiv 10^{15}$ W). Here the definitions of summer and winter are the same as Figs. 4.5 and 4.6.**

11 kaBP alone, without being affected by the different size of the prescribed ice sheets at each of these times. However, it also introduces an uncertainty in the interpretation of the results in that the magnitude of the response might change under the influence of large ice sheets. Furthermore, although the effect of seasonal snow cover change on planetary albedo is included in the model (Eq. 2.7), the effect of potential cloud cover changes is not incorporated.

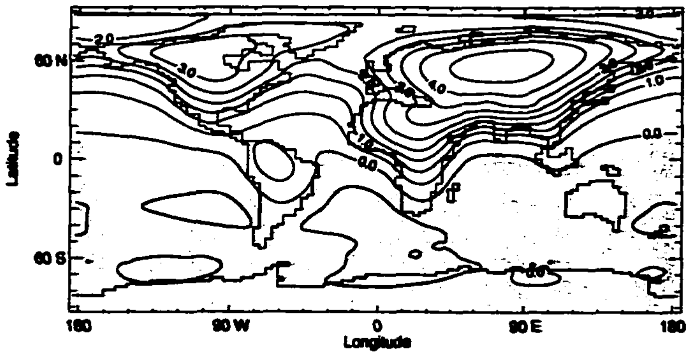

a Effect of orbital forcing (A3 minus A5)

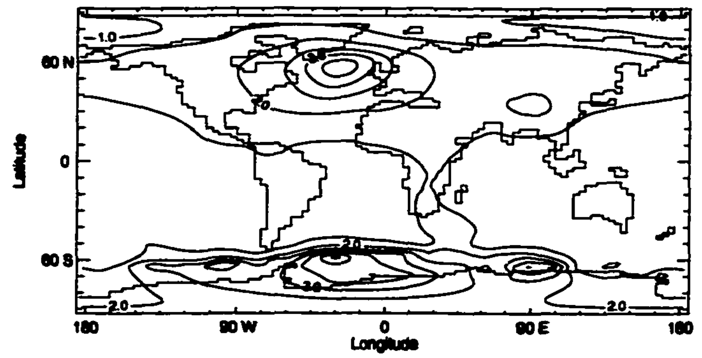

b Effect of CO_2 forcing (A4 minus A5)

Figure 4.10: **Simulated difference in surface air temperature during the NH summer. Contour interval is 0.5°C, and negative values are shaded. Here the definition of summer is the same as Fig. 4.5.**

Precipitation is another important factor for the mass balance of ice sheets. Accumulation is controlled by the amount of moisture available for precipitation and the fraction of snow in precipitation. Fig. 4.11a shows the difference in winter precipitation rate between 11 kaBP and 21 kaBP orbital forcing, when 200 ppmv CO_2 is imposed. Similarly, Fig.

4.11b shows the difference in winter precipitation rate between 280 ppmv and 200 ppmv CO_2 forcing, under the 21 kaBP orbital configuration. The change in orbital geometry, from 21 kaBP to 11 kaBP, leads to little increase in precipitation rate over the continents in high latitudes while it yields pronounced increase in the northern North Atlantic. The rise in atmospheric CO_2 concentration, from 200 ppmv to 280 ppmv, leads to an increase in precipitation rate over large areas of the NH, and again it yields a pronounced increase in the northern North Atlantic. This increase over large areas of the NH is caused by an enhanced hydrological cycle associated with CO_2-induced warming. CO_2 forcing introduced an increase in winter precipitation rate in North America and western Europe while orbital forcing has little effect there. On the other hand, a similar pattern of change in winter precipitation rate is seen in the North Atlantic: a decrease on the western and eastern sides in mid latitudes, and an increase in high latitudes.

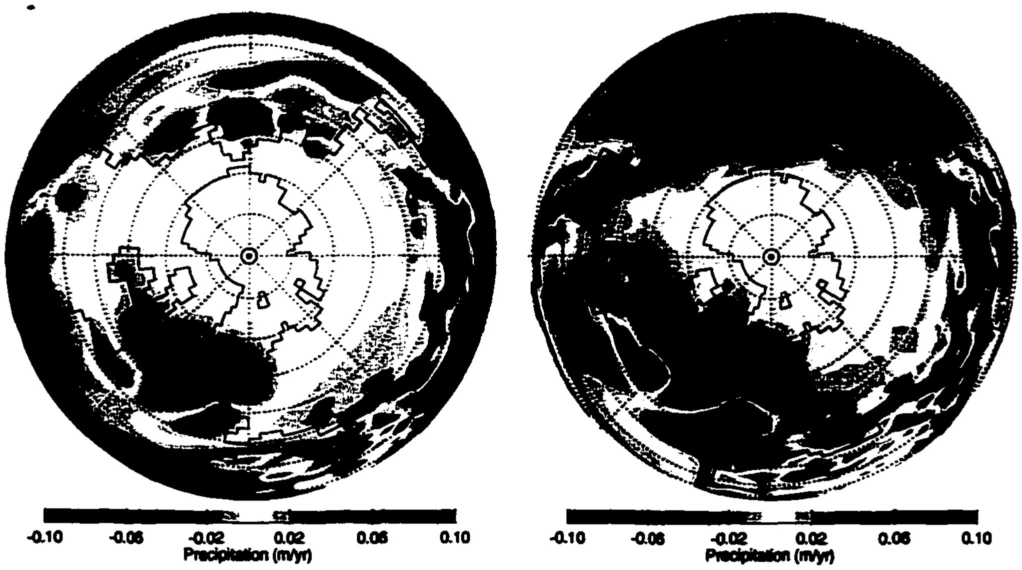

a Effect of orbital forcing (A3 minus A5) b Effect of CO_2 forcing (A4 minus A5)

Figure 4.11: **Difference in simulated winter precipitation rate. Here the definition of winter is the same as Fig. 4.6.**

The decreased precipitation rate in the mid-latitude North Atlantic reflects the decreased evaporation rate there. The warming in the northern North Atlantic, associated with changes in ocean heat transport, is relatively local in the ocean, but covers a relatively large area in the atmosphere through diffusion. It results in the large warming in the mid-latitude atmosphere and small warming in the mid-latitude ocean, reducing the vertical temperature gradient at the air-sea interface and hence reducing the evaporation rate. The increased precipitation rate in the high-latitude North Atlantic reflects an increased evaporation rate and moisture transport, which result from an increased gradient of horizontal temperature and hence specific humidity. The increased horizontal temperature gradient results, of course, from the warming in the northern North Atlantic. Note that the increase in the precipitation rate over the northern North Atlantic due to orbital forcing is much less under 280 ppmv CO_2 compared to under 200 ppmv CO_2 forcing, and the increase due to CO_2 forcing alone is slightly smaller under 11 kaBP orbital parameters compared to the 21 kaBP case. These results are consistent with oceanic responses.

Figure 4.12a shows the difference in annual mean snowfall rate between 11 kaBP and 21 kaBP orbital forcing, when 200 ppmv CO_2 is imposed. Similarly, Fig. 4.12b shows the difference in annual mean snowfall rate between 280 ppmv and 200 ppmv CO_2 forcing, under 21 kaBP orbital conditions. Consistent with the precipitation rate during winter, the change in orbital geometry, from 21 kaBP to 11 kaBP, brings negligible increase in snowfall over the continents in high latitudes. There is an appreciable increase in snowfall rate over the continents in mid latitudes, reflecting a longer snowfall season due to reduced insolation during fall (Figs. 4.3c and 4.3d). The rise in atmospheric CO_2 concentration, from 200 ppmv to 280 ppmv, brings little increase in snowfall rate over the continents in high latitudes, despite the increased precipitation rate during winter. There is also a large decrease in snowfall rate over the continents in mid latitudes, reflecting a shorter snowfall season due to CO_2-induced warming. Changes in the snowfall rate in the North Atlantic reflect changes in the sea ice cover rather than changes in the precipitation rate, as snow is allowed to accumulate in the model-ocean only where sea ice exists.

4.4.2 Ice-sheet response

In the model, glacial inception started under present-day forcing at the high bed elevation areas of Greenland and Antarctica, i.e., along the east coast of Greenland and the coast of East Antarctica. As expected from the small accumulation rate over Antarctica, it takes a much longer time to reach steady state for ice volume in the SH than the NH (Fig. 4.13). There is an important positive feedback in the model for the glacial expansion (decay) in terms of surface mass balance. As the elevation increases (decreases), SAT decreases (increases) through the specified lapse rate. Consequently, the fraction of snow in precipitation increases (decreases) and the melting rate of snow decreases (increases). Therefore, the absolute time taken to equilibrium is not independent of the frequency of the

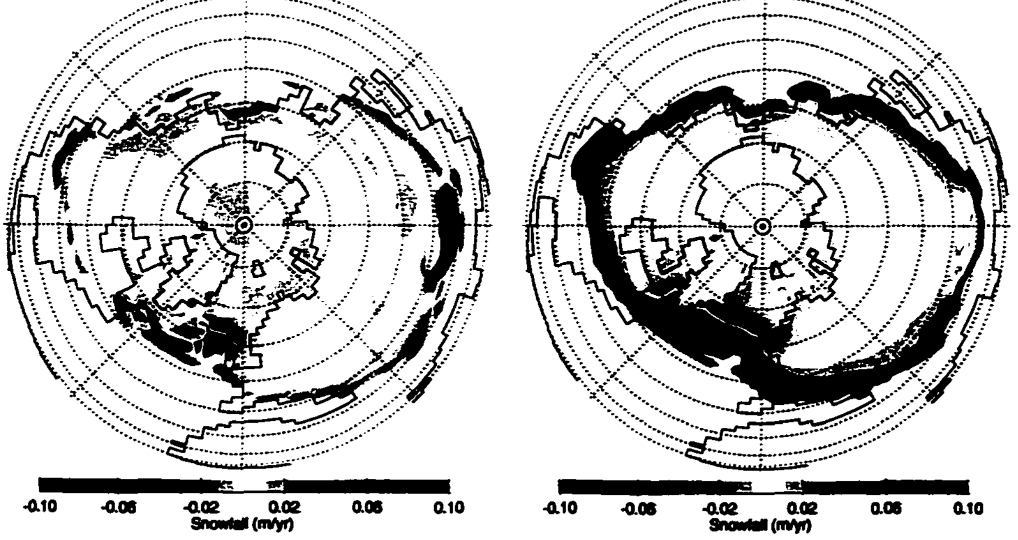

a Effect of orbital forcing (A3 minus A5) b Effect of CO_2 forcing (A4 minus A5)

Figure 4.12: **Difference in simulated annual mean snowfall rate.**

communication between the climate model and the ice sheet model although the equilibrium ice sheets are similar.

Figures 4.14a and 4.14c show the present-day equilibrium ice sheets, starting from no initial land ice, in the NH and the SH, respectively. For comparison, the observed ice sheet thicknesses over Greenland and Antarctica are also provided in Figs. 4.14b and 4.14d, respectively. The model successfully simulates the approximate ice sheet locations (only Greenland and Antarctica and nowhere else) and ice dome locations despite the coarse resolution of the ice sheet model. However, the model generally overestimates the ice thickness. For example, the simulated maximum ice thickness near the Greenland summit is 3867 m while the corresponding value calculated from observational measurements is 3050 m. Similarly, the maximum ice thickness near the Vostok (Antarctica) is 4753 m while that from observations is 4150 m. Although these maximum thickness values are tunable by changing the ice dynamics flow parameter, the same flow parameter is used in all experiments. The difference between the simulated ice thickness and the observations generally is a maximum near ice margins, due in large part to the resolution with which the model cannot properly represent the surface slope near the ice margins. As it is the increased slope near the margins that allows the thinner marginal ice to be mobile, the

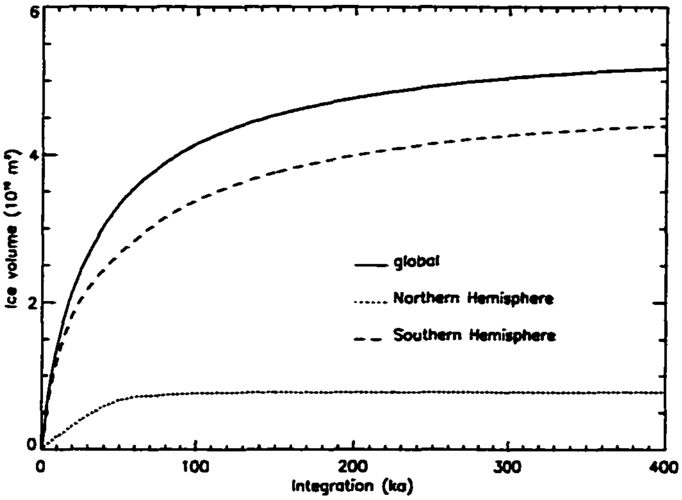

Figure 4.13: **Ice volume evolution (10^{16} m^3) under the present-day forcing in the coupled climate-ice sheet model.**

large cells force marginal ice to be thicker in order to build up sufficient marginal slope. The model also tends to overestimate glacial areas as thicker ice transports more ice toward the margins. It is expected that an ice sheet model with increased resolution would help resolve these problems (see next chapter).

Figures 4.16d and 4.16a show the response of ice sheets to 21 kaBP orbital and 200 ppmv CO_2 forcing (A5), and 11 kaBP orbital and 280 ppmv CO_2 forcing (A2), respectively, starting from the ICE-4G LGM reconstruction (Fig. 4.15 — Peltier 1994). Since these two experiments are conducted under perpetual forcing, neither of them should be expected to yield the actual 21 kaBP or 11 kaBP ice sheets. Rather, 21 kaBP ice sheets are expected to be much thicker and 11 kaBP ice sheets are expected to disappear as it is the time of maximum NH summer insolation during the last deglaciation. The clear difference in simulated ice-sheet distribution between the two different forcings supports the viability of the coupled climate-ice sheet model. At the same time, there are some limitations in the model performance: the model underestimates ice sheet expansion at 21 kaBP while the model probably overestimates it at 11 kaBP. This simulated tendency of less ice over eastern Canada and extra ice over western Canada may reflect the respective warmer and cooler climate bias in those areas in the present-day simulation.

Table 4.2 shows a comparison of the equilibrium climates simulated with and without the CIDM incorporated into the climate model. The 11 kaBP result with the CIDM corresponds to the climate after most of ice sheets have melted away (Fig. 4.16a). There is no significant

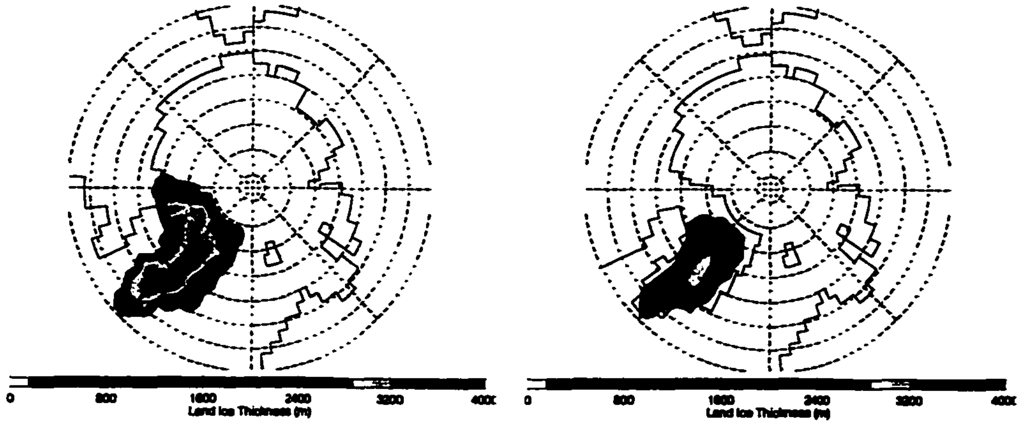

a Simulated Greenland ice sheet

b Observed Greenland ice sheet

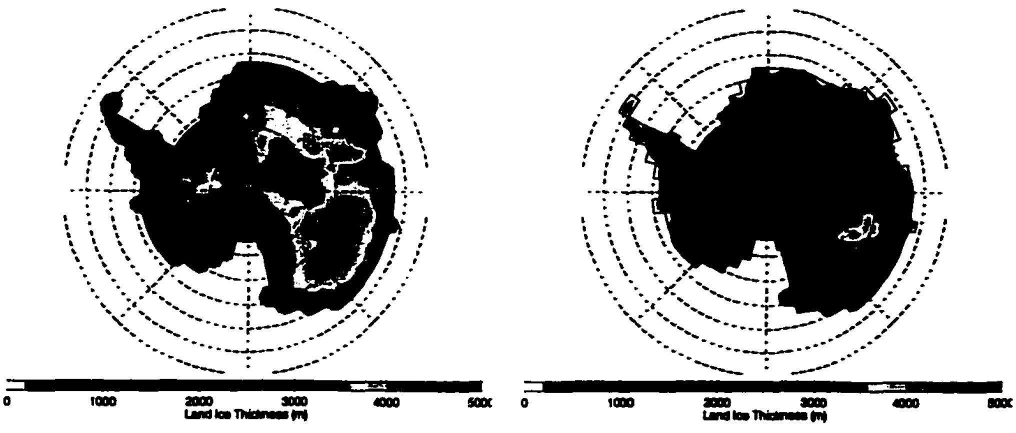

c Simulated Antarctic ice sheet

d Observed Antarctic ice sheet

Figure 4.14: **Present-day, simulation using the coupled climate-ice sheet model and observations.**

difference between the models, in both the present-day simulation and 11 kaBP experiment, showing the consistency between the models. Note that the 21 kaBP result is not included in this table as both models are not expected to show similar results: no ice sheet is prescribed in the climate model while large ice sheets exist in the coupled climate-ice sheet model. The present-day simulation, two paleo-experiment results, and this comparison suggest that the model works reasonably well and is expected to be useful for glaciation and deglaciation studies, albeit some future improvements are quite possible. These include an increase in resolution of the ice sheet model, the inclusion of atmospheric moisture advection (Weaver et al. 2001), as well as an improved present-day control climate.

Table 4.2: **Comparison between the climate model (model 1) and the coupled climate-ice sheet model (model 2)**

Global, annual	Present-day		11 kaBP; 280 ppmv	
mean fields	model 1	model 2	model 1	model 2
SAT (°C)	14.0	14.2	12.8	12.9
SST (°C)	18.3	18.5	17.4	17.6

Figures 4.16b and 4.16c show the response of ice sheets to 11 kaBP orbital and 200 ppmv CO_2 forcing (A3), and 21 kaBP orbital and 280 ppmv CO_2 forcing (A4), respectively, starting from the same initial ice sheets as in the previous experiments. Figures 4.16d-4.16b reveal the relative importance of orbital or CO_2 forcing on the maintenance or deglaciation of the LGM ice sheets. The impact of an increase in atmospheric CO_2 concentration, from 200 ppmv to 280 ppmv, during the last deglaciation is extracted by comparing Figs. 4.16d and 4.16c. Similarly, the impact of changes in orbital geometry, from 21 kaBP to 11 kaBP, during the last deglaciation is extracted by comparing Figs. 4.16b and 4.16d. These comparisons reveal that the influence of the orbital forcing is more important than that of CO_2 forcing during the last deglaciation. This relative importance of orbital forcing over CO_2 forcing reflects the dominant influence of orbital forcing on summer temperatures, whereas CO_2 forcing is dominant only for winter temperatures. Nevertheless, both orbital and CO_2 forcing are necessary for complete deglaciation. The comparison between Figs. 4.16d and 4.16c suggests that the effect of the increased winter precipitation rate due to increased CO_2 concentration is overcome by warmer temperatures. Similarly, the comparison between Figs. 4.16d and 4.16a suggests that the effect of increased annual snowfall rate in parts of North America due to changes in orbital geometry is also overwhelmed by the warmer summer temperatures.

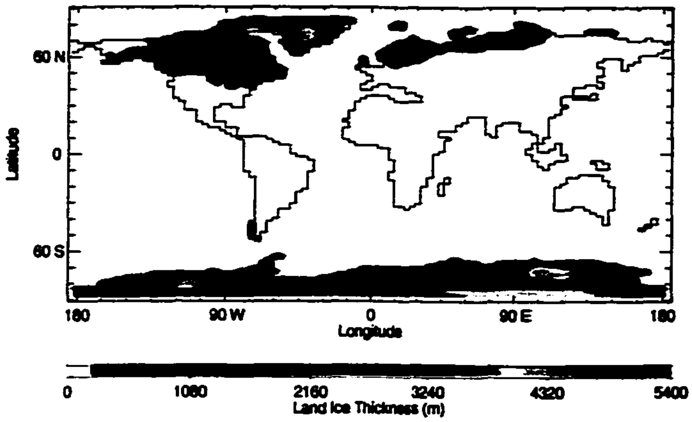

Figure 4.15: **Initial conditions used for the experiments.**

4.5 Discussion

According to the results in subsection 4.4.2, the difference in orbital geometry between 11 kaBP and 21 kaBP is more influential than the difference in atmospheric CO_2 concentration between 280 ppmv and 200 ppmv on the mass balance of ice sheets. There is little difference in orbital forcing between the present-day and 21 kaBP. In addition, the effect of the reduction in CO_2 concentration from 350 ppmv to 280 ppmv on the thermohaline circulation is smaller than the effect of a reduction from 280 ppmv to 200 ppmv (Chapter 3). Therefore, the difference in orbital geometry between the present-day and 11 kaBP would be more influential than the difference in atmospheric CO_2 concentration between 350 ppmv and 280 ppmv on the mass balance of ice sheets. While no ice grows over North America under present-day forcing (Fig. 4.14a), there is some ice left over western Canada under 11 kaBP orbital and 280 ppmv CO_2 forcing (Fig. 4.16a). The climate model shows no permanent snow cover over North America, including western Canada, under 11 kaBP orbital and 280 ppmv CO_2 forcing when the integration is started from present-day ice sheets. Therefore, this apparent discrepancy known as the "small ice sheet instability" (e.g., Weertman 1961; Birchfield 1977; Morales Maqueda et al. 1998), is attributed to the different initial conditions used in the two experiments. That is, no initial ice is specified for the present-day simulation while LGM ice sheets are specified for the experiment under 11 kaBP orbital and 280 ppmv CO_2 forcing.

It is interesting that glacial inception and the subsequent growth of ice sheets started from the bed elevation over Greenland and Antarctica under present-day forcing, as both ice sheets were possibly built up when climates were much colder than today. While validation

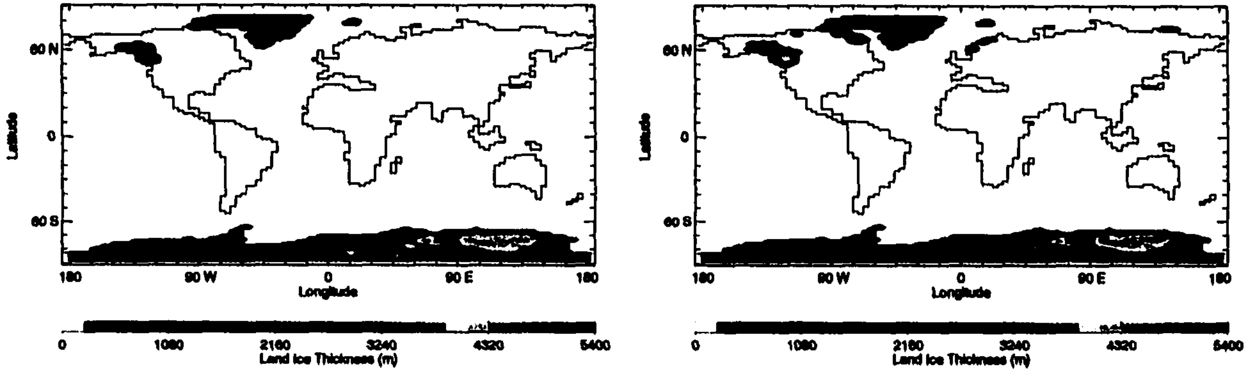

a 11 kaBP orbit and 280 ppmv CO_2 (A2)

b 11 kaBP orbit and 200 ppmv CO_2 (A3)

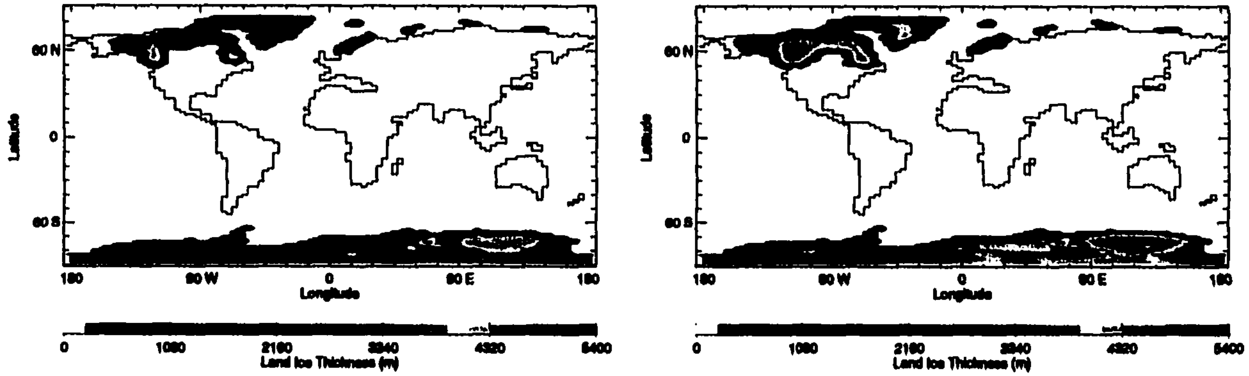

c 21 kaBP orbit and 280 ppmv CO_2 (A4)

d 21 kaBP orbit and 200 ppmv CO_2 (A5)

Figure 4.16: **Ice sheet response of the coupled climate-ice sheet model to changes in radiative forcing.**

of any model against present-day observation is necessary, it is not sufficient to give one confidence in climate simulations under different forcing. Such a universality is one of the largest uncertainties in applications of models for future climate prediction. At the same time, it is one of the most important applications of paleoclimate modelling. It is generally difficult to compare simulated results directly to the continental paleoclimate proxy records because of the difference in scales between the *areally-averaged* numerical grid and *in situ* data sampling. For instance, when the areally-averaged elevation in the model underestimates local elevation, it is not straightforward to evaluate air temperature in the surface layer or along the surface slope using the simulated lapse rate in the free atmosphere. Simulating the ice sheet mass balance gives another way of testing a climate model due to its large horizontal scale even though it is also affected by local topography and geology. In this regard, the model successfully showed a reasonable difference in sensitivity between 21 kaBP orbital and 200 ppmv CO_2 forcing, and 11 kaBP orbital and 280 ppmv CO_2 forcing. It is not, however, impossible that the model succeeded for wrong reasons, and several uncertainties are discussed below.

Although the original version of the CIDM contained ice thermodynamics (Marshall and Clarke 1997a;b), it was not used in this study because the ice temperature to be specified as an initial condition for the LGM was not known. It would be useful if the model could be integrated for a long period so that, by the time the LGM was reached, the memory of the initial ice temperature no longer remained. Since there exist large uncertainties in the physics of ice rheology including the enhancement factor in the flow law (Peltier 1998 and Hooke 1998, p.27-45), the ice temperature was treated as one of the adjustable parameters affecting the flow rate of ice in order to obtain a realistic simulation of the LGM ice sheets. As a result, a relatively cold value of -15°C was used. The fact that eastern Canada was too warm in the present-day control climate, might be responsible for the difficulty in maintaining the LGM ice sheets. The cold ice temperature, together with the use of coarse resolution, in the model might underestimate the flow rate and hence the role of ice dynamics during the last deglaciation.

As discussed in section 3.4, some feedback mechanisms associated with atmospheric dynamics could not be examined. The diffusive atmosphere used in this study may overestimate the effect of changes in the climate of northern North Atlantic on the Laurentide ice sheet and underestimate it on the Fennoscandian ice sheet as they are located in the upwind and downwind directions, respectively (Rind et al. 1986; Manabe and Stouffer 1988). Manabe and Broccoli (1985) and Broccoli and Manabe (1987) pointed out that the enhanced northerly flow over eastern sections of the Laurentide ice sheet likely aids in the cooling of its southeastern margin. In addition, the formation of storm tracks, and their associated precipitation belt, due to enhanced baroclinicity at the southern margin of Laurentide and Fennoscandian ice sheets may be an important positive feedback for the mass balance of ice sheets. Similar conclusions were made more recently by Hall et al. (1996), specifying CLIMAP ice sheets (CLIMAP 1981), and Vettoretti et al. (2000), specifying ICE-4G LGM ice sheets. Even with atmospheric dynamics, however, Thompson and Pollard (1997) could not maintain the ICE-4G LGM ice sheets under LGM forcing, leading them to speculate that a CLIMAP-like thicker Laurentide ice sheet existed prior to 21 kaBP, and that growth of the Cordilleran ice sheet occurred after 21 kaBP, so that it reduces the rain shadow effect on the precipitation over the Laurentide ice sheet.

The ICE-4G reconstruction of LGM ice sheets used as initial conditions is not ideal for the study of ice sheet mass balance. For example, it does not provide a realistically smooth ice sheet surface. The reason is that it is obtained from inverse modelling through setting ice blocks in the glacio-geologically constrained area to reproduce observed postglacial relative sea level change. Marshall (1996) integrated for 8000 years with zero surface mass balance to remove the unrealistic structure of the ice sheet prior to his experiments. The same procedure was tested in this study, but the conclusions of this chapter remain unaffected. The uncertainties in the ICE-4G reconstruction arise from the assumptions that the ice sheets were in isostatic equilibrium at the LGM, the mantle viscosity is a function of radius only, and the relative sea level record could be analysed without making the usual correction for a presumed constant local rate of tectonic uplift (Peltier 1994; Edwards and Peltier 1995; Peltier 1996; Thompson and Pollard 1997; Peltier 1998). On the other hand, uncertainties in the CLIMAP reconstruction arise from neglecting of the deformation of beds and a marine-based ice-sheet, and most importantly, the assumption that the ice sheet is in dynamic equilibrium at the LGM. Despite these serious uncertainties, the ICE-4G reconstruction is preferred to the CLIMAP (1981) reconstruction, as it arises from a time-dependent model and as the results are constrained by a large number of observed post-glacial relative sea level records.

During the course of these experiments, the effect of tropospheric aerosol forcing and cloud feedback was neglected. Both effects could be important (Hansen et al. 1984; Harvey 1988; Anderson and Charlson 1990; Overpeck et al. 1996) although the quantification of these effects is difficult. Furthermore, the sea level drop of ~120 m at the LGM was not taken into account for the simplicity of the comparison with the present-day control simulation and 11 kaBP experiments.

As mentioned in section 3.4, the thermohaline circulation could be affected by the mechanisms that are not included in this model, such as meltwater and river re-routing, changes in ice calving rate, and transport and melting of icebergs. The variations of the thermohaline circulation, in turn, could affect the ice sheet mass balance as shown in this chapter. Although it is likely that such an interaction between ice sheets and the ocean occurred in the past on millennial time scales (e.g., Bond et al. 1993; Broecker et al. 1989; Alley et al. 1999; Clarke et al. 1999; Licciarde et al. 1999) the significance of it on orbital time scales is not well established.

In this study, all experiments were conducted under perpetual forcing due to the prohibitive computational cost of transient simulations. Therefore, only the equilibrium states were examined. In reality, however, glacial termination is characterized by highly transient sates with rapid climatic changes. Investigating the equilibrium states provides a first look at the problem and addresses the tendency of the climatic response to the external forcing. From the viewpoint of testing the model performance, it is also an necessary research step. However, limitations still exist in our ability to address the actual transient response.

It is tempting to apply the results of this study to other previous deglaciations because of the semi-regularity of glacial-interglacial cycles. Before such a generalisation can be made, however, the sequence of events has to be firmly established. For instance, the relative timing of changes in ice volume and CO_2 concentration for the penultimate deglaciation is well established, as mentioned in section 4.1. On the other hand, the absolute timing of the penultimate deglaciation and hence the relative timing of changes in insolation and ice volume is highly controversial (summarised in Cronin 1999, 159-163,185-189 and more recently in Henderson and Slowey 2000). Therefore, the application of the results obtained in this study is restricted to the last deglaciation and speculation regarding other previous deglaciations should be avoided.

4.6 Conclusion

It has been established that increases of atmospheric CO_2 concentration during the last deglaciation preceded the changes in global ice volume, suggesting the important role of CO_2 forcing in deglacial processes. To study the relative importance of orbital and CO_2 forcing in ice sheet mass balance, the ice sheet model was globally and asynchronously coupled to a coupled atmosphere-ocean-sea ice model. The model performed reasonably well under present-day forcing, and showed a clear difference in ice sheet distribution under 11 kaBP and 21 kaBP perpetual forcing, providing some confidence in the validity of the model.

Both orbital and CO_2 forcing have an impact on ice sheet maintenance and deglacial processes. Although neither acting alone is sufficient to lead to complete deglaciation, orbital forcing appears to be more important during the last deglaciation. The effect of increased CO_2, from 200 ppmv to 280 ppmv, on SAT has its peak in winter associated with changes in sea ice extent in the northern North Atlantic. These changes are accompanied by an annual mean enhancement in the intensity of the meridional overturning and poleward ocean heat transport in the North Atlantic. On the other hand, the effect of orbital forcing, from 21 kaBP to 11 kaBP, has its peak in summer. Since summer temperatures, rather than winter temperatures, are found to be dominant for the ice sheet mass balance, orbital forcing has a larger effect than CO_2 forcing in deglaciation. The effect of changes in winter precipitation rate and annual snowfall rate are overwhelmed by the temperature effect.

Within the framework of equlibrium model experiments and evidence from proxy records, the results of this chapter suggest that the last deglaciation was initiated through increasing summer insolation and accelerated by a subsequent increase in the atmospheric CO_2 concentration. How the orbital trigger leads to increasing CO_2 and complete deglaciation is, of course, an outstanding challenge in paleoclimatology.

Chapter 5

Glacial inception: Effect of subgrid topography

5.1 Introduction

One of the fundamental and challenging issues in paleoclimate modelling is the failure to capture the last glacial inception (Rind et al. 1989). Between 118 and 110 kaBP, the sea level records show a rapid drop of 50–80 m from the last interglacial, which itself had a sea level only 3–5 m higher than today (East et al. 1999; Cuffey and Marshall 2000). This sea level lowering, as a reference, is about half of the LGM difference of 120 m relative to the present (Fairbanks 1989). Geological evidence suggests that the Laurentide ice sheet initially started on plateaus in the Canadian Arctic, Quebec/Labrador, and Keewatin around 115 kaBP, and then expanded toward the west (Clark et al. 1993). Geological and palynological evidence suggests that the Fennoscandian ice sheet started on mountains in Scandinavia (Ives et al. 1975; Kukla 1980). Geological evidence also shows no significant ice sheets over Alaska and western Canada (Clark et al. 1993). The potential existence of large ice sheets over Siberia (Andrews 1982; Denton and Hughes 1981; Flint 1971; Verbitsky and Oglesby 1992; Dong and Valdes 1995) and Tibet and the Himalayas (Kuhle 1987b;a; 1988; Zhang 1989) are controversial.

The fundamental aspect of the glacial inception simulation is the occurrence of permanent snow cover. The failure to capture the last glacial inception is not a unique problem of one particular model, but rather it is common of most models. The coupled atmosphere-ocean-sea ice model, used in Chapter 3 and 4, is no exception. The existence of a possible missing forcing has been explored. No evidence supports changes in solar radiation or tropospheric aerosol loading during the glacial inception period as the reason for the inability of models to capture glacial inception. In addition, there is no firm evidence to suggest any relationship between volcanic eruptions and the glacial inception (Rind et al. 1989). The effect of radiative forcing associated with greenhouse gases has already been examined in many studies (Table 6.1). Nevertheless, there are few AGCMs that "succeeded" in simulating the last glacial inception (Dong and Valdes 1995; Gallimore and Kutzbach 1996). Gallimore and Kutzbach (1996) implicated an important role for vegetation feedbacks in their successful simulation — a feedback that will be revisited in Chapter 6 in association with changes in ocean surface conditions. Although not conclusive, Dong and Valdes (1995) related their success to the use of a high resolution model. In low resolution models, topography is smoothed and small high-elevation areas are represented as a large mean-elevation area. They argued that this prohibits glacial inception from originating at high-elevation areas of small areal extent. In addition, snow disappears uniformly in a grid cell instead of gradually melting from the south to the north. The subsequent albedo feedback also results in an instant northward diffusion of heat within a particular grid cell.

Marshall and Clarke (1999) elegantly demonstrated the profound impact of subgrid-scale flow of ice on glacial inception. They parameterised the mass balance associated with subgrid-scale processes in their dynamic ice sheet model. Each grid cell was discretized into subgrid elevation levels with subgrid areas, and the distribution of precipitation on each level, as well as the transport of ice from higher levels to lower levels, were both parameterised. As a result, in addition to the better representation of the present-day ice distribution in North America, large Laurentide ice sheet inception was observed under prescribed temperature and precipitation forcing. Their prescribed climate perturbation (doubled precipitation rate and a temperature drop of up to -14°C), however, needs to be explicitly calculated in a climate model to further validate the importance of the resolution of subgrid scale topography for capturing glacial inception.

Here, two approaches are taken using a coupled climate model to examine the importance of subgrid-scale topography in simulations of the last glacial inception. Each approach emphasises a different aspect of the role of subgrid-scale topography. The first approach allows for the mechanism that perennial snow cover starts on subgrid-scale high elevation areas, followed by local cooling through the albedo feedback, and subsequent cooling of the surrounding low elevation areas that causes perennial snow cover there. The second approach also includes the effect of the subgrid-scale flow of ice. Changes in albedo due to the presence or absence of snow and ice are treated at the subgrid scale in both approaches, allowing for the slow diffusion, rather than instant diffusion, of heat within a grid cell.

5.2 Subgrid treatment and experimental design

The time period of interest in this study is centred around 116 kaBP when the NH summer insolation had a minimum value during the last glacial cycle. The orbital configuration at

116 kaBP is characterised by both a smaller obliquity and a larger eccentricity than today (Table 5.1). The small obliquity reduces seasonality, i.e., less insolation at high latitudes in both hemispheres during their respective summers. The large eccentricity decreases the distance between the sun and the perihelion, while it increases the distance between the sun and the aphelion, i.e., less insolation in the NH summer while more insolation in the NH winter. The resulting distribution of insolation, relative to the present, shows a strong negative anomaly during the NH summer, with its peak in the NH high latitudes, and a strong positive anomaly during the NH winter, with its peak in low latitudes (Fig. 5.1a,5.1b). As the lowest probable "equivalent CO_2 level" (combined radiative forcing of CO_2 and CH_4 — Schlesinger and Verbitsky 1996) at 116 kaBP, a fixed CO_2 concentration of 240 ppmv was used for all experiments except the present-day simulations in which 350 ppmv was used. The radiative forcing at the top of the atmosphere due to the reduction of CO_2 by 90 ppmv is -2.2 W m^{-2} in the coupled climate model.

The coupled atmosphere-ocean-sea ice climate model was integrated under two different sets of orbital and CO_2 forcing: present-day and 116 kaBP (B1 and B2 in Table 5.1). The same initial conditions described in section 3.2 were applied at the beginning of both spin-ups. The climate model was integrated for 2000 years by which time a quasi-steady state was reached. The 2000-year spin-ups under present-day and 116 kaBP forcing without any subgrid treatment were then used as initial conditions in the following experiments. Note that simulated SST and sea ice fields from these two spin-ups are also used in the next chapter as prescribed lower boundary conditions of the AGCM, and are described there (subsection 6.3.1) to facilitate the understanding of the subsequent subsections.

Table 5.1: **Experiments using the coupled climate model (PD: present-day)**

Experiments	Ages	Perihelion (°)	Obliquity (°)	Eccentricity	CO_2 (ppmv)
B1	PD	283.0	23.44	0.01668	350
B2	116 kaBP	275.1	22.48	0.04122	240

Perihelion: longitude of perihelion relative to the moving vernal equinox

In the first approach, each cell in the model was divided into many subcells which have different surface elevations. The SAT in each subcell was diagnosed from the sea level air temperature for each cell, using a constant lapse rate of 6.5°C km^{-1}. SAT was used in calculating the longwave radiation, areal fraction of snow, the saturation specific humidity,

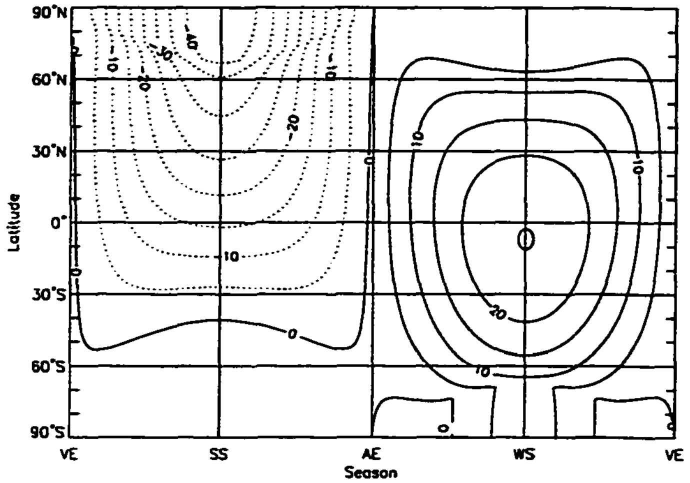

a With respect to season

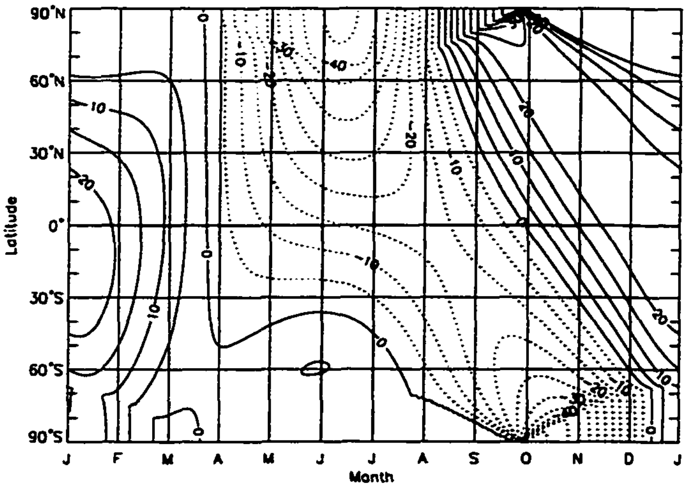

b With respect to calendar date

Figure 5.1: **Insolation at the top of the atmosphere at 116 kaBP relative to the present (W m^{-2}). Contour interval is 5 W m^{-2}, and negative values are dotted. VE, SS, AE, WS are respectively vernal equinox, summer solstice, autumnal equinox, and winter solstice in the NH.**

and the snow melting rate, and in determining whether precipitation falls as snow or rain. To perform a systematic analysis, five different subgrid resolutions were employed, ranging from 3.6°×1.8° to 0.2°×0.1° in longitude × latitude (M1–M5 in Table 5.2). As examples, the subgrid topography from the lowest resolution and the highest resolution cases are displayed in Figs. 5.2**a** and 5.2**b**, respectively. Note that these topographies were obtained from a data base of 5-min by 5-min global land and sea-floor elevations (ETOPO5 1988), using a raised-cosine weighted average.

Table 5.2: Resolution of the subcell

Experiment	M1	M2	M3	M4	M5
Resolution	3.6°×1.8°	1.2°×0.6°	0.6°×0.3°	0.4°×0.2°	0.2°×0.1°

The subgrid treatment of topography was only applied to the North American (and part of Greenland) grids (between 172.8°W and 50.4°W and between 37.8°N and 84.6°N), due to the limited amount of available computer memory, leaving the rest of the globe with the original resolution, i.e., 3.6°×1.8°. Note that in certain versions of the model, such as those used in Chapters 3 and 4, and Weaver et al. (2001), the topography at 3.6°×1.8° resolution was further smoothed by averaging with neighbouring grid elevations. This smoothing was still applied to the non-North American grids in this study for consistency. When applied to the North American grid in the case of 3.6°×1.8° resolution, it is confirmed to be responsible for the non-glaciation of Baffin Island under 116 kaBP forcing. The sensitivity to such an artificial and unphysical smoothing, however, is not the objective of this study and is not discussed further.

The integrations were carried out under both present-day and 116 kaBP forcing (C1 and C2 in Table 5.3). In addition, to diagnose the "errors" in capturing the last glacial inception with this particular model, the following experiments were conducted for each subgrid resolution. Under 116 kaBP orbital and CO_2 forcing, the threshold temperature, above which precipitation is assumed to fall as rain and below which it is assumed to fall as snow, was varied from -2.5 or 0°C (C3 or C4, respectively, in Table 5.3). Similarly, under 116 kaBP forcing, the precipitation rate was artificially doubled or quadrupled (C5 or C6, respectively, in Table 5.3). Note that runoff originating from snow melting was halved or quartered to conserve the total amount of moisture in the system.

These experiments will lead to a rough idea as to how much more cooling or precipitation is required for the occurrence of perennial snow cover. More importantly, they will reveal which factor (cooling and precipitation) is missing, as well as the geographic sensitivity

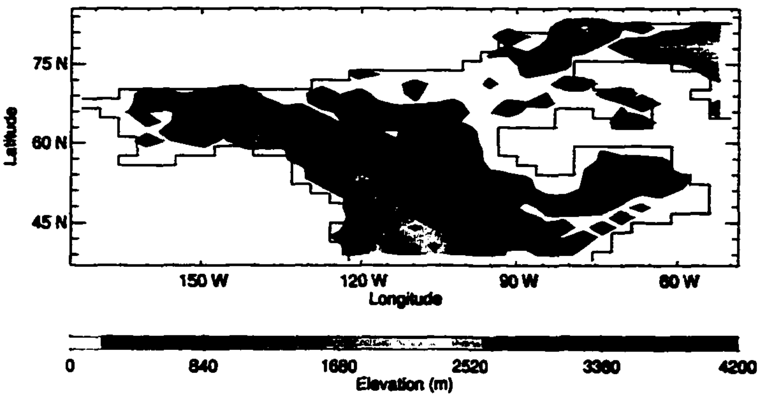

a The lowest subgrid resolution (3.6° x1.8°)

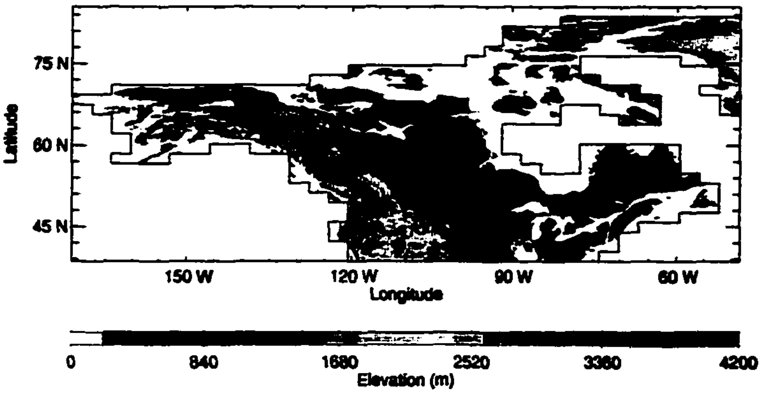

b The highest subgrid resolution (0.2° x0.1°)

Figure 5.2: **Subgrid topography over North America.**

Table 5.3: **Experimental design for the study of subgrid elevation (PD: Present-day)**

Experiments	Orbital geometry	Atmospheric CO_2 concentration (ppmv)	Critical temperature for snow (°C)	Multiplication factor for precipitation
C1	PD	350	-5.0	1
C2	116 kaBP	240	-5.0	1
C3	116 kaBP	240	-2.5	1
C4	116 kaBP	240	0.0	1
C5	116 kaBP	240	-5.0	2
C6	116 kaBP	240	-5.0	4

to glacial inception. As a result, 30 integrations were performed (M1–M5, C1–C6) taking advantage of the relatively short integration period necessary. The model was integrated for 20 years with specified subgrid resolution and forcing. The averaged fields over the last 10 years were utilised for this analysis.

In the second approach, the cell was discretized into subgrid elevation levels with subgrid areas. The subgrid elevation, h_k^b, is determined by

$$h_k^b = h_{\min} + \Delta h(k - 1/2), \quad k \in (1, n) \tag{5.1}$$

with

$$\Delta h = \left(h_{\max} - h_{\min}\right)/n \tag{5.2}$$

where $h_{\max}$ and $h_{\min}$ are maximum and minimum elevation in the grid cell, and n is the number of subgrid elevation levels. Areas belonging to each elevation level (interval: $h_k^b \pm \Delta h/2$) were directly constructed from a data base of 30-sec by 30-sec land elevation (GLOBE1.0 2001), rather than parameterising them through mathematical functions involving mean, variance, maximum, and minimum elevations (Walland and Simmonds 1996; Marshall and Clarke 1999). Sixteen subgrid elevation levels were employed. Note that Marshall and Clarke (1999) observed little effect in increasing the number of levels beyond eight. As examples, the distribution of the normalised areal fraction in the two grid cells containing Wisconsin and Idaho are shown in Figs. 5.3a and 5.3b, respectively. Visually, the distribution of areal fraction with respect to elevation is reasonably represented with 16 subgrid elevation levels. These subgrid treatments were applied globally.

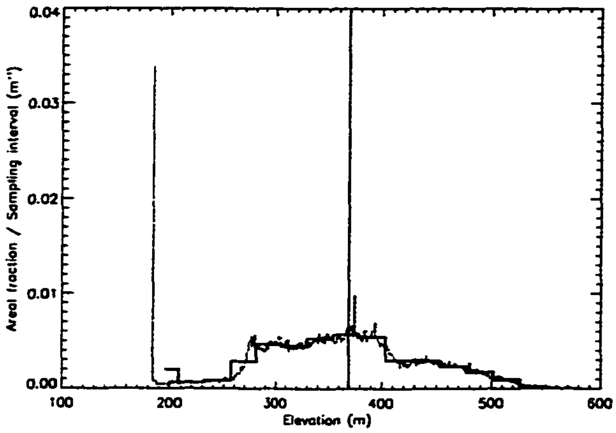

a A grid in Wisconsin (90–93.6°W and 45.0–46.8°N)

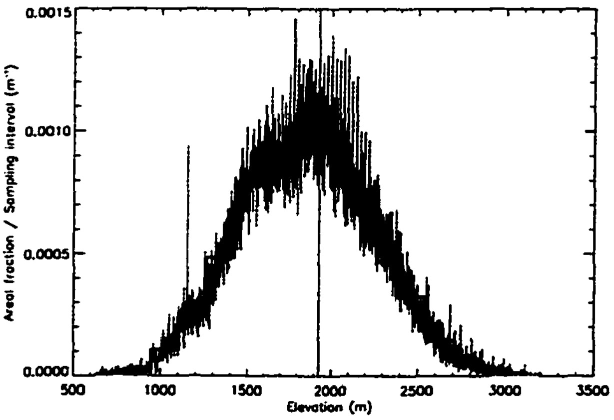

b A grid in Idaho (111.6–115.2°W and 45.0–46.8°N)

Figure 5.3: **Distribution of normalised areal fraction with respect to elevation. Histogram in blue represents normalised areal fraction sampled at each meter while that in red represents normalised areal fraction sampled at each subgrid elevation level. Black line represents elevation without any subgrid treatment.**

The downslope transport of ice is parameterised following Marshall and Clarke (1999). The mass balance at subgrid level k is parameterised as

$$\begin{aligned} \frac{\partial H_k}{\partial t} &= \frac{a_{k+1}}{a_k} Q_{k+1} - Q_k + b_k, \quad k \in (1, n-1), \\ &= -Q_k + b_k, \quad k = n. \end{aligned} \tag{5.3}$$

where H_k, a_k, and b_k are ice thickness, subgrid area, and surface mass balance at subgird level k, respectively, and Q_k is the volume flux per unit area of ice transferred from subgrid level k to level $k-1$. Ice is allowed to flow downslope only one subgrid level during a particular time step, and the volume flux is parameterised as

$$Q_k = \frac{1}{\tau}(H_k + b_k \Delta t)\left\{1 - \exp\left[-\left(\frac{\Delta h_k}{L_k}\right)^3\right]\right\}, \tag{5.4}$$

where $\tau = 10$ years is a time scale for the volume flux response, and $\Delta h_k = h_k - h_{k-1}$ with h_k being the surface elevation at subgrid level k. L_k represents the horizontal length scale at subgrid level k, which is parameterised as $L_k = L_0 a_k / A$ with L_0 and A being a horizontal length scale (approximated as longitudinal length) and area for a cell, respectively. As mentioned in section 5.1, the distribution of precipitation to each subgrid level is parameterised as a function of subgrid elevation in Marshall and Clarke (1999). However, this is not employed here as the focus is on the role of subgrid ice-flow in glacial inception. The mechanism tested in this study, namely that subgrid ice-flow from high to low elevations leads to the glacial inception, the distribution of less precipitation in high elevation areas and more precipitation in low elevation areas is not expected to aid the inception. In contrast to the first approach, only two integrations are conducted because these include ice-flow and hence require a longer integration period — 2000 years (Table 5.4).

Table 5.4: **Experimental design for the study of subgrid ice-flow (PD: Present-day)**

Experiments	Orbital geometry	Atmospheric CO$_2$ concentration (ppmv)	Number of levels
D1	PD	350	16
D2	116 kaBP	240	16

5.3 Results

5.3.1 The effect of subgrid elevation

The annual mean snowfall, snow melting, and net accumulation in North America (and part of Greenland) are summarised in Table 5.5, 5.6, and 5.7, respectively. Under 116 kaBP forcing (C2), the annual mean snowfall rates increase due to the longer snowfall season in all subgrid resolution experiments (M1–M5), when compared to the present-day simulations (C1). Despite the cooler summer at 116 kaBP, the annual mean snow melting also increases. This is simply because more snow is available to melt due to increased snowfall rate. As the increase in snowfall rate is larger than the increase in snow melting rate, in C2 compared to C1, the net accumulation increases. Therefore, 116 kaBP still provides more favourable conditions than the present-day for the occurrence of perennial snow cover even though the total amount of snow melting increases.

Table 5.5: Snowfall rate (10^{-3} m yr^{-1})

Experiments	M1	M2	M3	M4	M5
C1	3.66	3.71	3.74	3.73	3.74
C2	4.03	4.16	4.19	4.18	4.19
C3	5.35	5.47	5.51	5.51	5.51
C4	6.88	6.96	7.02	7.01	7.02
C5	8.09	8,36	8.42	8.41	8.43
C6	16.3	16.8	16.9	16.9	16.9

Table 5.6: Snow melting rate (10^{-3} m yr^{-1})

Experiments	M1	M2	M3	M4	M5
C1	3.42	3.45	3.49	3.49	3.50
C2	3.70	3.83	3.86	3.85	3.86
C3	4.61	4.78	4.80	4.79	4.80
C4	5.33	5.45	5.46	5.45	5.46
C5	7.30	7.59	7.63	7.60	7.62
C6	13.8	14.5	14.5	14.5	14.5

The geographical distribution of net accumulation in the present-day simulation with the lowest and the highest subgrid resolutions are displayed in Figs. 5.4a and 5.5a, respec-

Table 5.7: **Net accumulation rate (10^{-4} m yr^{-1})**

Experiments	M1	M2	M3	M4	M5
C1	2.39	2.52	2.47	2.43	2.45
C2	3.26	3.26	3.28	3.34	3.33
C3	7.42	6.87	7.05	7.20	7.13
C4	15.4	15.2	15.6	15.6	15.6
C5	7.93	7.76	7.94	8.08	8.07
C6	24.3	22.8	23.4	24.0	23.9

tively. Realistic perennial snow cover is seen over the high elevation areas of Alaska and Baffin Island in the highest subgrid resolution case. The geographical distribution of net accumulation in the 116 kaBP simulation with the lowest and the highest subgrid resolutions are also shown in Figs. 5.4**b** and 5.5**b**, respectively. A small expansion of perennial snow cover is seen in Alaska in the lowest subgrid resolution case and in northwestern Canada in the highest subgrid resolution case. The expansion of perennial snow cover in Baffin Island is in line with the geological evidence (Clark et al. 1993). Unfortunately, due to the low resolution, parts of Baffin Island are represented as ocean rather than land in this model. In addition, it was not clear until after the ice sheet model was interactively integrated at this higher resolution, that the observed perennial snow cover would expand under 116 kaBP forcing and not under present-day forcing. More importantly, there is no perennial snow cover seen in Keewatin and Labrador.

Temperature forcing affects the mass balance in two ways: 1) a temperature drop (increase of threshold temperature) contributes to an increase of the fraction of precipitation that falls as snow, and a consequently to an increase in snow melting under a warmer climate; 2) a temperature drop decreases snow melting if all else remains equal. As the increase of snowfall is larger than the increase of snow melting, temperature drop contributes to positive net accumulation (C3 and C4). Net accumulation roughly doubles for an increase of threshold temperature by 2.5°C. The geographical distribution of net accumulation with the lowest and the highest subgrid resolutions in experiment C4 are shown in Figs. 5.4c and 5.5c, respectively. In both the lowest and highest subgrid resolution cases, a large increase in perennial snow cover is seen in Alaska, northwestern Canada, and Baffin Island. Despite the relatively large temperature perturbation, there is virtually no perennial snow cover seen in Keewatin and Labrodor.

Similar to the temperature forcing, precipitation forcing affects the mass balance in two ways: 1) a precipitation increase contributes to an increase of the snowfall rate, and consequently an increase of snow melting under a warmer climate; 2) a decrease in snow melting rate occurs through the ice-albedo feedback. As the increase of snowfall is much larger than the increase of snow melting, the net result is a positive net accumulation (C5 and C6). Net accumulation varies nonlinearly with the increase in total precipitation. For the highest subgrid resolution, for example, the net accumulation increases by 2.4 times and 7.2 times when precipitation is doubled and quadrupled, respectively. The geographic distribution of net accumulation with the lowest and highest resolutions in experiment C6 are shown in Figs. 5.4d and 5.5d, respectively. In the highest subgrid resolution case, a large expansion of perennial snow cover is seen in northwestern Canada. Despite the relatively large precipitation perturbation, there is again no perennial snow cover seen in Keewatin and Labrodor.

5.3.2 The effect of subgrid ice-flow

In subsection 5.3.1, a perennial snow cover was simulated in parts of Baffin Island. It is not clear, however, whether the perennial snow cover is enough to expand to surrounding areas of lower elevation. The ice thickness at the selected subgrid elevation levels (16, 11, 6, and 1) in the present-day simulation (D1) are shown in Figs. 5.6a–5.6d, respectively. In the highest subgrid elevation levels (level 16), perennial snow cover is seen in most of the high elevation areas over the globe e.g., the Himalayas, Rockies, and Andes, and the two polar ice sheets: Greenland and Antarctica. Ice at the intermediate subgrid elevation level (level 11) in Alaska is thicker than that at the highest elevation level. As the precipitation rates are the same within a grid cell, this is caused by subgrid ice-flow. In the lowest level (level 1), there is no perennial snow cover except over Greenland and Antarctica, consistent with observations. The ice thickness at the selected subgrid elevation levels (16, 11, 6, and 1) in the 116 kaBP simulation (D2) are shown in Figs. 5.7a–5.7d, respectively. No striking differences are seen from the present-day simulation, particularly at the lowest subgrid elevation level. This suggests that although the model can simulate the perennial snow cover at the small area of high elevation in Baffin Island, it does not allow for the further expansion through downslope ice flux. Therefore, the coupled climate model fails in this last glacial inception benchmark test.

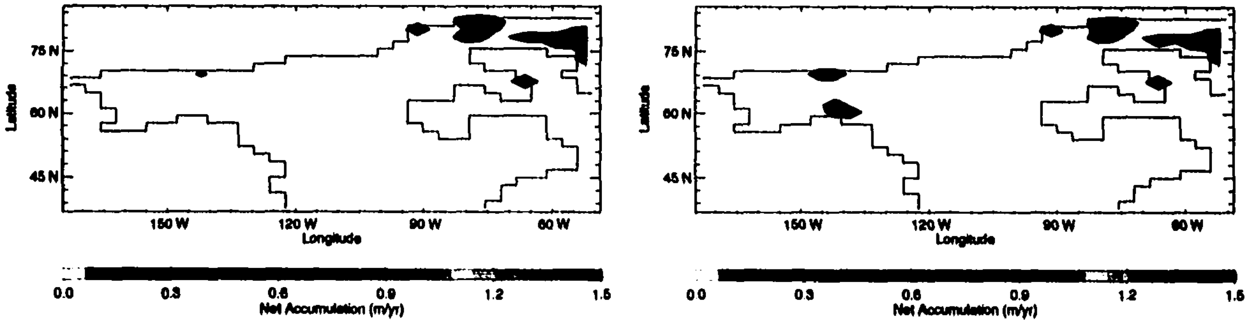

a present-day simulation (C1)

b 116 kaBP simulation (C2)

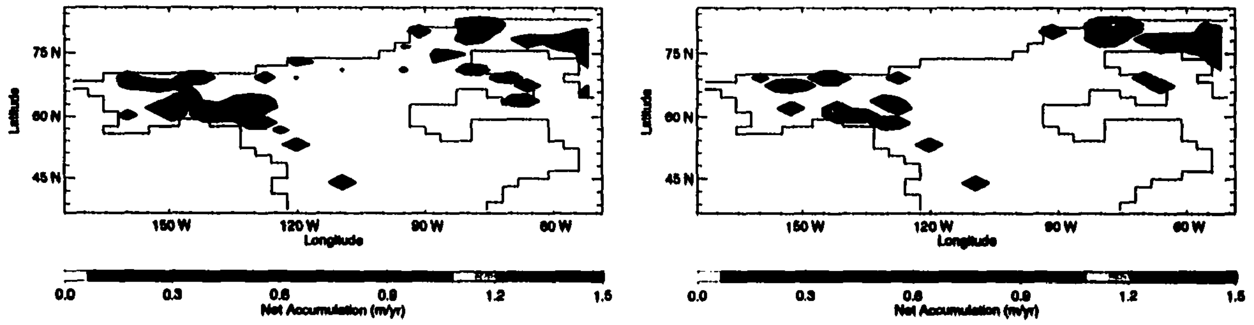

c 116 kaBP experiment with temperature forcing (C4)

d 116 kaBP experiment with precipitation forcing (C6)

Figure 5.4: **Annual mean net accumulation with the lowest subgrid resolution (M1).**

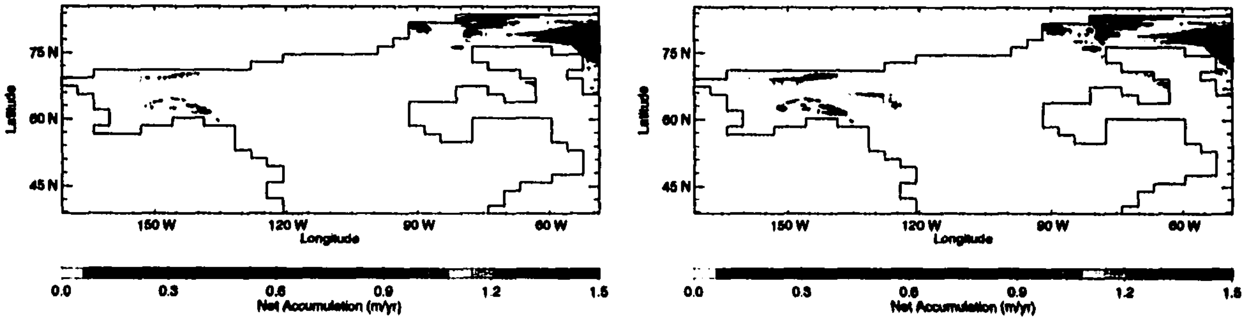

a present-day simulation (C1)

b 116 kaBP simulation (C2)

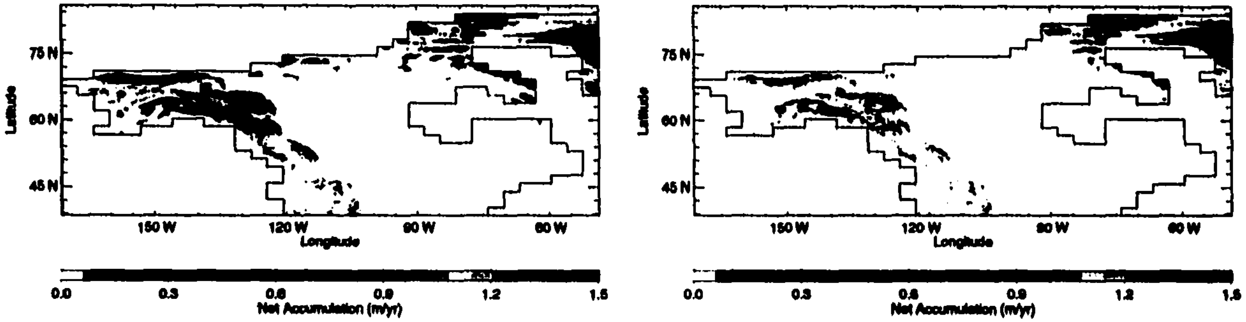

c 116 kaBP experiment with temperature forcing (C4)

d 116 kaBP experiment with precipitation forcing (C6)

Figure 5.5: **Annual mean net accumulation with the highest subgrid resolution (M5).**

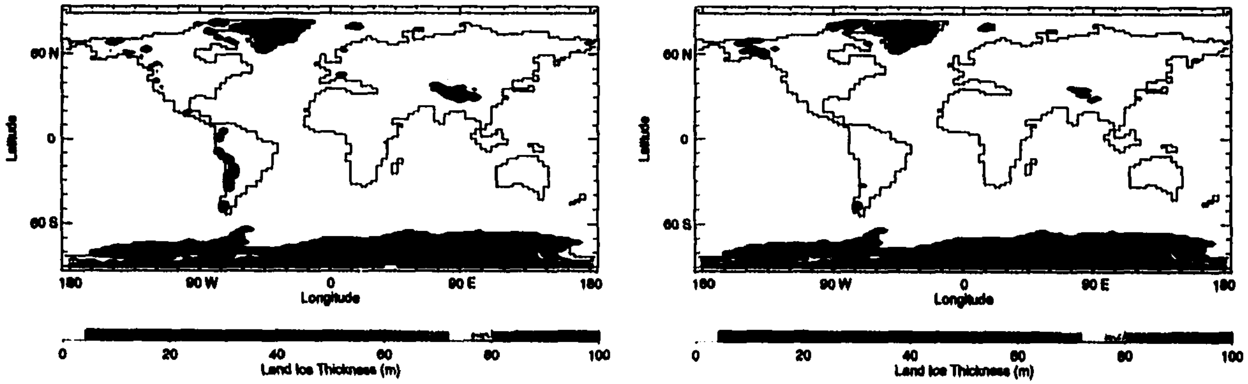

a The highest subgrid elevation level (level 16)

b Intermediate subgrid elevation level (level 11)

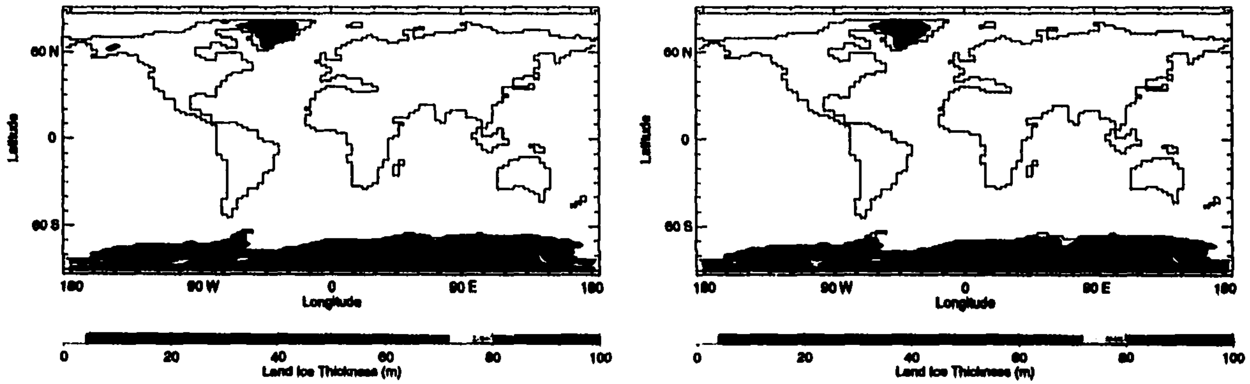

c Intermediate subgrid elevation level (level 6)

d The lowest subgrid elevation level (level 1)

Figure 5.6: **Ice thickness at selected subgrid elevation levels in the present-day simulation.**

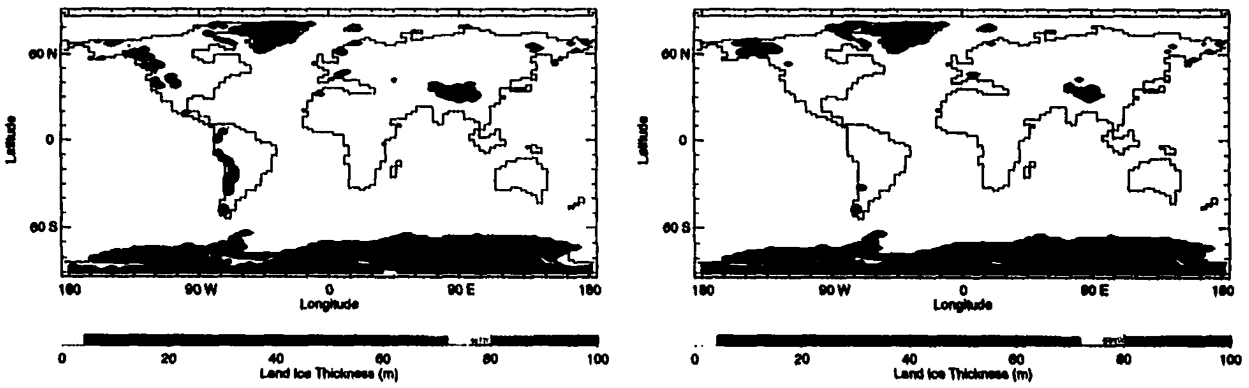

a The highest subgrid elevation (level 16)

b Intermediate subgrid elevation level (level 11)

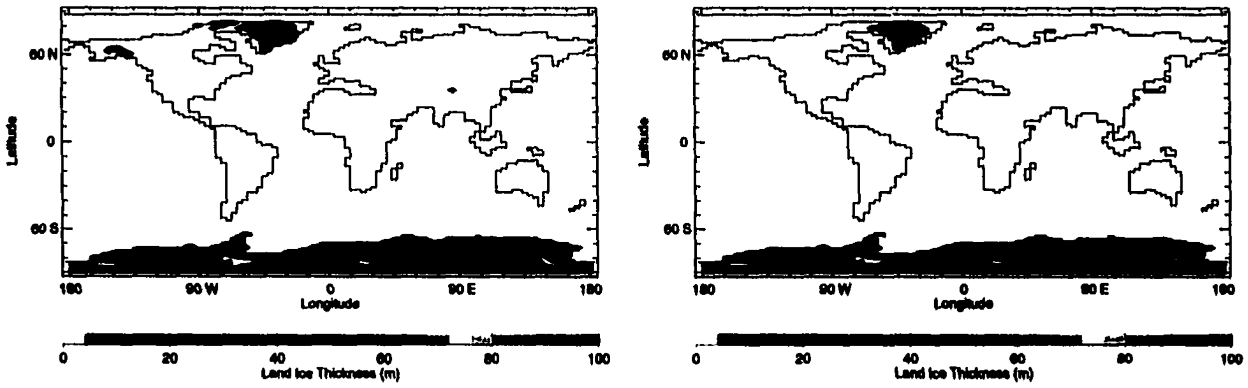

c Intermediate subgrid elevation level (level 6)

d The lowest subgrid elevation level (level 1)

Figure 5.7: **Ice thickness at selected subgrid elevation levels in the 116 kaBP simulation.**

5.4 Discussion and conclusion

In this study, the simplest down-scaling technique was undertaken to calculate the SAT in each subgrid cell. The lapse rate used was the global average for a free atmosphere (6.5°C km^{-1}). Different researchers use different values as a constant lapse rate. For example, 7.0, 7.5, and 9.0°C km^{-1} are used by Pollard and Thompson (1997), Tarasov and Peltier (1997b;a; 1999), and Marshall and Clarke (1999), respectively. As these differences in lapse rate produce significant differences in SAT, more sophisticated down-scaling techniques which include the explicit calculation of the lapse rate are necessary. A difference of 1.0°C km^{-1} in lapse rate produces more than 1.0°C difference in the highest point of Baffin Island, for example.

The lack of atmospheric dynamics, cloud feedback, and a land surface model are of course potential reasons for the failure of the climate model to capture glacial inception. It is not, however, easy to rule out the possibility of a bias arising from the control climate bias. Another possible reason is that the current version of the coupled climate model applies a relatively weak albedo difference (~0.18) in the presence of snow or ice cover over land. The justification for the use of such a small value comes from the fact that it represents changes in planetary albedo rather than surface albedo. It is, however, noteworthy that a strong albedo difference (~0.3) was required to reproduce a realistic simulation of the late Oldovician glaciation in this coupled climate model (Poussart et al. 1999). Note that a sensitivity analysis to the lapse rate and albedo feedback are not performed in this study as the use of larger lapse rate or higher albedos significantly distorts the present-day climate which complicates the interpretation even if realistic glacial inception occurs.

The inclusion of subgrid topography leads to the simulation of a more realistic present-day ice distribution in Alaska and Baffin Island, consistent with the results obtained by Marshall and Clarke (1999). Under 116 kaBP forcing, a small expansion of perennial snow cover occurs over northwestern Canada and Baffin Island with the highest subgrid resolution. With the inclusion of subgrid flow of ice, these regions of perennial snow cover, however, do not grow to form a large ice sheet. Instead, the ice flows to the lower subgrid elevations and melts there. Under temperature and precipitation forcing, it was revealed that northwestern Canada and Alaska are the "glaciation sensitive" areas of the coupled climate model, as observed in other models (Oglesby 1990; Dong and Valdes 1995). No perennial snow cover occurred over Keewatin and Labrador. Results obtained here are, nevertheless, instructive in that the effect of subgrid-scale topography is probably of secondary importance and improvements in the large-scale climatology may be of primary importance for the simulation of the last glacial inception.

Chapter 6

Glacial inception: Effect of surface conditions

6.1 Introduction

As the ability to capture the last glacial inception offers a test of the viability of climate models, including AGCMs, many studies regarding this event have been conducted (see Table 6.1). The first attempts to simulate glacial inception using an AGCM were carried out by Royer and Deque (1983) and Royer et al. (1984). In their experiments, only orbital parameters were changed with other boundary conditions remaining at modern values. Although they found several favourable conditions for ice sheet growth such as annual mean cooling over eastern Canada and increased precipitation over Canada, the occurrence of perennial snow cover was not reported. Also, uncertainty arose from the insufficient length of their integrations.

The issue concerning the difficulty in simulating the last glacial inception was first raised by Rind et al. (1989). They conducted several experiments under 116 kaBP and extreme orbital geometries. First, they investigated the occurrence of perennial snow cover with prescribed modern and predicted SSTs. Neither of them showed perennial snow cover over the desired areas. Second, they examined the maintenance of snow cover with the help of the ice albedo feedback, specifying 10 m land ice over the areas of CLIMAP LGM ice sheets (CLIMAP 1981) under modern and reduced atmospheric CO_2 concentrations. Again, neither of them revealed permanent snow cover. The second result has a different implication from the first, in the sense that it rejects some scenarios for glacial inception associated with hysteresis or natural climate variability from possible reasons for the failure of the simulation. Third, they examined the effect of colder SSTs by specifying CLIMAP LGM SSTs (CLIMAP 1981) and reduced (by 2°C) CLIMAP LGM SSTs. In combination with the prescribed initial 10 m land ice, they found permanent snow cover over northeast Baffin Island and eastern Scandinavia. However, the use of full glacial ocean conditions for the simulation of glacial inception, and the resulting inconsistency of the SSTs with applied orbital and CO_2 forcing, restricts the interpretation of the results.

A series of sensitivity experiments with respect to atmospheric CO_2 concentrations were conducted by Oglesby (1990) and Verbitsky and Oglesby (1992). Under the condition of greatly reduced atmospheric CO_2 concentration (100 ppmv) or initial imposition of 1 m snow cover over the entire NH, Oglesby (1990) found positive net snow accumulation over Alaska, western Canada, Siberia, and the Tibetan Plateau and not over eastern Canada nor Scandinavia. He defined these as "glaciation sensitive" areas. However, possible nonlinear responses due to the combination of orbital forcing and other feedback mechanisms such as changes in ocean circulation and land surface conditions might change the geographical distribution of "sensitive" areas. Also, it was pointed out that a longer integration may show these regions to be ice free (Phillipps and Held 1994). Verbitsky and Oglesby (1992) integrated an ice sheet-asthenosphere model for 25 ka, using AGCM results which are integrated under several atmospheric CO_2 concentrations. They found that the simulated maximum ice volume was about an order of magnitude less than estimates derived from proxy records. They concluded that CO_2 forcing alone could not account for the glacial inception, which is in line with the conclusion of Syktus et al. (1994).

Phillipps and Held (1994) and Gallimore and Kutzbach (1995), on the other hand, conducted a series of sensitivity experiments with respect to orbital parameters by specifying several extreme orbital configurations. These included a case with less obliquity and aphelion during the NH summer, which produces a cooler summer in the NH. Both studies came to a similar conclusion that although a "cold-summer" orbit brings the most favourable conditions for the development of permanent snow and expansion of glaciers, orbital forcing alone cannot account for the permanent snow cover in North America and Europe. This conclusion was also confirmed by Mitchell (1993), Schlesinger and Verbitsky (1996), and Vavrus (1999). Other interesting results found by Phillipps and Held (1994) and Gallimore and Kutzbach (1995) are the large sensitivity of sea ice to the changes in orbital parameters in terms of both areal coverage and thickness, and the accompaniment of Arctic sea ice expansion with favourable conditions for perennial snow cover. Further investigation with emphasis on the role of sea ice and similar conclusions were made by Vavrus (1999). Phillipps and Held (1994) were also unable to find the existence of multiple equilibria, consistent with the results of Rind et al. (1989).

Combinations of orbital and CO_2 forcing were studied by Syktus et al. (1994) and Schlesinger and Verbitsky (1996). Syktus et al. (1994), using an AGCM coupled to a dynamic upper ocean circulation model, found that the sensitivity of climate variables, such as surface mass balance, to orbital forcing is nonlinearly connected to CO_2 forcing. That is, the northern perennial snow and sea ice cover change dramatically with CO_2 concentration between 260 and 350 ppmv, but not between 350 and 460 ppmv, suggesting the existence of some critical threshold value close to the present-day CO_2 level. Schlesinger and Verbitsky (1996), integrating an ice sheet-asthenosphere model with AGCM output, found that a combination of orbital forcing and Greenhouse forcing caused by reduced CO_2 and CH_4 concentrations was enough to nucleate ice sheets in Europe and North America. However, the simulated global ice volume was only 31% of the estimate derived from proxy records. They attributed this underestimation to the neglect of the effect of ice sheet expansion through ice flow on climate. Only with the assumption of all precipitation over the ice sheets occurring as snow did the volume reach 86% of the estimated value. However, this assumption is crude and further attempts, for example, using an interactive integration involving an AGCM and ice sheet-asthenosphere model, are desirable.

By using a higher resolution model, Dong and Valdes (1995) simulated the growth of perennial snow under combined orbital and CO_2 forcing. As well as the resolution of the model, an important difference between their model and others was the use of "envelope orography" in which an additional increment, equal to two standard deviations of the subgrid scale high resolution orography, was added to the area mean orography. This technique was introduced to improve the dynamical aspect of the atmospheric circulation (to compensate for insufficient orographic forcing in maintaining stationary waves), and its thermal impact, including the snow budget, should be verified. They also found that the changes in SST due to orbital perturbations played a very important role in initiating the Laurentide and Fennoscandian ice sheets.

The role of the biosphere in glacial inception has been studied by Gallimore and Kutzbach (1996), de Noblet et al. (1996), and Pollard and Thompson (1997). Gallimore and Kutzbach (1996) integrated an AGCM with a mixed layer ocean model under five different forcing: 1)- control; 2)- orbital; 3)- 2) plus CO_2; 4)- 3) plus 25% expansion of tundra based on the study of Harrison et al. (1995); and 5)- 4) plus further 25% expansion of tundra. The effect of the expansion of tundra through a vegetation-snow masking feedback was approximated by increasing the snow cover fraction. In only the last case was perennial snow cover observed. De Noblet et al. (1996) coupled a global biome model to an AGCM and integrated iteratively (five iterations) to study the possible role of vegetation in the climate system with present-day SST and sea ice and reduced CO_2 concentration. They found, firstly, that 115 kaBP orbital forcing was insufficient to start glaciation. Secondly, summer temperatures were lowered and tundra expanded southward as the iteration was repeated. They found a consistent trend towards cooler summer SAT and greater snow accumulation over

Quebec/Labrador, central Canada, Greenland and the Canadian Arctic, northern/western Scandinavia, northern Siberia, and Tibet, indicating a significant biospheric feedback. However, no ice remained during August and September over eastern Canada.

Pollard and Thompson (1997) also conducted an interactive vegetation and AGCM experiment under both orbital and CO_2 forcing. They further integrated a dynamic ice sheet model for 10 ka under the surface mass balance calculated from AGCM output using a multi-layer land surface model on the grid of the ice sheet model. They included the process of refreezing of rain and meltwater into the ice sheet mass balance. Although their model predicted the growth of an ice sheet over Baffin Island and the Canadian Archipelago, it also predicted a much faster growth rate in northwestern Canada and southern Alaska, and no nucleation was seen on Keewatin or Labrador. Furthermore, the rate of increase in ice volume was an order of magnitude less than that estimated from proxy records.

It is difficult to synthesise the results of these studies since each model used different parameterisations of unresolved physical processes, resolution, and had different control climates as well as experimental design. However, some synthesis may be addressed: 1) neither orbital forcing alone (Gallimore and Kutzbach 1995; Mitchell 1993; Phillipps and Held 1994; Rind et al. 1989; Vavrus 1999) nor CO_2 forcing alone (Verbitsky and Oglesby 1992; Syktus et al. 1994) can account for the last glacial inception; 2) results of the combined effects of these two contributions to the forcing are not consistent (Rind et al. 1989; Gallimore and Kutzbach 1996; Syktus et al. 1994; Dong and Valdes 1995); and 3) the difficulty in simulating perennial snow cover is not related to the existence of multiple equilibria (hysteresis or natural variability), but to the resolution of the model or the overlooked role of the biosphere.

On the other hand, a common uncertainty arises from the use of prescribed present-day sea surface conditions or a mixed layer ocean model. Note that Khodri et al. (2001) conducted a glacial inception simulation using a fully coupled atmosphere-ocean GCMs at the time of writing of this dissertation. Their model successfuly simulated a permanent snow cover over northeastern Canada. The length of their integration (100 years from the present-day control simulation under 115 kaBP orbital forcing), however, is not sufficient for the study of processes involving deep ocean changes. To investigate the role of changes in ocean conditions in the last glacial inception and the role of changes in vegetation associated with changes in ocean conditions, several experiments are conducted here using an AGCM. Different ocean conditions are provided by the coupled climate model simulation. The strengths of the coupled climate model lie in the detailed physics of the ocean and sea ice components and non-drifting, but realistic, simulated present-day climate without flux adjustments. Its weaknesses are the simplified atmosphere and land surface components. The strengths of the AGCM are, of course, the detailed physics of the atmosphere and land surface. However, it requires prescribed lower boundary conditions. Using SST and sea ice fields from the coupled climate model in the AGCM allows AGCM experiments with lower boundary conditions broadly consistent with external forcing.

6.2 *Experimental design*

All integrations conducted in this study are summarised in Table 5.1 and Table 6.2, and the experimental procedures are described in Fig. 6.1. The coupled atmosphere-ocean-sea ice climate model was integrated under two different sets of orbital and CO_2 forcing: present-day and 116 kaBP (B1 and B2 in Table 5.1). The same initial conditions described in section 3.2 were applied for both spin-ups. The climate model was integrated for 2000 years by which time a quasi-steady state was reached. It was then integrated for another year to obtain equilibrium monthly fields which include SST, sea ice thickness, areal fraction of sea ice cover, and SAT (Fig. 6.1). Note that the use of multi-year averaged data instead of one-year data does not produce any significant difference due to little internal climate variability existing in the climate model.

Present-day and 116 kaBP sea surface conditions used as lower boundary conditions of the AGCM were established from the equilibrium monthly fields. For the open ocean, the climate model-simulated SST and sea ice amounts obtained from B1 and B2 (Table 5.1) were used as present-day (E3 and E5) and 116 kaBP (E4 and E6) conditions, respectively. An alternate approach could have been to use observed values as present-day conditions, and the sum of observed values and anomaly (the difference between 116 kaBP and present-day simulations) as 116 kaBP conditions. This alternate approach, however, produced unphysical values (e.g., more than 100% areal fraction of sea ice cover). Therefore, the approach was avoided, except for surface water temperatures where the grid point was specified as land in the climate model, but recognised as water in GCMII (Baltic Sea, Black Sea, Caspian Sea, and Red Sea). In this case, the SAT difference was used for the surface water temperature difference, limiting the resulting minimum temperature at 116 kaBP to the freezing point of water.

To study the sensitivity of the AGCM to the lower boundary conditions, GCMII (see section 2.3) was integrated with four different lower boundary conditions (E3–E6 in Table 6.2) in addition to two present-day simulations (E1 and E2 in Table 6.2). GCMII was integrated for 10 years after a spin-up of 1 year and 2 months, and the seasonal averages

Table 6.1: **AGCM simulations (1) (after Mitchell 1993)**

Studies	Atmosphere model	SST or ocean model	Orbital Parameters	CO_2/CH_4 (ppmv)	Initial land snow/ice	Other Parameters
Royer et al. (1983; 1984)	EERM 32×20/L10	PD	PD; 115 kaBP 125 kaBP	PD	PD	
Rind et al. (1989)	NASA GISS 10°×8°/L9	PD; ML; CL81 CL81−2°C	PD, 116 kaBP extreme values	PD (=310) 240	PD CL81 10 m ice	
Oglesby (1990)	NCAR CCM1 7.5°×4.5°/L12	PD ML	PD	100–1000 (PD= 330)	PD NH 1 m snow PD - Antarctica	roughness snow fraction topography
Verbitsky and Oglesby (1992)	NCAR CCM1 7.5°×4.5°/L12	PD CO_2-dependent	PD	100–1000 (PD= 330)	NH 10 m snow	ablation
Mitchell (1993)	Hadley Centre 3.75°×2.5°/L19	PD	115 kaBP 125 kaBP	PD	PD	
Syktus et al. (1994)	CISRO4 R21/L4	DU	PD 116 kaBP	100–3500 (PD= 350)	PD	solar constant
Phillipps and Held (1994)	NOAA GFDL R15/L9	ML	extreme values	PD	PD	solar constant cloud surface albedo

PD: present-day; ML: mixed layer ocean model; DU: dynamic upper ocean circulation model; CL81: CLIMAP 1981; NH: Northern Hemisphere; see Glossary of Acronyms

Table 6.1 cont.: AGCM Simulations (2)

Studies	Atmosphere model	SST or ocean model	Orbital Parameters	CO_2/CH_4 (ppmv)	Initial land snow/ice	Other Parameters
Gallimore and Kutzbach (1995)	NCAR CCM1 T10/L5	ML	extreme values	PD	PD	
Dong and Valdes (1995)	UGAMP T42/L19	PD, PD−2°C ML	PD 115 kaBP	PD (= 345) 280	PD	resolution
Gallimore and Kutzbach (1996)	NCAR CCM1 T10/L5	ML	PD 115 kaBP	PD (= 330) 267	PD	vegetation
Schlesinger and Verbitsky (1996)	OSU 5°×4°/L2	ML	PD 115 kaBP	PD (= 326) 275; 246	none	snow fraction ice dynamics
de Noblet et al. (1996)	LMD 5.3 64×50/L11	PD	PD 115 kaBP	PD (= 345) 280	PD	vegetation
Pollard and Thompson (1997)	NCAR GENESIS2 T31/L18	ML	PD 116 kaBP	PD (= 345/1.653) 314/1.088	none	ice dynamics
Vavrus (1999)	NCAR GENESIS2 T31/L18	ML	PD; 6 kaBP 115 kaBP	PD	PD	sea ice dynamics
Khodri et al. (2001)	LMD 5.3 64×50/L11	OGCM	PD 115 kaBP	PD	PD	
This thesis	CCCma GCMII T32/L10	coupled model	PD 116 kaBP	PD (= 350) 240	PD	vegetation

Table 6.2: **Experiments using GCMII (PD: present-day)**

Experiments	Orbital parameters	CO_2 (ppmv)	Ocean surface	Land surface
E1	PD	350	observed PD	observed PD
E2	PD	350	B1	observed PD
E3	116 kaBP	240	B1	observed PD
E4	116 kaBP	240	B2	observed PD
E5	116 kaBP	240	B1	modified based on E3
E6	116 kaBP	240	B2	modified based on E4

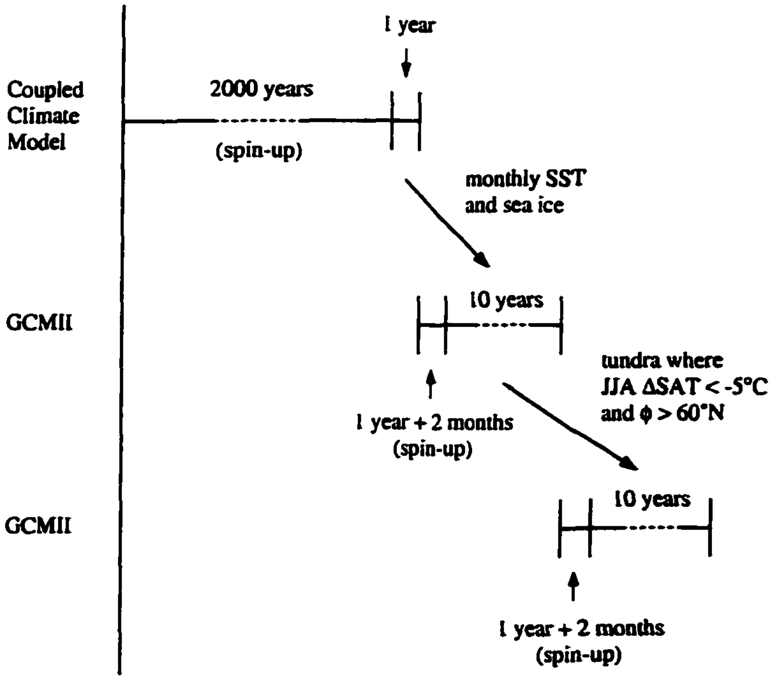

Figure 6.1: **Experimental procedures (see text for details).**

over the last 10 years were mainly analysed. The purpose of the two present-day simulations are to evaluate the extent of errors induced by using simulated sea surface conditions rather than observed conditions. Thereafter, E2 is defined as the control simulation. Two 116 kaBP experiments were conducted to investigate the effect of changes in sea surface conditions on the AGCM results (E3 and E4 in Table 6.2). In nature, vegetation changes as climate changes, and hence the simulated 116 kaBP climate is not necessarily consistent with the specified vegetation. Therefore, two additional experiments were conducted to investigate the combined effect of changes in sea surface conditions and vegetation (E5 and E6 in Table 6.2).

Changes in vegetation as lower boundary conditions were implemented as follows. In nature, the distribution of vegetation varies primarily with temperature and water availability. However, only the dependence of vegetation type on temperature was considered in this study for simplicity. If the difference relative to the control integration in SAT during summer (JJA) was less than -5°C, all vegetation types were changed to tundra. Here, SAT represents air temperature at the 2 m screen level and it was obtained by averaging data over the last 10 years in each integration in E2, E3, and E4. This treatment is crude, but reasonable for sensitivity experiments, since the boreal forest would not likely survive in such a colder climate. The use of actual temperature, rather than temperature change from the control simulation, for the constraint of vegetation field is possible, but it would undoubtedly amplify the influence of any biases in the present-day control simulation. Considering that the strength and uniqueness of the present approach taken is a clean separation of the effect of orbital and CO_2 forcing, sea surface conditions, and land surface conditions on glacial inception, modifying vegetation based on temperature change is consistent with the objective of this study. The unrealistic expansion of tundra in low and mid latitudes arising from the use of temperature change, rather than actual temperature, was avoided by restricting this alteration to grid points north of 60°N. The modification of vegetation in E5 was based on the difference between E3 and E2 while that in E6 is based on the difference between E4 and E2. These changes in vegetation affect climate through changes in soil depth, evapotranspiration slope factor, snow masking depth (McFarlane et al. 1992), and albedo (Wilson and Henderson-Sellers 1985). For consistency with other tundra areas in the model, the bare soil fraction was changed to 0% in each grid cell where tundra was specified.

6.3 Results

6.3.1 Coupled model simulated sea surface conditions

Two sea surface conditions were simulated using the coupled climate model: present-day (B1) and 116 kaBP (B2). Figures and a detailed description of the simulated present-day sea surface conditions, as well as other climatic fields are found in Weaver et al. (2001), in which a nearly identical model was used. Only a brief description of simulated SST and sea ice cover for the present-day simulation is given here without figures. The model captures the main characteristics in observed SST in terms of geographical structure and magnitude. However, there are some discrepancies between the simulation and observations. In the North Pacific and the North Atlantic, simulated SSTs are too warm near the mid-latitude western coasts, due to western boundary currents separating too far north. In addition, the Gulf of Alaska and Norwegian Sea are too cold due to an underestimation of ocean heat transport (Fanning and Weaver 1997a), which in the latter case is due to deep water formation forming too far south. The simulated SST is too warm in the southern Indian Ocean which results from the Antarctic Circumpolar Current being steered southward by the Kerguelen plateau, thereby bringing relatively warm waters poleward.

The model captures the approximate ice thickness distribution found in observations. However, two distinct differences between the simulation and the observations occur. The model predicts thin ice cover over the Norwegian and Barents Seas in the NH winter and over the Barents Sea in the NH summer, while observations show ice-free conditions over the corresponding areas in the corresponding seasons. In short, the model overestimates the equatorward extension of ice cover in the North Atlantic. On the other hand, the model predicts a small ice-free area along the coast of East Antarctica all year round while observations show ice cover over the corresponding area. These areas are consistent with the areas of errors in the simulated SST which are mentioned above.

The difference between 116 kaBP and the present-day in the simulated SST is shown in Figs. 6.2a and 6.2b for the NH winter and summer, respectively. In both seasons, the SST in the 116 kaBP simulation is globally colder than in the present-day simulation. The difference between the 116 kaBP and present-day simulations in global and annual mean SST is 1.1°C. As the globally- and annually-integrated insolation between the two simulations is virtually the same, this cooling is attributed to the difference in the atmospheric CO_2 concentration. The largest cooling of up to about 6°C in both seasons is found in the northern North Atlantic and is accompanied by a reduction in the intensity of the meridional overturning and poleward heat transport in the North Atlantic. This reduction is caused by the decreased CO_2 concentration through tropical cooling, and increased freshwater flux due to melting of advected sea ice as described in Chapter 3. Zonal cooling of about 2–3°C is found between 40°N and 60°N in the NH summer. This cooling is due to the difference in insolation induced by the 116 kaBP "cold-summer" orbit. Note that there are no significant differences seen further north of 60°N (Arctic Ocean), despite the fact that the summer insolation anomaly is strongest in the NH high latitudes (Fig. 5.1**a**). This is simply because the SST reaches the freezing point.

To the author's knowledge, there are no global reconstructions of SST and sea ice cover around 116 kaBP. However, there exist reconstructions available in the North Atlantic, some of which suggest SST dropped by about 6–7°C around 115 kaBP (Dong and Valdes 1995), and the rest of which suggest the ocean surface cooling lagged behind the continental ice growth by about 3000 to 4000 years, with peak cooling around 110 kaBP (Ruddiman and McIntyre 1979 and Bradley 1999, Fig.6.12) or even later (McManus et al. 1994). Since the model is integrated under perpetual 116 kaBP forcing, it is difficult to validate it through a direct comparison with these reconstructions, which of course reflect transient stages. Nevertheless, model results are generally consistent with such an inferred cooling. Note that the purpose of this study is to investigate the sensitivity of climate to changes in sea surface conditions and not to decide if changes in sea surface condition acted as trigger or additional forcing (feedback) during the last glacial inception.

The difference between 116 kaBP and present-day in the simulated sea ice amount is shown in Figs. 6.3**a** and 6.3**b** for the NH winter and summer, respectively. Much thicker ice is seen in both the Arctic and Southern Oceans at 116 kaBP relative to the present.

In summary, the simulated present-day sea surface conditions are in good agreement with the observations except for two restricted regions in the polar oceans, suggesting that the use of the simulated fields as lower boundary conditions for the AGCM simulations is reasonable. The simulated 116 kaBP sea surface conditions are characterised by zonally cooler SST between 40 and 60°N and much thicker sea ice in the Arctic. Note that these fields (SST and sea ice amount) are obtained without any flux adjustment.

6.3.2 Present-day AGCM Simulations

To examine the bias in the simulated present-day climate potentially introduced by the use of the simulated sea surface conditions, rather than observed sea surface conditions, two present-day simulations were conducted using GCMII: one with the observed sea surface conditions (Alexander and Mobley 1976) — E1 and the other with the simulated sea surface conditions (E2). The differences in SAT between the simulations and observations

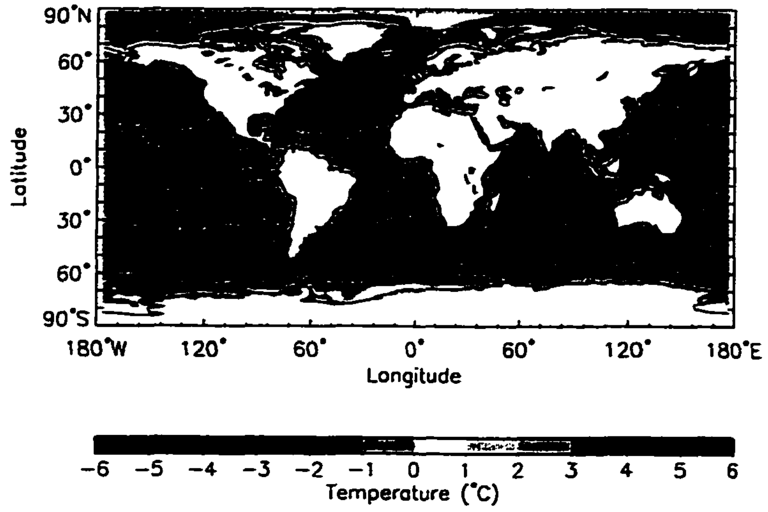

a DJF

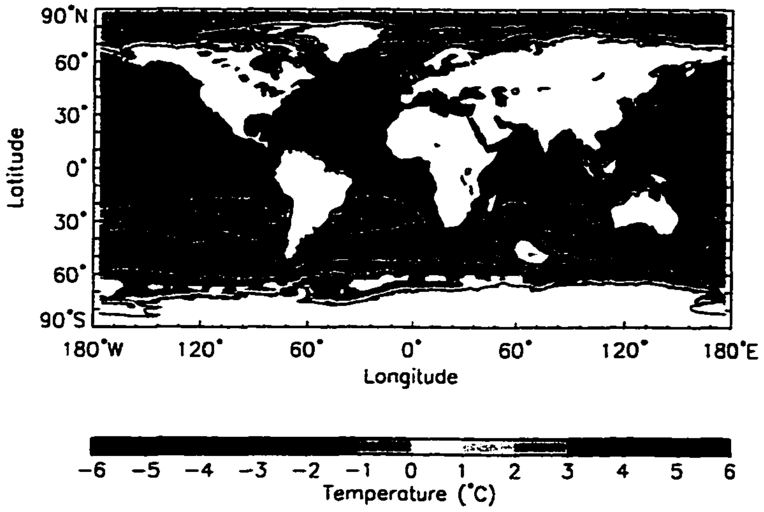

b JJA

Figure 6.2: **Differences in sea surface temperature (°C) between 116 kaBP (B2) and present-day (B1) from the coupled climate model simulations.**

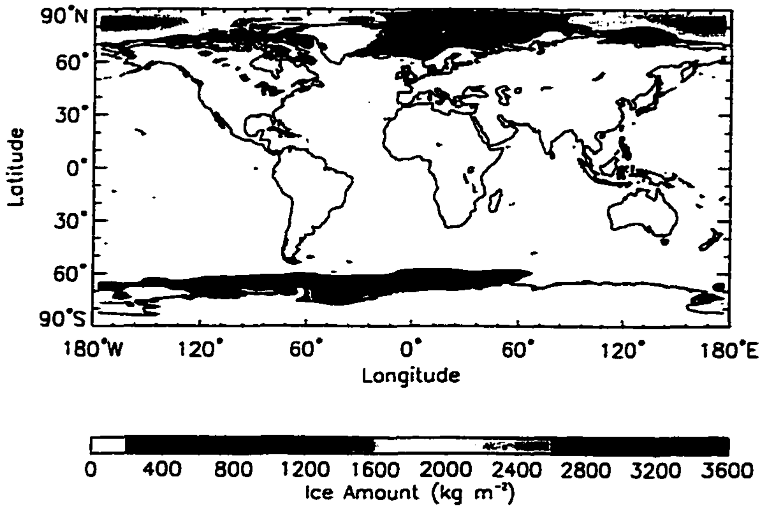

a DJF

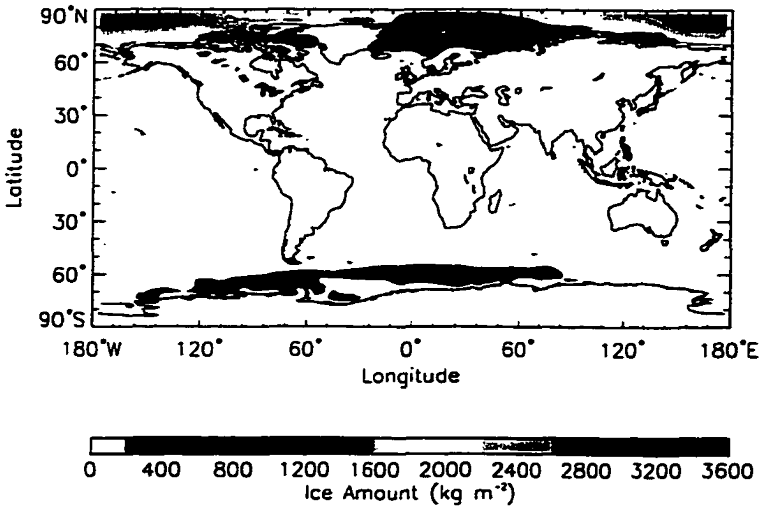

b JJA

Figure 6.3: **As in Fig. 6.2 but for differences in sea ice amount. Note that 1 kg m^{-2} is approximately equivalent to 1 mm in ice thickness.**

(operational analyses of the National Meteorological Center: 1989-1999) are shown in Figs. 6.4a-6.4d. The largest differences are seen over the Norwegian and Barents Seas in the NH winter, and to a lesser degree in the NH summer, and near the coast of East Antarctica in both seasons. These differences are consistent with corresponding errors in sea ice cover as mentioned in subsection 6.3.1. Smaller differences are also seen over the mid-latitude eastern edge of the North American and Eurasian continents in the NH winter, over the southern Indian Ocean in both seasons, and the mid-latitude over the North Pacific and the North Atlantic in summer. These differences reflect errors in SST. Notice that a slight cold bias is introduced over most of the NH continents in both seasons when simulated sea surface conditions are used. This is due to the existence of a slightly colder simulated SST in the North Pacific and the North Atlantic and their downstream zonal influence via the prevailing westerlies. The difference in precipitation between E2 and E1 is much smaller than between E1 and observations, and is not significant. The global, annual mean SAT is slightly warmer and net snow accumulation rate is larger in E2 than E1 (Table 6.3).

Table 6.3: **Annual mean response of the GCMII**

Global, annual mean field	E1	E2	E3	E4	E5	E6
SAT (°C)	13.4	13.6	13.4	11.8	13.4	11.6
Estimated sea level drop due to net accumulation over land (m yr^{-1})	0.0188	0.0210	0.0236	0.0256	0.0239	0.0299

In summary, although there are large biases in the present-day climate in some regions when simulated sea surface conditions are used, bias in northern North America is relatively small. Therefore, it is useful to conduct experiments which reveal a clean separation of the competing effects of orbital and CO_2 forcing, sea surface conditions, and land surface conditions in causing glacial inception. For consistency, the present-day simulation with the simulated sea surface conditions (E2) is defined as the control simulation hereafter.

6.3.3 116 kaBP AGCM Simulations

Effect of Sea Surface Conditions

To examine the effect of sea surface conditions (SST and sea ice) on the last glacial inception, two 116 kaBP experiments were conducted using GCMII: one with the simulated present-day

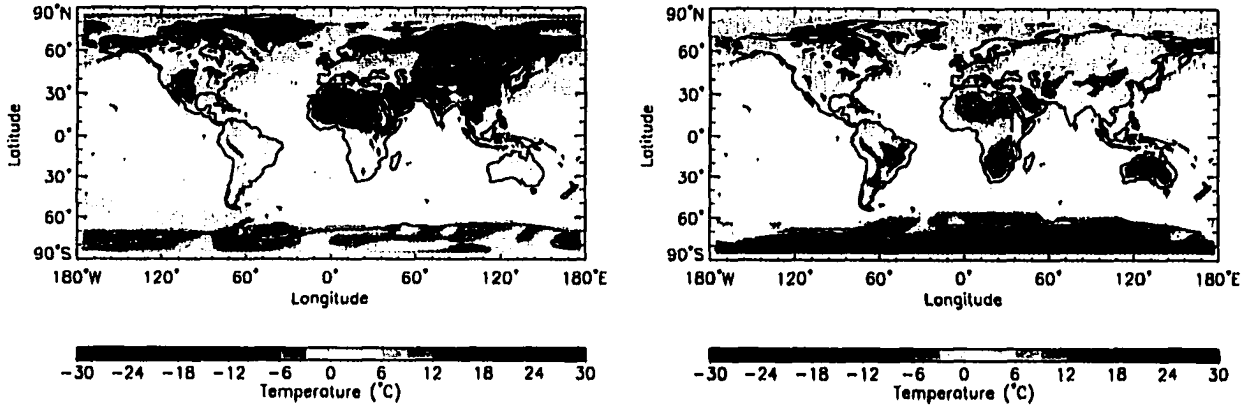

a DJF from the AGCM simulation with observed sea surface conditions (E1)

b JJA from the AGCM simulation with observed sea surface conditions (E1)

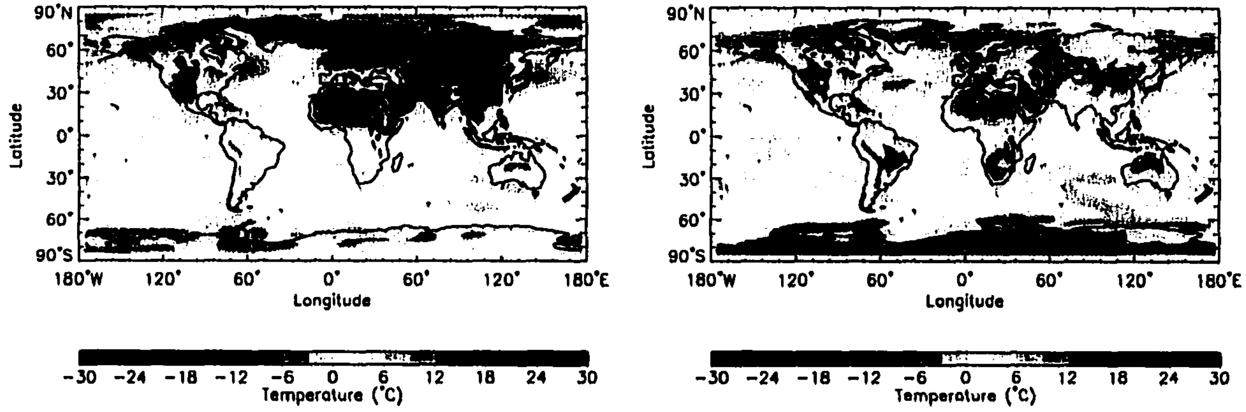

c DJF from the AGCM simulation with simulated present-day sea surface conditions (E2)

d JJA from the AGCM simulation with simulated present-day sea surface conditions (E2)

Figure 6.4: **Simulated minus observed surface air temperature (°C).**

sea surface conditions (E3) and the other with the simulated 116 kaBP sea surface conditions (E4). The global, annual mean SAT is much colder in E4 than E3 (Table 6.3). The net annual snow accumulation from E2, E3, and E4 are shown in Figs. **6.5a**, **6.5b**, and **6.5c**, respectively. As desired, the control simulation shows positive net accumulation only over Greenland and Antarctica where large ice sheets exist at present (Fig. **6.5a**). Despite the present-day sea surface conditions, additional perennial snow cover is found over the Queen Elizabeth Islands, Victoria Island, Banks Island, and Tibet-Himalayas under 116 kaBP orbital and CO_2 forcing (Fig. **6.5b**). When the 116 kaBP sea surface conditions are applied, perennial snow cover expands to cover northern Alaska, eastern Canadian Arctic/Keewatin, and northwestern Baffin Island, and Kamchatka (Fig. **6.5c**). It is interesting that the southward expansion of the perennial snow cover is not zonal, but most pronounced over the Keewatin area, little in Alaska, and none in western Canada, which is in good agreement with the geological reconstruction (Clark et al. 1993). The global, net snow accumulation rate in sea level equivalent is 2.6 m per 1000 yr in E3 and 4.6 m per 1000 yr in E4, relative to the control simulation (Table 6.3). While E3 largely underestimates the growth rate estimated from proxy records, E4 predicts a fairly accurate value. Interaction with ice dynamics and the inclusion of ice calving in the model, however, is necessary to be conclusive.

The differences in zonally-averaged annual snow budget between E3 and E2 and between E4 and E2 over North America (between 60°W and 120°W, excluding Alaska) are shown in Figs. **6.6a** and **6.6b**, respectively. The annual snow budget is determined by the balance between the amount of snowfall, snow melting, and sublimation. The figures show that the increased net accumulation and occurrence of the perennial snow cover in E3 and further expansion in E4 are due in large part to decreased snow melting. The reduction is consistent with the significantly colder summer compared to the control simulation (Fig. **6.7a**). Note that the colder summer itself is partly due to the perennial snow cover (a positive feedback). Although it would be interesting to know the relative importance of changes in SST and sea ice extent, decoupling each contribution is not easy.

It is noticeable that some of the contribution to the net accumulation difference comes from increased snowfall, especially in the most southern latitudes within the latitudinal band of positive net accumulation in Figs. **6.6a** and **6.6b**. It is, to some extent, counter-intuitive as a colder climate is generally expected to possess less precipitation due to a reduced hydrological cycle (Fig. **6.7b**). Figs. **6.8a** and **6.8b** show differences in zonally-averaged seasonal snowfall rate and seasonal precipitation rate over the North America between E4 and E3, respectively. It is clear that the increase of snowfall comes from the increased

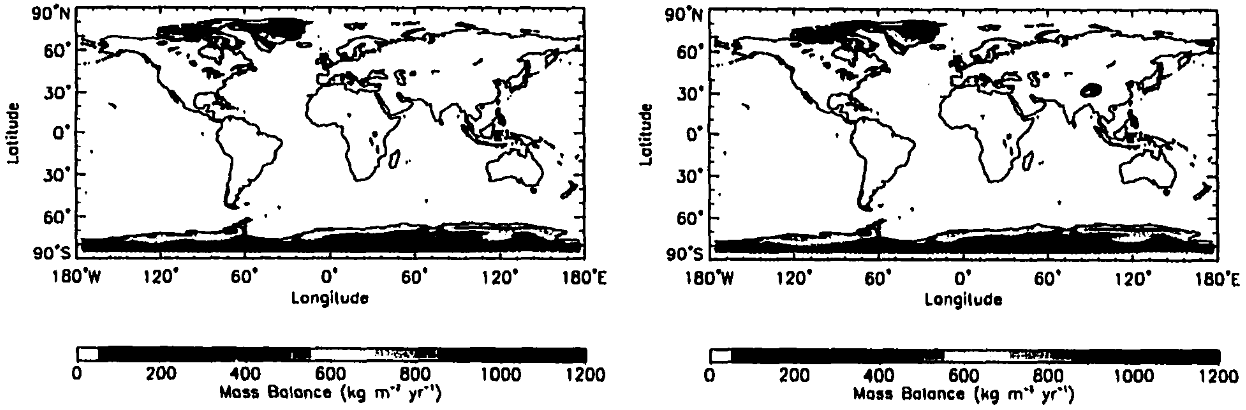

a Present-day AGCM simulation with simulated present-day sea surface conditions (E2)

b 116 kaBP AGCM simulation with simulated present-day sea surface conditions (E3)

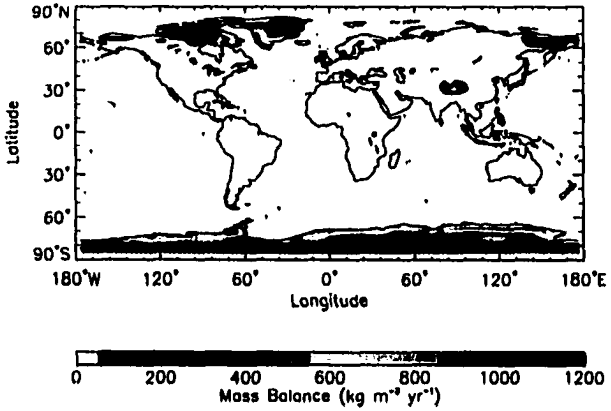

c 116 kaBP AGCM simulation with simulated 116 kaBP sea surface conditions (E4)

Figure 6.5: **Net annual snow accumulation rate (kg m^{-2} yr^{-1}).**

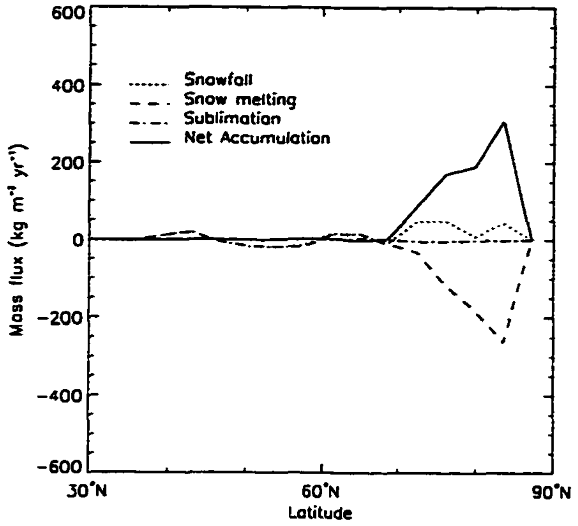

a Difference between the 116 kaBP AGCM simulation with simulated present-day sea surface conditions (E3) and the control run (E2)

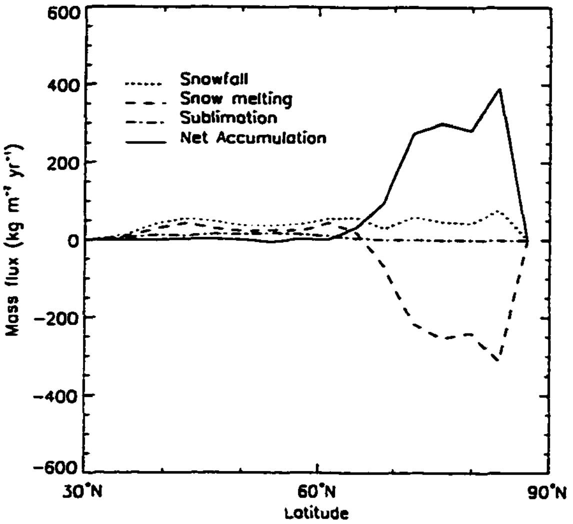

b Difference between the 116 kaBP AGCM simulation with simulated 116 kaBP sea surface conditions (E4) and the control run (E2)

Figure 6.6: **Annual snow budget (kg m^{-2} yr^{-1}). Data are extracted only over land between 60°W and 120°W (North America except Alaska) and then zonally-averaged.**

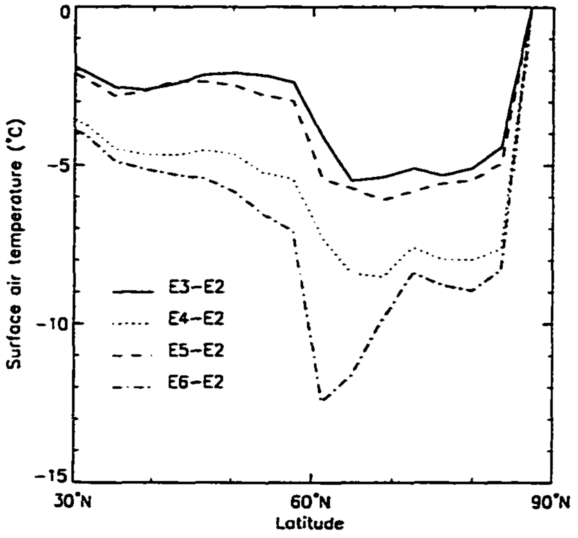

a Summer (JJA) surface air temperature (°C)

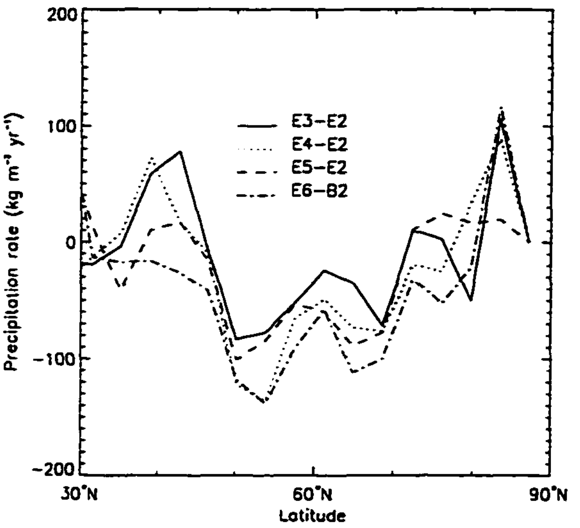

b Winter (DJF) precipitation rate (kg m^{-2} yr^{-1})

Figure 6.7: **Difference between 116 kaBP experiments (E3 – E6) and the control run. Data are extracted only over land between 60°W and 120°W and then zonally-averaged.**

fraction of snow in total precipitation due to the colder climate in E4, despite the fact that precipitation decreased between 45°N and 75°N in all seasons. In Fig. 6.8a, snowfall increased in lower latitudes (between 30°N and 55°N) during winter while it increased in higher latitudes (between 50°N and 75°N) during summer. The largest increase in snowfall occurred in fall and spring, suggesting the importance of these transition seasons for the annual snow budget. Notice that the reduced snowfall between 60°N and 75°N during spring and winter and between 75°N and 80°N during fall reflect the reduced precipitation during the corresponding seasons. This means that the amount of snowfall in these latitudes during these seasons is controlled by the total amount of precipitation rather than the temperature as it is already cold enough for precipitation to fall as snow. Figure 6.9 shows the difference in zonally-averaged seasonal snow melting rate over North America between E4 and E3. The decrease of annual snow melting rate is dominated by the decrease during summer.

Figure 6.10 shows the difference in zonally-averaged energy budget during summer at the surface over North America between E4 and E3. The decreased shortwave radiation absorbed at the surface, with its peak between 60°N and 70°N, reflects an increased surface albedo in the presence of snow rather than a cloud feedback. It is consistent with the extended perennial snow cover and resulting reduction in snow melting. It is interesting that the (upward) latent heat flux at the surface shows noticeable reduction, while the net longwave radiation and sensible heat flux show negligible change. In the model, the melting rate of snow is calculated from the residual of the energy flux at the surface. Therefore, the reduced latent heat flux acts as a positive contribution to snow melting by leaving more energy available for the melting process.

Effect of Land Surface Conditions

In the previous experiments, only changes in sea surface conditions were considered, with land surface conditions remaining the same, i.e., the present-day distribution of vegetation was specified. To examine the combined effect of sea surface (SST and sea ice) and land surface (vegetation) conditions on the last glacial inception, two additional 116 kaBP experiments were conducted: one with the simulated present-day sea surface and modified land surface conditions (E5); the other with simulated 116 kaBP sea surface and modified land surface conditions (E6). As mentioned already in section 6.2, the modification of vegetation in E5 is based on the difference in climate between E3 and E2, while that in E6 is based on the difference between E4 and E2.

The present-day distribution of tundra as a primary and a secondary vegetation in the NH (used in the control simulation), is shown in Figs. 6.11a and 6.11b, respectively.

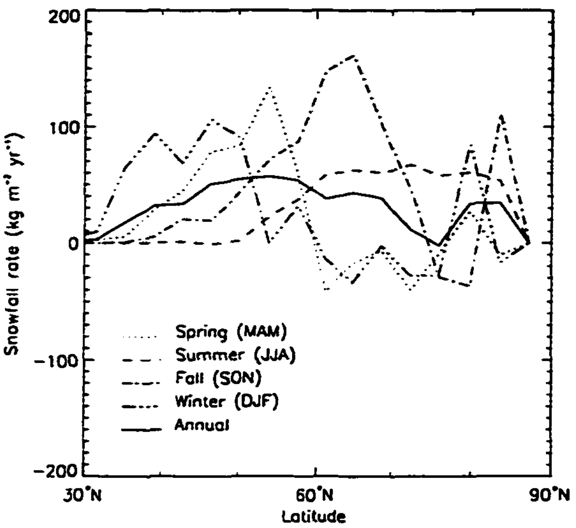

a Seasonal snowfall rate (kg m^{-2} yr^{-1})

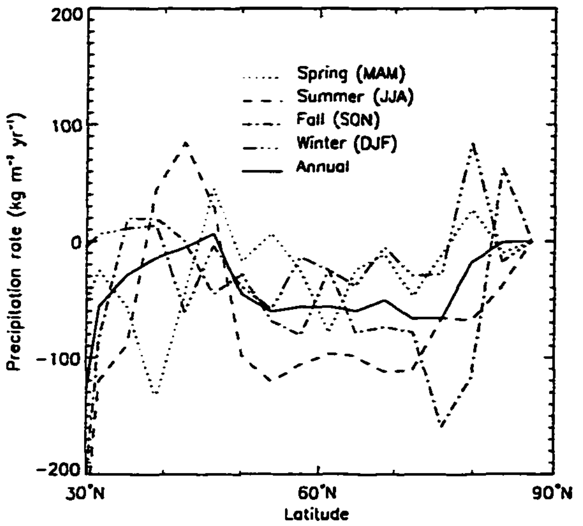

b Seasonal precipitation rate (kg m^{-2} yr^{-1})

Figure 6.8: **Difference between the 116 kaBP simulation with simulated 116 kaBP sea surface conditions (E4) and the 116 kaBP simulation with simulated present-day sea surface conditions (E3). Data are extracted only over land between 60°W and 120°W and then zonally-averaged.**

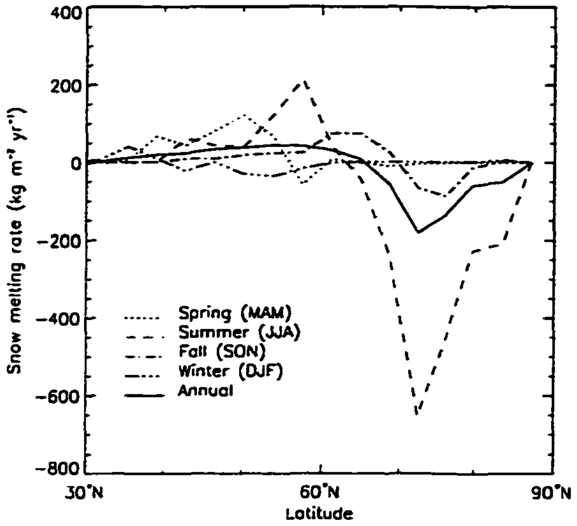

Figure 6.9: **Difference in seasonal snow melting rate (kg m^{-2} yr^{-1}) between the 116 kaBP simulation with simulated 116 kaBP sea surface conditions (E4) and the 116 kaBP simulation with simulated present-day sea surface conditions (E3). Data are extracted only over land between 60°W and 120°W and then zonally-averaged.**

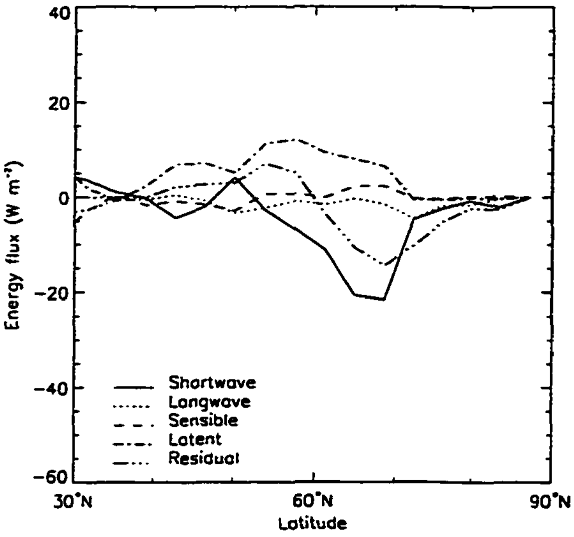

Figure 6.10: **Difference between E4 and E3 in summer energy budget at the land surface (W m^{-2}). Positive values represents net gain of energy for the surface while negative values represents net loss of energy for the surface. Data are extracted between 60°W and 120°W and then zonally-averaged.**

The modified distribution of tundra used in E5 shows little change from the present-day distribution except for secondary vegetation over Kamchatka (not shown). On the other hand, the modified vegetation used in E6 shows significant expansion of tundra resulting in vast areas of tundra north of 60°N (Figs. 6.11c,6.11d).

The net annual snow accumulation in E5 and E6 are shown in Figs. 6.12a and 6.12b, respectively. As expected from the existence of little change in vegetation, little difference is seen between E3 and E5 in which the present-day sea surface conditions are applied. On the other hand, large differences are seen between E4 and E6 in which the 116 kaBP sea surface conditions are applied (Fig. 6.12b). Additional expansion of perennial snow cover is seen over southern Alaska, western Canadian Arctic, Scandinavia, and Siberia. The resulting distribution of perennial snow cover is relatively zonal, which is also seen in other studies (Dong and Valdes 1995; Gallimore and Kutzbach 1996). The perennial snow cover over Alaska and northwestern Canada at 116 kaBP is probably unrealistic, although in order to determine whether this perennial snow cover could grow into an ice sheet would require the use of a dynamic ice sheet model. This discrepancy with geological records might be associated with cold biases in the present-day control simulation. The emergence of perennial snow cover over Scandinavia is interesting because it is in good qualitative agreement with palynological reconstructions in that first vegetation changed to tundra, and then the glaciation started on high mountain regions (Kukla 1980). However, the result in this area should be interpreted with caution as a relatively large cold bias is introduced in the present-day climate by using the simulated sea surface conditions rather than observed conditions. The global, net snow accumulation rate in sea level equivalent is 2.9 m per 1000 yr in E5 and 8.9 m per 1000 yr in E6, relative to the control run (Table 6.3). Similar to E3, E5 largely underestimates the growth rate estimated from the sea level records. On the other hand, E6 gives a realistic rate which can accommodate the rapid growth of ice during the last glacial inception.

The differences in zonally-averaged annual snow budget over North America between E5 and E2 and between E6 and E2 are shown in Figs. 6.13a and 6.13b, respectively. Again, the figures show that the increased net accumulation and occurrence of the perennial snow cover in E5 and further expansion in E6 are due in large part to decreased snow melting which is associated with a much colder climate. For the same reasons mentioned before, the increase in snowfall in E6 relative to E5, is explained by the increase in fraction of precipitation falling as snow despite a decrease in total precipitation.

Fig. 6.14 shows the difference in the zonally-averaged energy budget during summer at the surface over North America between E6 and E4, representing the effect of changes

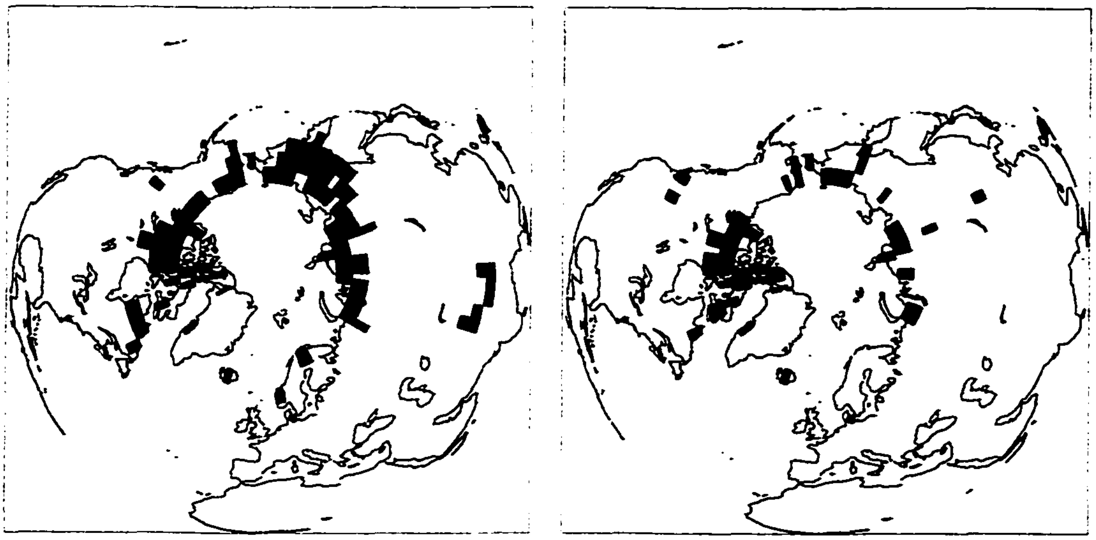

a Primary vegetation in E2, E3, and E4

b As in 6.11a but for secondary vegetation

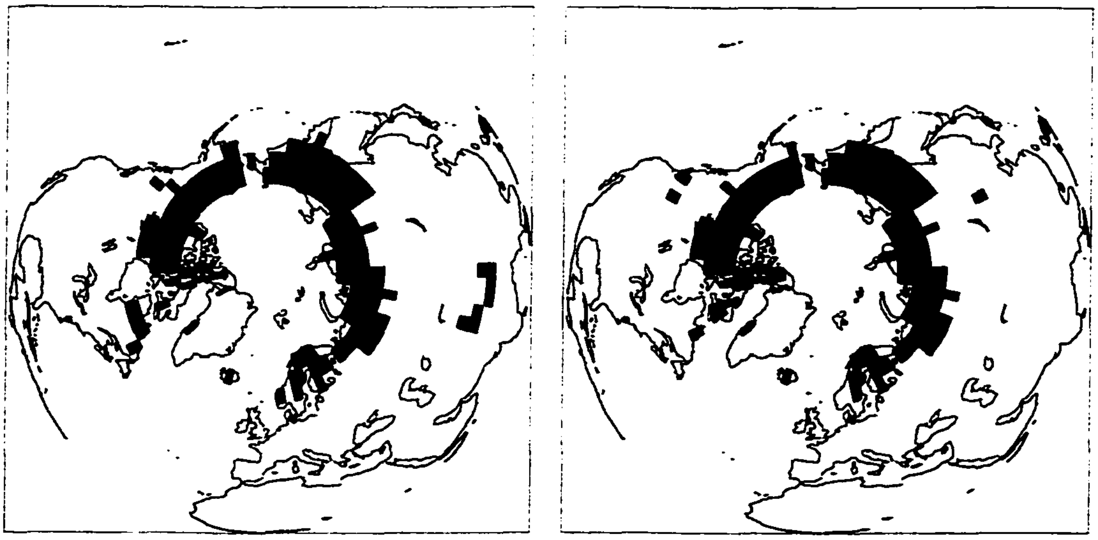

c Primary vegetation in E6

d As in 6.11c but for secondary vegetation

Figure 6.11: **Areas specified as tundra (shaded).**

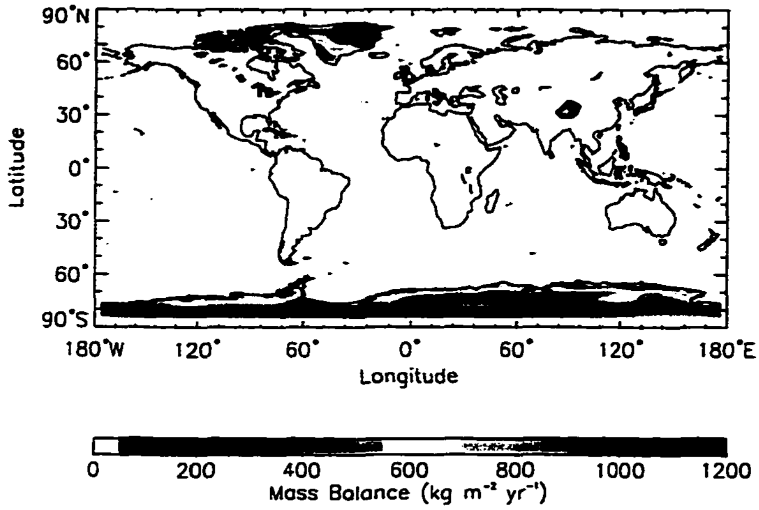

a 116 kaBP AGCM simulation with simulated present-day sea surface conditions and modified vegetation (E5)

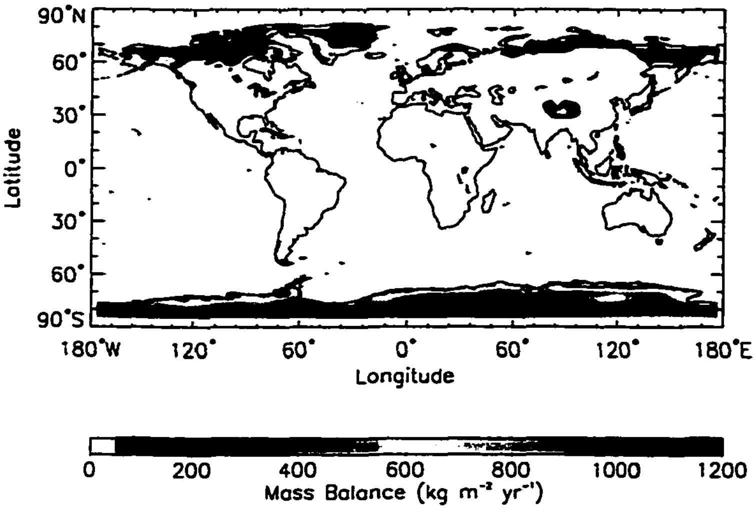

b 116 kaBP AGCM simulation with simulated 116 kaBP sea surface conditions and modified vegetation (E6)

Figure 6.12: **Net annual snow accumulation rate (kg m^{-2} yr^{-1}).**

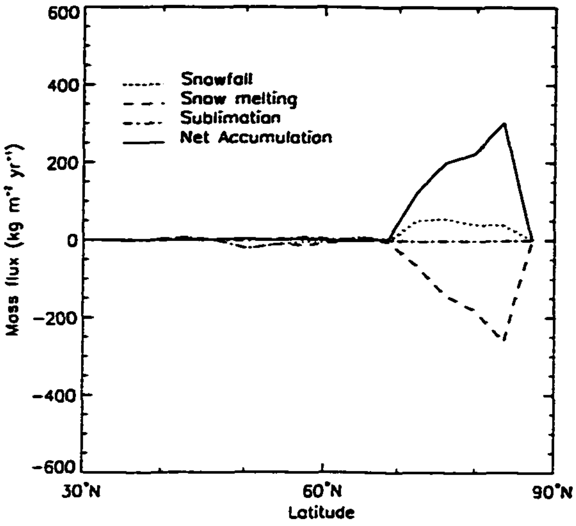

a Difference between the 116 kaBP AGCM simulation with simulated present-day sea surface conditions and modified vegetation (E5) and the control run (E2)

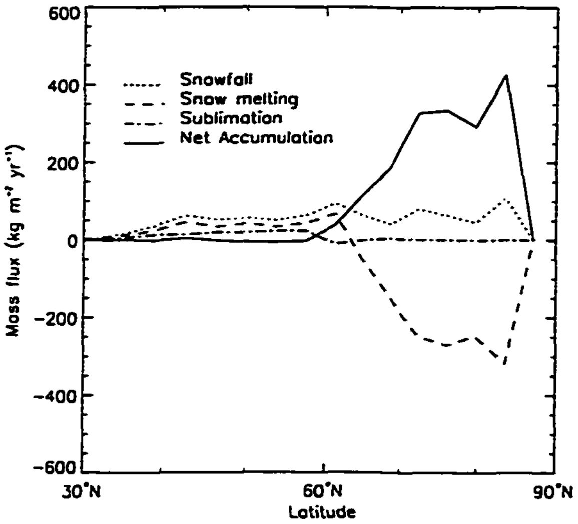

b Difference between the 116 kaBP AGCM simulation with simulated 116 kaBP sea surface conditions and modified vegetation (E6) and the control run (E2)

Figure 6.13: **Annual snow budget (kg m^{-2} yr^{-1}). Data are extracted only over land between 60°W and 120°W and then zonally-averaged.**

in vegetation, excluding the effect of changes in sea surface conditions. The decreased shortwave radiation absorbed at the surface, with its peak between 60°N and 70°N, is consistent with the extended perennial snow cover. The decreased absorbed shortwave radiation is largely compensated for by a reduction of upward net longwave radiation and sensible and latent heat fluxes, with the latent heat flux showing the second largest changes. It is noteworthy that the expansion of tundra over the area north of 60°N affects the climate south of 60°N, as shown in Fig. 6.7a, although the effect is not seen significantly in the energy fluxes at the surface.

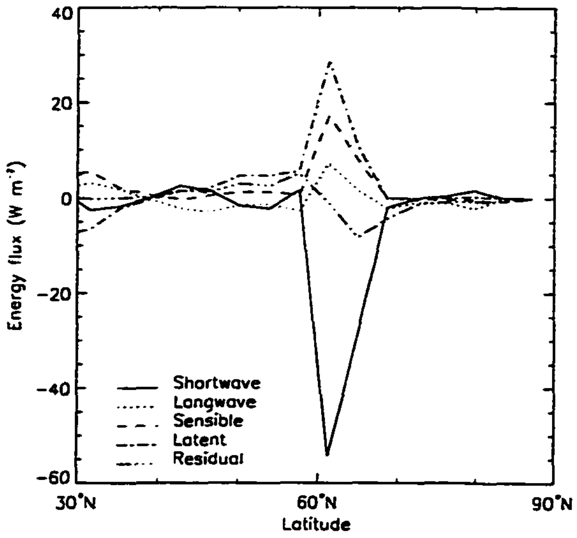

Figure 6.14: **Difference between E6 and E4 in summer energy budget at the land surface (W m^{-2}). Positive values represent net gain of energy for the surface while negative values represent net loss of energy for the surface. Data are extracted between 60°W and 120°W and then zonally-averaged.**

6.4 Discussion

Two mechanisms responsible for the decrease in snow melting due to 116 kaBP "cooler" sea surface conditions can be considered. The first mechanism is that colder SATs over land, caused by colder sea surface conditions, increase the net upward sensible heat flux at the surface, and reduce the energy available for the melting of snow. The second mechanism is that the colder SATs increase snowfall through increasing the fraction of snow in the total precipitation (especially in fall and spring — Fig. 6.8a), resulting in a longer snow cover season, an increase in surface albedo and a reduction in the energy available for snow melting. It is not, however, easy to discern the relative importance of the two mechanisms from these equilibrium experiments. Therefore, even though snow melting is a more important contribution to the annual snow budget difference at equilibrium, changes in snowfall could be important for the occurrence of a perennial snow cover. Consequently, the large increase in snowfall during fall and spring rather than winter and summer suggests the importance of SAT during these transition seasons for the occurrence of a perennial snow cover.

Further iteration of the AGCM integration and changes in vegetation might produce further expansion of tundra even when the present-day sea surface conditions are applied. However, given that changes in SAT during summer due to changes in vegetation with present-day sea surface conditions are less than 1°C cooling (Fig. 6.7**a**), this scenario would be highly dependent on the specified threshold temperature for vegetation change. This may explain the reason why no perennial snow cover was seen in de Noblet et al. (1996), where observed present-day sea surface conditions were used to drive their biosphere coupled AGCM.

Results obtained in this study suggest that the initiation of permanent snow cover and the growth of ice sheets is favoured by colder sea surface conditions, consistent with Rind et al. (1989) and Dong and Valdes (1995). Also, the model predicts that snowfall decreases with warm (present-day) sea surface conditions even though precipitation increases (Figs. 6.8**a** and 6.8**b**). Therefore, the results do not support the ice age hypothesis of Ruddiman and McIntyre (1979; 1981) and Ruddiman et al. (1980) in which warm sea surface conditions are necessary to lead to glacial inception through increased precipitation due to the enhanced hydrological cycle and due to the increased thermal contrast between land and ocean to intensify the baroclinicity and hence storm activity under 116 kaBP orbital forcing.

It may be noteworthy that heat transport in the OGCM and that implied by the AGCM are not expected to be compatible, as demonstrated by Weaver and Hughes (1996). For this reason, fully coupled atmosphere-ocean GCMs tend to require flux adjustments to avoid climate drift, and hence the approach (two-stage GCMs) taken in this study has great advantage. Indeed, the CCCma GCMII was designed to be used with either specified SST or a mixed layer model with specified internal heat transport.

6.5 Conclusion

To explore the effect of sea surface conditions on the last glacial inception, two 116 kaBP experiments were conducted: one with the present-day sea surface conditions and the other with 116 kaBP sea surface conditions. Perennial snow cover, considered as a minimum requirement for glacial inception, occurred over Canadian Archipelago under 116 kaBP orbital and CO_2 forcing, and further expanded over northeastern Canada when 116 kaBP sea surface conditions were applied. At equilibrium, snow melting dominated over snowfall and sublimation in the annual snow budget differences.

To explore the combined effect of the sea and land surface conditions, two additional 116 kaBP experiments were conducted: one with the present-day sea surface and modified land surface conditions and the other with 116 kaBP sea surface and modified land surface conditions. The modification of the land surface was carried out based on the climate from the previous experiments. When present-day sea surface conditions were applied to the 116 kaBP experiment, the climate did not change enough to cause much expansion of tundra based on the simple criteria employed in this study. On the other hand, when the 116 kaBP sea surface conditions were applied, significant cooling caused large expansion of tundra north of 60°N, which in turn produced further expansion of perennial snow cover over northern Canada. Perennial snow cover occurred over Scandinavia is well in agreement with paleo-reconstruction, but the control climate of this area is too cold, thereby allowing for a bias in this region.

This study verified the importance of sea surface conditions in paleoclimate modelling both for simulations and sensitivity analyses. This study also supports the notion that changes in vegetation should be taken into account (Gallimore and Kutzbach 1996; de Noblet et al. 1996). However, interactive coupling with a detailed biosphere model would be necessary to address this issue further. Results obtained in this study also demonstrate the ability of the CCCma AGCM to capture perennial snow cover over most of the areas known to have been important for glacial inception at 116 kaBP. To further examine the growth of ice sheets over the desired perennial snow cover areas at the desired speed, it is necessary to interactively couple the AGCM to a dynamic ice sheet model. At the same time, it is important to keep in mind that any biases in the present-day reference climate could play an important role in the study of ice sheet/snow mass balance.

Taken together, contrary to the earlier ice age hypothesis, the present analysis suggests that the capturing of glacial inception at 116 kaBP in AGCMs requires the use of "cooler" sea surface conditions than the present as a necessary condition. Without the inclusion of the "cooler" sea surface conditions, changes in vegetation are not enough to nucleate permanent snow cover. Combining "cooler" sea surface conditions with changes in vegetation lead to permanent snow cover over large regions in the AGCM used in this study.

Chapter 7

Conclusion

It has been well established that variations in the Earth's orbital geometry are the origin of the glacial-interglacial cycles. As represented by the 100 ka problem, the mechanism that links the insolation input to the geological output in the Earth's climate system, however, has not been completely understood. Paleoclimate proxy records strongly suggest the importance of changes in ocean circulation, particularly in the North Atlantic thermohaline circulation. Nevertheless, no studies have been conducted to investigate the interaction between ocean circulation and ice sheets using a non-zonal, coupled atmosphere-ocean-ice sheet model. Particular time periods such as 21 kaBP (LGM) and 6 kaBP (Holocene climatic optimum, hypthermal period) have been utilised to test the validity of the climate models under perpetual forcing. Climate at 116 kaBP (last glacial inception) has also been examined in detail. In such validation processes, the inclusion of the most important climate system components into a model is crucial. In this thesis, two rapid climatic transitions during the last glacial cycle, were studied: glacial termination and glacial inception. Emphasis was given to the ocean's role in these transitions as well as the interaction between the climate system components, and potentially important yet little explored precesses. The coupled climate (atmosphere-ocean-sea ice) model, the dynamical ice sheet model, and the CCCma AGCM were flexibly used depending on the specific objective of each chapter.

The response of thermohaline circualtion to changes in atmospheric CO_2 concentration and orbital geometry, during the last deglaciation, was investigated using the coupled climate model. It was shown that the thermohaline circulation can be greatly affected by both CO_2 and orbital forcing within a range of values during the last glacial cycle. The increase of the atmospheric CO_2 concentration from 200 ppmv to 280 ppmv which occurred during the last deglaciation, lead to a meridional temperature gradient between the ice-free ocean in lower latitudes and the ice-covered ocean in higher latitudes. This resulted in a strengthening the Atlantic meridional overturning. As the meridional overturning rate, and hence northward ocean heat transport increased, the freshwater flux at the sea surface in the northern North Atlantic decreased through changes in the formation, advection, and melting rates of sea ice. This mechanism works as a positive feedback, and further strengthens the meridional overturning. On the the hand, the change in orbital precession which also occurred during the last deglaciation, seasonally re-distributed the incoming solar radiation at the top of the atmosphere without changing the annual mean insolation at any given latitude. With seasonally-varying planetary albedo, however, this results in a latitudinal re-distribution of incoming solar radiation at the surface, thereby developing a hemispheric temperature gradient in the ocean, and consequently a change in atmospheric moisture transport. The moisture change in turn develops hemispheric salinity gradient in the ocean, resulting in a strengthening of the Atlantic meridional overturning. As is the case for CO_2 forcing, a similar positive feedback associated with sea ice further strengthens the meridional overturning. These results comprehensively reveal the response of the thermohaline to CO_2 and orbital forcing during the last glacial cycle. The results also suggest that the interactive calculation of planetary (cloud) albedo, rather than the specification of a planetary albedo fixed to the calendar date, is desirable for paleoclimate modelling.

An ice sheet model was then globally and asynchronously coupled to the climate model. The coupled climate-ice sheet model performed well under present-day, 11 kaBP and 21 kaBP perpetual forcing. The response of ice sheets to changes in atmospheric CO_2 concentration and orbital geometry during the last deglaciation was investigated using this coupled climate-ice sheet model. It was shown that, although both orbital and CO_2 forcing have an impact on ice sheet maintenance and deglacial processes, and although neither acting alone is sufficient to lead to complete deglaciation, orbital forcing is more important. The increase of atmospheric CO_2 concentration from 200 ppmv to 280 ppmv, as occurred during the last deglacition, had a large impact on climate, not uniformly or zonally over the globe, but concentrated in the North Atlantic and adjacent continents. The effect of CO_2 forcing on SAT had its peak there in winter associated with a reduction in sea ice extent in the northern North Atlantic. These changes were accompanied by an increased meridional overturning rate and northward ocean heat transport in the Atlantic. On the other hand, the changes in orbital configuration, as occurred during the last deglaciation, had a large impact on the climate over the NH continents. The effect of orbital forcing on SAT had its peak in summer. Since the summer temperature, rather than winter temperature, was found to be dominant for the ice sheet mass balance, orbital forcing had a larger effect than CO_2 forcing in deglaciation. The precipitation effect is totally overwhelmed by the temperature effect. These results suggest that the last deglaciation was initiated through increasing summer insolation with CO_2 providing a powerful feedback.

The importance of unresolved subgrid-scale topography in simulations of the last glacial inception was also investigated using the coupled climate model. Two different approaches were taken. In the first approach, each cell was divided into many subcells and the SAT was calculated using a constant lapse rate. This approach allowed for the mechanism that perennial snow cover starts on subgrid-scale high elevation areas, followed by local cooling through the albedo feedback, and subsequent cooling of the surrounding low elevation areas that causes perennial snow cover there. In the second approach, subgrid-scale ice-flow was parameterised and hence allowed for the mechanism that glacial inception expanded due to ice-flow and a direct local albedo feedback, rather than through the diffusion of heat from high elevation areas to low elevation areas. It was shown that the inclusion of subgrid elevation improved the distribution of ice in the present-day simulation, and a recognisable expansion of perennial snow cover was observed in northwestern Canada and Baffin Island under 116 kaBP forcing. It was also shown, however, that the inclusion of subgrid ice-flow did not further lead to a large scale glacial inception. In both cases, no perennial snow cover occurred in Keewatin and Labrador, where glacial inception is suggested by geological evidence. These results suggest that the coupled climate model fails to capture the last glacial inception, and unresolved subgrid-scale topography is of secondary importance to large scale climatology.

The response of an AGCM to changes in lower boundary conditions was investigated to explore processes involved in glacial inception at 116 kaBP. Two 116 kaBP experiments were conducted to examine the importance of sea surface conditions (SST and sea ice distribution): one with the present-day sea surface conditions, and the other with 116 kaBP sea surface conditions. These two different sea surface conditions were obtained from coupled climate model simulations. Perennial snow cover occurred over the Canadian Archipelago under 116 kaBP orbital and CO_2 forcing with present-day "warm" sea surface conditions, and further expanded over northeastern Canada when 116 kaBP "cold" sea surface conditions were applied. The net positive accumulation in northeastern Canada, with little net accumulation in Alaska, is in good agreement with geological records. Two additional 116 kaBP experiments were conducted to examine the combined importance of sea surface conditions and land surface conditions (vegetation): one with the present-day sea surface and modified land surface conditions, and the other with 116 kaBP sea surface and modified land surface conditions. Modifying vegetation, based on cooling during summer induced by 116 kaBP sea surface conditions, lead to much larger areas of perennial snow cover. Only when 116 kaBP sea surface conditions were applied, is a realistic global net snow accumulation rate obtained. Contrary to the earlier ice age hypothesis, the results suggest that the capturing of glacial inception at 116 kaBP requires the use of "colder" sea surface conditions than those of the present climate. Also, the large impact of vegetation change on climate suggests that the inclusion of the vegetation feedback is important for model validation, at least, in this particular period of the Earth history.

In this thesis, the focus was upon the interaction between climate system components: atmosphere, ocean, sea ice, ice sheet, and biosphere. The different characteristics of the temporal and spatial scales of each component creates a challenge for paleoclimate modelling. In addition, the use of fully coupled atmosphere-ocean GCMs in paleoclimate applications is still premature and limits modelling studies. Furthermore, paleoclimate modelling often forces the tackling of two fundamentally different goals at the same time: 1) solving the mystery of climate within paleo-reconstructions; and 2) validating the model. To overcome such difficulties, however, unique approaches were taken in this thesis. It was seen that the Earth's climate acted in the past as a system with complicated interactions between subsystems. Therefore, the development and application of a more comprehensive Earth system climate model in the future would be useful. Given that the ocean played an important role during the last glacial cycle, fully coupled atmosphere-ocean GCMs have the highest priority among these.

This thesis suggests that increase in the atmospheric CO_2 concentration during the last glacial termination played an important role in promoting deglacial processes. This thesis also suggests that changes in ocean conditions and vegetation during the last glacial inception played an fundamental role in promoting glacial processes. Taken together, the glacial-interglacial transitions, during the last glacial cycle, were initiated by changes in orbital configuration and greatly aided by the subsequent changes in internal climate system components.

Bibliography

Alexander R.C. and Mobley R.L. (1976) Monthly average sea-surface temperatures and ice-pack limits on a 1° global grid. *Mon. Wea. Rev.*, 104(2):143–148.

Alley R.B. (1989) Water-pressure coupling of sliding and bed deformation II: Velocity-depth profiles. *J. Glaciol*, 35:119–129.

Alley R.B. and Clark P.U. (1999) The deglaciation of the Northern Hemisphere: A global perspective. *Ann. Rev. Earth Planet. Sci.*, 27:149–182.

Alley R.B., Clark P.U., Keigwin L.D., and Webb R.S. (1999) Making sense of millennial-scale climate change. In P.U. Clark, R.S. Webb, and L.D. Keigwin, eds., *Mechanisms of Global Climate Change at Millennial Time Scales*, vol. 112 of *Geophysical Monograph*, pages 385–394. American Geophysical Union, Washington, DC.

Anderson T.L. and Charlson R.J. (1990) Ice-age dust and salt. *Nature*, 345:393.

Andrews J.T. (1982) On the reconstruction of Pleistocene ice sheets: A review. *Quat. Sci. Rev.*, 1:1–30.

Andrews J.T. (1997) Northern Hemisphere (Laurentide) deglaciation: Processes and responses of ice sheet/ocean interactions. In I.P. Martini, ed., *Late Glacial and Postglacial Environmental Changes: Quaternary, Carboniferous-Permian, and Proterozoic*, pages 9–27. Oxford University Press, New York, NY.

Archer D., Winguth A., Lea D., and Mahowald N. (2000) What caused the glacial/interglacial atmospheric $p\mathrm{CO}_2$ cycles? *Rev. Geophys.*, 38(2):159–189.

Bard E. (1999) Ice age temperatures and geochemistry. *Science*, 284(5417):1133–1134.

Barnola J.M., Raynaud D., Korotkevich Y.S., and Lorius C. (1987) Vostok ice core provides 160,000-year record of atmospheric CO_2. *Nature*, 329:408–414.

Barron E.J. (1985) Explanation of the Tertiary global cooling trend. *Plaeogeogr. Palaeoclim. Palaeoecol.*, 50:45–61.

Barron J., Larsen B., and Baldauf J.G. (1991) Evidence for late Eocene to early Oligocene Antarctic glaciation and observations on late Neogene glacial history of Antarctica: Results from leg 119. *Proceedings of the Ocean Drilling Program, Scientific Resutls*, 119:869–891. Kerguelen Plateau - Prydz Bay (14 December 1987 - 20 February 1988).

Bender M., Sowers T., and Labeyrie L. (1994) The Dole effect and its variations during the last 130,000 years as measured in the Vostok ice core. *Global Biogeochem. Cycles*, 8(3):363–376.

Berger A. (1978) Long-term variations of daily insolation and Quaternary climatic changes. *J. Atmos. Sci.*, 35(12):2362–2367.

Berger A. (1988) Milankovitch theory and climate. *Rev. Geophys.*, 26(4):624–657.

Berger A. (1996) Orbital parameters and equations. In S.H. Schneider, ed., *Encyclopedia of Climate and Weather*, vol. 2, pages 552–557. Oxford University Press, New York, NY.

Berger A. and Loutre M.F. (1991) Insolation values for the climate of the last 10 million years. *Quat. Sci. Rev.*, 10:297–317.

Berger A., Melice J.L., and Hinnov L. (1991) A strategy for frequency spectra of Quaternary climate records. *Clim. Dyn.*, 5(4):227–240.

Berggren W.A. (1972) Late Pliocene-Pleistocene glaciation. In A.S. Laughton, W.A. Berggren, et al., eds., *Initial Reports of the Deep Sea Drilling Project*, vol. 12, pages 953–963. U.S. Government Printing Office, Washington D.C.

Bigg G.R., Wadley M.R., Stevens D.P., and Johnson J.A. (1998) Simulations of two last glacial maximum ocean states. *Paleoceanogr.*, 13(4):340–351.

Birchfield G.E. (1977) A study of the stability of a model continental ice sheet subject to periodic variations in heat input. *J. Geophys. Res.*, 82(31):4909–4913.

Birchfield G.E., Weertman J., and Lunde A.T. (1981) A paleoclimate model of Northern Hemisphere ice sheets. *Quat. Res.*, 15:126–142.

Birchfield G.E., Weertman J., and Lunde A.T. (1982) A model study of the role of high-latitude topography in the climatic response to orbital insolation anomalies. *J. Atmos. Sci.*, 39(1):71–87.

Bolton D. (1980) The computation of equivalent potential temperature. *Mon. Wea. Rev.*, 108:1046–1053.

Bolton E.W., Maasch K.A., and Lilly J.M. (1995) A wavelet analysis of Plio-Pleistocene climate indicators: A new view of periodicity evolution. *Geophys. Res. Let.*, 22(20):2753–2756.

Bond G., Broecker W., Johnsen S., McManus J., Labeyrie L., Jouzel J., and Bonani G. (1993) Correlations between climate records from North Atlantic sediments and Greenland ice. *Nature*, 365:143–147.

Boyle E.A. and Keigwin L. (1987) North Atlantic thermohalice circulation during the past 20,000 years linked to high-latitude surface temperature. *Nature*, 330:35–40.

Boyle E.A. and Keigwin L.D. (1982) Deep circulation of the North Atlantic over the last 200,000 years: Geochemical evidence. *Science*, 218:784–787.

Boyle E.D. (1995) Last-Glacial-Maximum North Atlantic Deep Water: On, off or somewhere in-between? *Philosophical Transactions of the Royal Society of London*, 347:243–253. Series B Biological Sciences.

Bradley R.S. (1999) *Paleoclimatology: Reconstructing Climates of the Quaternary*, vol. 64 of *International Geophysical Series*. Academic Press, San Diego, CA, second edn. 613pp.

Brickman D., Hyde W., and Wright D.G. (1999) Filtering of Milankovitch cycles by the thermohaline circulation. *J. Clim.*, 12(6):1644–1658.

Broccoli A.J. and Manabe S. (1987) The influence of continental ice, atmospheric CO_2, and land albedo on the climate of the last glacial maximum. *Clim. Dyn.*, 1(2):87–99.

Broecker W.S. (1985) *How to Build a Habitable Planet*. Lamont-Doherty Geological Observatory of Columbia University, Palisades, NY. 291pp.

Broecker W.S. (1989) Some thoughts about the radiocarbon budget for the glacial Atlantic. *Paleoceanography*, 4(2):213–220.

Broecker W.S. (1991) The great ocean conveyor. *Oceanography*, 4(2):79–89.

Broecker W.S. and Denton G.H. (1989) The role of ocean-atmosphere reorganizations in glacial cycles. *Geochim. Cosmo. Acta*, 53:2465–2501.

Broecker W.S. and Henderson G.M. (1998) The sequence of events surrounding termination II and their implications for the cause of glacial-interglacial CO_2 changes. *Paleoceanogr.*, 13(4):352–364.

Broecker W.S., Kennett J.P., Flower B.P., Teller J.T., Trumbore S., Bonani G., and Molfli W. (1989) Routing of meltwater from the Laurentide ice sheet during the Younger Dryas cold episode. *Nature*, 341:318–321.

Broecker W.S. and Peng T.H. (1993) What caused the glacial to interglacial CO_2 change? In M. Heimann, ed., *The Global Carbon Cycle*, vol. 15, pages 95–115. Springer-Verlag, Heidelberg.

Broecker W.S., Peteet D.M., and Rind D. (1985) Does the ocean-atmosphere system have more than one stable mode of operation? *Nature*, 315(6014):21–26.

Bryan K. and Lewis L.J. (1979) A water mass model of the world ocean. *J. Geophys. Res.*, 84(C5):2503–2517.

Bryden H.L. (1993) Ocean heat transport across 24° latitude. In *Interactions Between Global Climate Subsystems*, vol. IUGG 15 of *Geophysical Monograph 75*, pages 65–75. International Union of Geodesy and Geophysics and the American Geophysical Union.

Budd W.F. and Smith I.N. (1981) The growth and retreat of ice sheets in response to orbital radiation changes. *IAHS Publ.*, 131:369–409.

Budyko M.I. (1969) The effect of solar radiation variations on the climate of the Earth. *Tellus*, 21:611–619.

Bush A.B.G. and Philander S.G.H. (1998) The role of ocean-atmosphere interactions in tropical cooling during the last glacial maximum. *Science*, 279(5355):1341–1344.

Clark P.U., Clague J.J., Curry B.B., Dreimanis A., Hicock S.R., Miller G.H., Berger G.W., Eyles N., Lamothe M., Miller B.B., Mott R.J., Oldale R.N., Stea R.R., Szabo J.P., Thorleifson L.H., and Vincent J.S. (1993) Initiation and development of the Laurentide and Cordilleran ice sheets following the last interglaciation. *Quat. Sci. Rev.*, 12:79–114.

Clark P.U. and Pollard D. (1998) Origin of the middle Pleistocene transition by ice sheet erosion of regoligh. *Paleoceanogr.*, 13(1):1–9.

Clarke G.K.C., Marshall S.J., Hillaire-Marcel C., Bilodeau G., and Veiga-Pires C. (1999) A glaciological perspective on Heinrich events. In P.U. Clark, R.S. Webb, and L.D. Keigwin, eds., *Mechanisms of Global Climate Change at Millennial Time Scales*, vol. 112 of *Geophysical Monograph*, pages 243–262. American Geophysical Union, Washington, DC.

CLIMAP (1981) *Seasonal Reconstructions of the Earth's Surface at the Last Glacial Maximum*. Map Chart Series, MC-36. Geological Society of America, Boulder, CO.

Colin de Verdiére A. (1993) On the oceanic thermohaline circulation. In J. Willebrand and D.L.T. Anderson, eds., *Modelling Oceanic Climate Interactions*, vol. I11 of *NATO ASI Series*, pages 151–183. Springer-Verlag, Berlin, Heidelberg.

Cronin T.M. (1999) *Principles of Paleoclimatology*. Perspectives in Paleobiology and Earth History Series. Columbia University Press, New York, NY. 560pp.

Crowley T.J. (1992) North Atlantic deep water cools Southern Hemisphere. *Paleoceanography*, 7(4):489–497.

Crowley T.J. and Häkkinen S. (1998) A new mechanism for decreasing North Atlantic Deep Water production rates during the Pleistocene. *Paleoceanogr.*, 3(3):249–258.

Crowley T.J. and North G.R. (1991) *Paleoclimatology*, vol. 18 of *Oxford Monograph on Geology and Geophysics*. Oxford University Press, New York, NY. 349pp.

Cuffey K.M. and Marshall S.J. (2000) Substantial contribution to sea-level rise during the last interglacial from the Greenland ice sheet. *Nature*, 404(6778):591–594.

Curry R.R. (1966) Glaciation about 3,000,000 years ago in the Sierra Nevada. *Science*, 154:770–771.

de Noblet N.I., Prentice I.C., Joussaume S., Texier D., Botta A., and Haxeltine A. (1996) Possible role of atmosphere-biosphere interactions in triggering the last glaciation. *Geophys. Res. Let.*, 23(22):3191–3194.

de Vernal A. and Hillaire-Marcel C. (2000) Sea-ice cover, sea-surface salinity and halo-/thermocline structure of the northwest North Atlantic: Modern versus full glacial conditions. *Quat. Sci. Rev.*, pages 65–85.

de Vernal A., Hillaire-Marcel C., Turon J.L., and Matthiessen J. (2000) Reconstruction of sea-surface temperature, salinity, and sea-ice cover in the northern North Atlantic during the last glacial maximum based on dinocyst assemblages. *Can. J. Earth Sci.*, 37:725–750.

Deardorff J.W. (1978) Efficient prediction of ground surface temperature and moisture, with inclusion of a layer of vegetation. *J. Geophys. Res.*, 83(C4):1889–1903.

Deblonde G. and Peltier W.R. (1990) A model of late Pleistocene ice sheet growth with realistic geography and simplified cryodynamics and geodynamics. *Clim. Dyn.*, 5(2):103–110.

Deblonde G. and Peltier W.R. (1991) Simulations of continental ice sheet growth over the last glacial-interglacial cycle: Experiments with a one-level seasonal energy balance model including realistic geography. *J. Geophys. Res.*, 96(D5):9189–9215.

Deblonde G. and Peltier W.R. (1993) Late Pleistocene ice age scenarios based on observational evidence. *J. Clim.*, 6(4):709–727.

Denton G.H. and Hughes T.J., eds. (1981) *The Last Great Ice Sheets*. John Wiley and Sons, New York, NY.

Dong B. and Valdes P.J. (1995) Sensitivity studies of Northern Hemisphere glaciation using an atmospheric general circulation model. *J. Clim.*, 8(10):2471–2496.

Donn W.L. and Ewing M. (1966) A theory of ice ages III. *Science*, 152(3730):1706–1712.

Duplessy J.C., Shackleton N.J., Fairbanks R.G., Labeyrie L., Oppo D., and Kallel N. (1988) Deepwater source variations during the last climatic cycle and their impact on the global deepwater circulation. *Paleoceanography*, 3(3):343–360.

East T.M., McCulloch M.T., Chappell J., Pillans B., and Omura A. (1999) Rapid fluctuations in sea level recorded at Huon Peninsula during the penultimate deglaciation. *Science*, 283(5399):197–201.

Edwards R.L. and Peltier W.R. (1995) Paleotopography of glacial-age ice sheets. *Science*, 267(5197):536–538.

Ehrmann W.U. and Mackensen A. (1992) Sedimentological evidence for the formation of an East Antarctic ice sheet in Eocone/Oligocene time. *Plaeogeogr. Palaeoclim. Palaeoecol.*, 93:85–112.

ETOPO5 (1988) Data announcement 88-mgg-02, digital relief of the surface of the earth. NOAA, National Geophysical Data Center, Boulder, CO.

Ewing M. and Donn W.L. (1956) A theory of ice ages. *Science*, 123(3207):1061–1066.

Ewing M. and Donn W.L. (1958) A theory of ice ages II. *Science*, 127(3307):1159–1162.

Fairbanks R.G. (1989) A 17,000-year glacio-eustatic sea level record: Influence of glacial melting rates on the Younger Dryas event and deep-ocean circulation. *Nature*, 342(6250):637–642.

Fanning A.F. and Weaver A.J. (1996) An atmospheric energy-moisture balance model: Climatology, interpentadal climate change, and coupling to an ocean general circulation model. *J. Geophys. Res.*, 101(D10):15111–15128.

Fanning A.F. and Weaver A.J. (1997a) A horizontal resolution and parameter sensitivity study of heat transport in an idealized coupled climate model. *J. Clim.*, 10(10):2469–2478.

Fanning A.F. and Weaver A.J. (1997b) On the role of flux adjustments in an idealized coupled climate model. *Clim. Dyn.*, 13(10):691–701.

Fichefet T., Hovine S., and Duplessy J.C. (1994) A model study of the Atlantic thermohaline circulation during the last glacial maximum. *Nature*, 372(6503):252–255.

Flint R.F. (1971) *Glacial and Quaternary Geology*. John Wiley and Sons, New York, NY.

Fouquart Y. and Bonnel B. (1980) Computations of solar heating of the earth's atmosphere: A new parameterization. *Beitr. Phys.*, 53(1):35–62.

Gallée H., van Ypersele J.P., Fichefet T., Ch C.T., and Berger A. (1991) Simulation of the last glacial cycle by a coupled, sectorially averaged climate-ice sheet model 1. the climate model. *J. Geophys. Res.*, 96(D7):13139–13161.

Gallée H., van Ypersele J.P., Fichefet T., Marsiat I., Tricot C., and Berger A. (1992) Simulation of the last glacial cycle by a coupled, sectorially averaged climate-ice sheet model 2. response to insolation and CO_2 variations. *J. Geophys. Res.*, 97(D14):15713–15740.

Gallimore R.G. and Kutzbach J.E. (1995) Snow cover and sea ice sensitivity to generic changes in earth orbital parameters. *J. Geophys. Res.*, 100(D1):1103–1120.

Gallimore R.G. and Kutzbach J.E. (1996) Role of orbitally induced changes in tundra area in the onset of glaciation. *Nature*, 381(6582):503–505.

Ganopolski A., Rahmstorf S., Petoukhov V., and Claussen M. (1998) Simulation of modern and glacial climates with a coupled global model of intermediate complexity. *Nature*, 391(6665):351–356.

Gill A.E. (1982) *Atmosphere-Ocean Dynamics*, vol. 30 of *International Geophysics Series*. Academic Press, New York, NY.

Glen J.W. (1955) The creep of polycrystalline ice. *Proc R Soc London Ser A*, 228:519–538.

Glen J.W. (1958) The flow law of ice: A discussion of the assumptions made in glacier theory, their experimental foundations and consequences. *IASH*, 47:171–183.

Glickman T.S., ed. (2000) *Glossary of Meteorology*. American Meteorological Society, second edn.

GLOBE1.0 (2001) Global land one-kilometer base elevation digital elevation data: Globe dem version 1.0. Http://www.ngdc.noaa.gov/seg/fliers/globedem.shtml.

Godfrey J.S. (1989) A Sverdrup model of the depth-integrated flow for the world ocean allowing for island circulations. *Geophys. Astrophys. Fluid Dynamics*, 45:89–112.

Gordon A.L. (1986) Interocean exchange of thermocline water. *J. Geophys. Res.*, 91(C4):5037–5046.

Graves C.E., Lee W.H., and North G.R. (1993) New parameterizations and sensitivities for simple climate models. *J. Geophys. Res.*, 98(D3):5025–5036.

Guilderson T.P., Fairbanks R.G., and Rubenstone J.L. (1994) Tropical temperature variations since 20,000 years ago: Modulating interhemispheric climate change. *Science*, 263(5147):663–665.

Hall M.N.J., Valdes P.J., and Dong B. (1996) The maintenance of the last great ice sheets: A UGAMP GCM study. *J. Clim.*, 9(5):1004–1019.

Hansen J., Lacis A., Rind D., Russel G., Stone P., Fung I., Ruedy R., and Lerner J. (1984) Climate sensitivity: analysis of feedback mechanisms. In J. Hansen and T. Takahashi, eds., *Climate processes and climate sensitivity.*, pages 130–163. American Geophysical Union.

Harland W.B., Armstrong R.L., Cox A.V., Craig L.E., Smith A.G., and Smith D.G. (1990) *A Geologic Time Scale 1989*. Cambridge University Press, New York, NY. 263pp.

Harrison S.P., Kutzbach J.E., Prentice I.C., Behling P.J., and Sykes M.T. (1995) The response of Northern Hemisphere extratropical climate and vegetation to orbitaly induced changes in insolation during the last interglaciation. *Quat. Res.*, 43(2):174–184.

Harvey L.D.D. (1988) Climatic impact of ice-age aerosols. *Nature*, 334:333–335.

Hays J.D., Imbrie J., and Shackleton N.J. (1976) Variations in the earth's orbit: Pacemaker of the ice ages. *Science*, 194(4720):1121–1132.

Henderson G.M. and Slowey N.C. (2000) Evidence from U-Th dating against Northern Hemisphere forcing of the penultimate deglaciation. *Nature*, 404(6773):61–66.

Hewitt C.D., Broccoli A.J., Mitchell J.F.B., and Stouffer R.J. (2001) A coupled model study of the last glacial maximum: Was part of the North Atlantic relatively warm? *Geophys. Res. Let.*, 28(8):1571–1574.

Hibler I.W.D. (1979) A dynamic thermodynamic sea ice model. *J. Phys. Oceanogr.*, 9(4):815–846.

Hooke R.L. (1998) *Principles of Glacier Mechanics.* Prentice Hall, Upper Saddle River, NJ. 248pp.

Hostetler S.W. and Mix A.C. (1999) Reassessment of ice-age cooling of the tropical ocean and atmosphere. *Nature*, 399(6737):673–676.

Howard W.R. (1997) A warm future in the past. *Nature*, 388(6641):418–419.

Hughes T.M.C. and Weaver A.J. (1994) Multiple equilibria of an asymmetric two-basin ocean model. *J. Phys. Oceanogr.*, 24(3):619–637.

Hunke E.C. and Dukowicz J.K. (1997) An elastic-viscous-plastic model for sea ice dynamics. *J. Phys. Oceanogr.*, 27(9):1849–1867.

Hyde W.T. and Peltier W.R. (1985) Sensitivity experiments with a model of the ice age cycles: The response to harmonic forcing. *J. Atmos. Sci.*, 42(20):2170–2188.

Hyde W.T. and Peltier W.R. (1987) Sensitivity experiments with a model of the ice age cycles: The response to Milankovitch forcing. *J. Atmos. Sci.*, 44(10):1351–1374.

Imbrie J., Berger A., Boyle E.A., Clemens S.C., Duffy A., Howard W.R., Kukla G., Kutzbach J., Martinson D.G., McIntyre A., Mix A.C., Molfino B., Morley J.J., Peterson L.C., Pisias N.G., Prell W.L., Raymo M.E., Shackleton N.J., and Toggweiler J.R. (1993) On the structure and origin of major glaciation cycles: 2. the 100,000-year cycle. *Paleoceanogr.*, 8(6):699–735.

Imbrie J., Boyle E.A., Clemens S.C., Duffy A., Howard W.R., Kukla G., Kutzbach J., Martinson D.G., McIntyre A., Mix A.C., Molfino B., Morley J.J., Peterson L.C., Pisias N.G., Prell W.L., Raymo M.E., Shackleton N.J., and Toggweiler J.R. (1992) On the structure and origin of major glaciation cycles: 1. linear responses to Milankovitch forcing. *Paleoceanogr.*, 7(6):701–738.

Imbrie J., Hays J.D., Martinson D.G., McIntyre A., Mix A.C., Morley J.J., Pisias N.G., Prell W.L., and Shackleton N.J. (1984) The orbital theory of Pleistocene climate: Support from a revised chronology of the marine δ^{18}O record. In A.L. Berger, J. Hays, G. Kukla, and B. Salzman, eds., *Milankovitch and Climate, Part 1*, pages 269–305. D. Reidel Publishing Company, Dordrecht, Holland.

Imbrie J. and Imbrie J.Z. (1980) Modeling the climatic response to orbital variations. *Science*, 207(4434):943–953.

Imbrie J. and Imbrie K.P. (1979) *Ice Ages: Solving the Mystery*. Harvard University Press, Cambridge, MA. 224pp.

Isemer H.J., Willbrand J., and Hasse L. (1989) Fine adjustment of large scale air-sea energy flux parameterizations by direct estimates of ocean heat transport. *J. Clim.*, 2(10):1173–1184.

Ives J.D., Andrews J.T., and Barry R.G. (1975) Growth and decay of the Laurentide Ice Sheet and comparisons with Fenno-Scandinavia. *Naturwissenschaften*, 62:118–125.

Jansen E. and Sjøholm J. (1991) Reconstruction of glaciation over the past 6 myr from ice-borne deposits in the Norwegian Sea. *Nature*, 349(6310):600–603.

Jansen E., Sjøholm J., Bleil U., and Ericksen J.A. (1990) Neogene and Pleistocene glaciation in the Northern Hemisphere and late Miocene-Pliocene global ice volume fluctuations: Evidence from the Norwegian Sea. In U. Bleil and J. Thiede, eds., *Geological History of the Polar Oceans: Arctic versus Antarctic*, pages 677–705. Kluwer, Netherlands.

Jouzel J., Barkov N.I., Barnola J.M., Bender M., Chappelaz J., Genthon C., Kotlyakov V.M., Lipenkov V., Lorius C., Petit J.R., Raynaud D., Raisbeck G., Ritz C., Sowers T., Stievenard M., Yiou F., and Yiou P. (1993) Extending the Vostok ice-core record of palaeoclimate to the penultimate glacial period. *Nature*, 364:407–412.

Kageyama M., Valdes P.J., Ramstein G., Hewitt C., and Wyputta U. (1999) Northern Hemisphere strom tracks in present day and last glacial maximum climate simulations: A comparison of the European PMIP models. *J. Clim.*, 12(3):742–760.

Kalnay E., Kanamitsu M., Kistler R., Collins W., Deaven D., Gandin L., Iredell M., Saha S., White G., Woolen J., Zhu Y., Leetmaa A., and Reynolds R. (1996) The NCEP/NCAR 40 years reanalysis project. *Bull. Amer. Meteor. Soc.*, 77:437–471.

Keffer T., Martinson D.G., and Corliss B.H. (1988) The position of the Gulf Stream during Quaternary glaciations. *Science*, 241(4864):440–442.

Keigwin L.D.J. and Thunell R.C. (1979) Middle Pliocene climate change in the western Mediterranean from faunal and oxygen isotopic trends. *Nature*, 282:294–296.

Kennett J.P. (1977) Cenozoic evolution of Antarctic glaciation, the Circum-Antarctic ocean and their impact on global paleoceanography. *Journal of Geophysical Research*, 82(27):3843–3860.

Kennett J.P. (1982) *Marine Geology*. Prentice-Hall.

Khodri M., Leclainche Y., Ramstein G., Braconnot P., Marti O., and Cortijo E. (2001) Simulating the amplification of orbital forcing by ocean feedbacks in the last glaciation. *Nature*, 410(6828):570–574.

Killworth P.D. (1983) Deep convection in the world ocean. *Rev. Geophys. Space Phys.*, 21(1):1–26.

Kitoh A., Murakami S., and Koide H. (2001) A simulation of the last glacial maximum with a coupled atmosphere-ocean gcm. *Geophys. Res. Let.*, 28(11):2221–2224.

Kuhle M. (1987a) Geomorphological findings on the build-up of Pleistocene glaciation in southern Tibet and on the problem of inland ice - results of the Shisha Pangma and Mt. Everest expedition 1984. *GeoJournal*, 17:457–511.

Kuhle M. (1987b) Subtropical mountain- and highland-glaciation as Ice Age triggers and the waning of the glacial periods in the Pleistocene. *GeoJournal*, 14(4):393–421.

Kuhle M. (1988) The Pleistocene glaciations of the Tibet and the onset of ice ages - an autocycle hypothesis. *GeoJournal*, 17(4):581–595.

Kukla G. (1980) End of the last interglacial: A predictive model of the future? In E.M. Van Zinderen Bakker Sr and J.A. Coetzee, eds., *Paleoecology of Africa and the Surrounding Islands*, pages 395–408. Balkema Publishers, Rotterdam.

Kundu P.K. (1990) *Fluid Mechanics*. Academic Press, San Diego, CA. Pp.638.

Laprise R. and Girard C. (1990) A spectral general circulation model using a piecewise-constant finite-element representation on a hybrid vertical coordinate system. *J. Clim.*, 3(1):32–52.

Larsen H.C., Saunders A.D., Clift P.D., Beget J., Wei W., Spezzaferri S., and ODP Leg 152 Scientific Party (1994) Seven million years of glaciation in Greenland. *Science*, 264(5161):952–955.

Lautenschlager M., Mikolajewicz U., Maier-Reimer E., and Heinze C. (1992) Application of ocean models for the interpretation of atmospheric general circulation model experiments on the climate of the last glacial maximum. *Paleoceanogr.*, 7(6):769–782.

Lear C.H., Elderfield H., and Wilson P.A. (2000) Cenozoic deep-sea temperature and global ice volumes from Mg/Ca in benthic foraminiferal calcite. *Science*, 287(5451):269–272.

Licciarde J.M., Teller J.T., and Clark P.U. (1999) Freshwater routing by the Laurentide Ice Sheet during the last deglaciation. In P.U. Clark, R.S. Webb, and L.D. Keigwin, eds., *Mechanisms of Global Climate Change at Millennial Time Scales*, vol. 112 of *Geophysical Monograph*, pages 177–201. American Geophysical Union, Washington, DC.

Linsley B.K. (1996) Oxygen-isotope record of sea level and climate variations in the Sulu Sea over the past 150,000 years. *Nature*, 380(6571):234–237.

Liu H.S. and Chao B.F. (1998) Wavelet spectral analysis of the earth's orbital variations and paleoclimatic cycles. *J. Atmos. Sci.*, 55(2):227–236.

Lowell T.V., Heusser C.J., Anderson B.G., Moreno P.I., Hauser A., Heusser L.E., Schlüchter C., Marchant D.R., and Denton G.H. (1995) Interhemispheric correlation of late pleistocene glacial events. *Science*, 269(5230):1541–1549.

Lynch-Stieglitz J., Curry W.B., and Slowey N. (1999) Weaker Gulf Stream in the Florida Straits during the last glacial maximum. *Nature*, 402(6762):644–648.

Manabe S. (1989) Studies of glacial climates by coupled atmosphere-ocean models: How useful are coupled models? In R.S. Bradley, ed., *Global Changes of the Past*, pages 421–448. UCAR/Office for Interdisciplinary Earth Studies, Boulder, CO.

Manabe S. and Broccoli A.J. (1985) The influence of continental ice sheets on the climate of an ice age. *J. Geophys. Res.*, 90(D1):2167–2190.

Manabe S. and Stouffer R.J. (1988) Two stable equilibria of a coupled ocean-atmosphere model. *J. Clim.*, 1(9):841–866.

Marotzke J. (1996) Analysis of thermohaline feedbacks. In D.L.T. Anderson and J. Willebrand, eds., *Decadal Climate Variability: Dynamics and Predictability*, vol. I 44 of *NATO ASI Series*, pages 333–378. Springer-Verlag, Berlin Heidelberg.

Marotzke J. and Scott J.R. (1999) Convective mixing and the thermohaline circulation. *J. Phys. Oceanogr.*, 29(11):2962–2970.

Marotzke J. and Stone P.H. (1995) Atmospheric transports, the thermohaline circulation, and flux adjustments in a simple coupled model. *J. Phys. Oceanogr.*, 25(6, Part I):1350–1364.

Marshall J. and Schott F. (1999) Open-ocean convection: Observations, theory, and models. *Rev. Geophys.*, 37(1):1–64.

Marshall S.J. (1996) *Modelling Laurentide Ice Stream Thermomechanics*. Ph.D. thesis, University of British Columbia, Vancouver, BC, Canada.

Marshall S.J. (1997) *UBC Ice Sheet Model Documentation*. Department of Earth and Ocean Sciences, University of British Columbia, Vancouver, BC, Canada. 51pp.

Marshall S.J. (1998) Dynamics of the Pleistocene ice sheet. In P.P. Wu, ed., *Dynamics of the Ice Age Earth: A Modern Perspective*, vol. 3 of *GeoResearch Forum Series*, pages 217–248. Trans Tech Publications, Zurich.

Marshall S.J. and Clarke G.K.C. (1997a) A continuum mixture model of ice stream thermomechanics in the Laurentide ice sheet, 1. theory. *J. Geophys. Res.*, 102(B9):20599–20614.

Marshall S.J. and Clarke G.K.C. (1997b) A continuum mixture model of ice stream thermomechanics in the Laurentide ice sheet, 2. application to the Hudson Strait ice stream. *J. Geophys. Res.*, 102(B9):20599–20614.

Marshall S.J. and Clarke G.K.C. (1999) Ice sheet inception: Subgrid hypsometric parameterization of mass balance in an ice sheet model. *Clim. Dyn.*, 15(7):533–550.

Marsiat I. and Valdes P.J. (2001) Sensitivity of the Northern Hemisphere climate of the Last Glacial Maximum to sea surface temperatures. *Clim. Dyn.*, 17(2-3):233–248.

Marsiat I.M. and Berger A. (1990) On the relationship between ice volume and sea level over the last glacial cycle. *Clim. Dyn.*, 4(2):81–84.

McDougall I. and Wensink H. (1966) Paleomagnetism and geochronology of the Pliocene-Pleistocene Lausas in Iceland. *Earth and Planetary Science Letters*, 1:232–236.

McFarlane N.A. (1987) The effect of orographically excited gravity wave drag on the general circulation of the lower stratosphere and troposphere. *J. Atmos. Sci.*, 44(14):1775–1800.

McFarlane N.A., Boer G.J., Blanchet J.P., and Lazare M. (1992) The Canadian Climate Centre second-generation general circulation model and its equilibrium climate. *J. Clim.*, 5(10):1013–1044.

McManus J.F., Bond G.C., Broecker W.S., Johnsen S., Labeyrie L., and Higgins S. (1994) High-resolution climate records from the North Atlantic during the last interglacial. *Nature*, 371(6495):326–329.

McPhee M.G. (1992) The turbulent heat flux in the upper ocean under sea ice. *J. Geophys. Res.*, 97(C4):5365–5379.

Milankovitch M. (1941) *Kanon der Erdbestrahlung und seine Anwendung auf das Eiszeitenproblem*, vol. 33, Spec. Pub. 132 of *section of Mathematical and Natural Sciences*. Royal Serbian Sciences, Belgrade. 633pp., Canon of Insolation and the Ice Age Problem, English Translation by Israel Program for Scientific Translation and published for the U.S. Department of Commerce and the National Science Foundation, Washington DC, 1969.

Miller J.R. and Russell G.L. (1989) Ocean heat transport during the last glacial maximum. *Paleoceanogr.*, 4(2):141–155.

Miller K.G., Fairbanks R.G., and Mountain G.S. (1987) Tertiary oxygeon isotope synthesis, sea-level history, and continental margin erosion. *Paleoceanography*, 2(1):1–20.

Mitchell J.F.B. (1993) Modelling of palaeoclimates: Examples from the recent past. *Phil. Trans. R. Soc. Lond. B*, 341:267–275.

Morales Maqueda M.A., Willmott A.J., Bamber J.L., and Darby M.S. (1998) An investigation of the small ice cap instability in the Southern Hemisphere with a coupled atmosphere-sea ice-ocean-terrestrial ice model. *Clim. Dyn.*, 14(5):329–352.

Morcrette J.J. (1990) Impact of changes to the radiation transfer parameterizations plus cloud optical properties in the ECMWF model. *Mon. Wea. Rev.*, 118:847–873.

Morcrette J.J. (1991) Radiation and cloud radiative properties in the European Centre for Medium Range Weather Forecasts forecasting system. *J. Geophys. Res.*, 96(D5):9121–9132.

Murdock T.Q., Weaver A.J., and Fanning A.F. (1997) Paleoclimatic response of the closing of the Isthmus of Panama in a coupled ocean-atmosphere model. *Geophys. Res. Let.*, 24(3):253–256.

Neeman B.U., Ohring G., and Joseph J.H. (1988a) The Milankovitch theory and climate sensitivity 1. equilibrium climate model solution for the present surface conditions. *J. Geophys. Res.*, 93(D9):11153–11174.

Neeman B.U., Ohring G., and Joseph J.H. (1988b) The Milankovitch theory and climate sensitivity 2. interaction between the northern hemisphere ice sheets and the climate system. *J. Geophys. Res.*, 93(D9):11175–11191.

Newell R.E. (1974) Changes in the poleward energy flux by the atmosphere and oceans as a possible cause for ice ages. *Quaternary Research*, 4:117–127.

Oerlemans J. (1980) Model experiments on the 100,000-yr glacial cycle. *Nature*, 287(5781):430–432.

Oerlemans J. (1981a) Modeling of pleistocene European ice sheets: Some experiments with simple mass-balance parameterizations. *Quat. Res.*, 15:77–85.

Oerlemans J. (1981b) Some basic experiments with a vertically integrated ice sheet model. *Tellus*, 33:1–11.

Oerlemans J. (1982) Glacial cycles and ice-sheet modelling. *Climatic Change*, 4:353–374.

Oerlemans J. (1991) The role of ice sheets in the pleistocene climate. *Norsk Geologisk Tidsskrift*, 71:155–161.

Oglesby R.J. (1989) A GCM study of Antarctic glaciation. *Clim. Dyn.*, 3(3):135–156.

Oglesby R.J. (1990) Sensitivity of glaciation to initial snow cover, CO_2, snow albedo, and oceanic roughness in the NCAR CCM. *Clim. Dyn.*, 4(4):219–235.

Overpeck J., Rind D., Lacis A., and Healy R. (1996) Possible role of dust-induced regional warming in abrupt climate change during the last glacial period. *Nature*, 384(6608):447–449.

Pacanowski R.C. (1996) MOM 2: Documentation user's guide and reference manual. GFDL Ocean Group Technical Report 3.2, NOAA, GFDL, Princeton, NJ. 329pp.

Pacanowski R.C. and Griffies S.M. (1999) MOM 3.0 manual. Tech. rep., NOAA, GFDL, Princeton, NJ. 668pp.

Paillard D. (1998) The timing of Pleistocene glaciations from a simple multiple-state climate model. *Nature*, 391(6665):378–381.

Parkinson C.L. and Washington W.M. (1979) A large-scale numerical model of sea ice. *J. Geophys. Res.*, 84(C1):311–337.

Paterson W.S.B. (1994) *The Physics of Glaciers*. Pergamon.

Pearson P.N. and Palmer M.R. (2000) Atmospheric carbon dioxide concentrations over the past 60 million years. *Nature*, 406(6797):695–699.

Peltier W.R. (1994) Ice age paleotopography. *Science*, 265(5169):195–201.

Peltier W.R. (1996) Mantle viscosity and ice-age ice sheet topography. *Science*, 273(5280):1359–1364.

Peltier W.R. (1998) Postglacial variations in the level of the sea: Implications for climate dynamics and solid-earth geophysics. *Rev. Geophys.*, 36(4):603–689.

Peltier W.R. and Marshall S. (1995) Coupled energy-balance/ice-sheet model simulations of the glacial cycle: A possible connection between terminations and terrigenous dust. *J. Geophys. Res.*, 100(D7):14269–14289.

Petit J.R., Jouzel J., Raynaud D., Barkov N.I., Barnola J.M., Basile I., Bender M., Chappellaz J., Devis M., Delaygue G., Delmotte M., Kotlyakov V.M., Legrand M., Lipenkov V.Y., Lorius C., Pépin L., Ritz C., Saltzman E., and Stievenard M. (1999) Climate and atmospheric history of the past 420,000 years from the Vostok ice core, Antarctica. *Nature*, 399(6735):429–436.

Phillipps P.J. and Held I.M. (1994) The response to orbital perturbations in and atmospheric model coupled to a slab ocean. *J. Clim.*, 7(5):767–782.

Pinot S., Ramstein G., Marsiat I., de Vernal A., Peyron O., Duplessy J.C., and Weinelt M. (1999) Sensitivity of the European LGM climate to North Atlantic sea-surface temperature. *Geophys. Res. Let.*, 26(13):1893–1896.

Pollard D. (1978) An investigation of the astronomical theory of the ice ages using a simple climate-ice sheet model. *Nature*, 272:233–235.

Pollard D. (1982) A simple ice sheet model yields realistic 100 kyr glacial cycles. *Nature*, 296:334–338.

Pollard D. (1983) A coupled climate-ice sheet model applied to the Quaternary ice ages. *J. Geophys. Res.*, 88(C12):7705–7718.

Pollard D. and Thompson S.L. (1997) Driving a high-resolution dynamic ice-sheet model with GCM climate: Ice-sheet initiation at 116 000 BP. *Ann. Glaciology*, 25:296–304.

Poore R.Z. (1981) Temporal and spatial distribution of ice-rafted mineral grains in Pliocene sediments of the North Atlantic: Implication for late Cenozoic climatic history. In R.G. Douglas and E. Winterer, eds., *Deep Sea Drilling Project - A Decade of Progress*, vol. 47, pages 433–445. SEPM Special Publication.

Poussart P.F., Weaver A.J., and Barnes C.R. (1999) Late Ordovician glaciation under high atmospheric CO_2: A coupled model analysis. *Paleoceanogr.*, 14(4):542–558.

Rahmstorf S. (1993) A fast and complete convection scheme for ocean models. *Ocean Modelling*, 101:9–11.

Rahmstorf S. (1996) On the freshwater forcing and transport of the Atlantic thermohaline circulation. *Clim. Dyn.*, 12(12):799–811.

Rahmstorf S., Marotzke J., and Willebrand J. (1996) Stability of the thermohaline circulation. In W. Krauss, ed., *The Warmwatersphere of the North Atlantic Ocean*, pages 129–157. Gebrüder Borntraeger, Berlin, Stuttgart.

Ramanathan V., Callis L., Cess R., Hansen J., Isaksen I., Kuhn W., Lacis A., Luther F., Mahlman J., Reck R., and Schlesinger M. (1987) Climate-chemical interactions and effects of changing atmospheric trace gases. *Rev. Geophys.*, 25(7):1441–1482.

Raymo M.E. (1994) The initiation of Northern Hemisphere glaciation. *Ann. Rev. Earth Planet. Sci.*, 22:353–383.

Raymo M.E. (1997) The timing of major climate terminations. *Paleoceanogr.*, 12(4):577–585.

Raynaud D., Jouzel J., Barnola J.M., Chappellaz J., Delmas R.J., and Lorius C. (1993) The ice record of greenhouse gases. *Science*, 259:926–934.

Rind D. and Peteet D. (1985) Terrestrial conditions at the Last Glacial Maximum and CLIMAP sea-surface temperature estimates: Are they consistent? *Quat. Res.*, 24(1):1–22.

Rind D., Peteet D., Broecker W., McIntyre A., and Ruddiman W. (1986) The impact of cold North Atlantic sea surface temperatures on climate: Implications for the Younger Dryas cooling. *Clim. Dyn.*, 1(1):3–33.

Rind D., Peteet D., and Kukla G. (1989) Can Milankovitch orbital variations initiate the growth of ice sheets in a general circulation model? *J. Geophys. Res.*, 94(D10):12851–12871.

Robin G.Q. (1988) The Antarctic ice sheet, its history and response to sea level and climatic change over the past 100 million years. *Plaeogeogr. Palaeoclim. Palaeoecol.*, 67:31–50.

Roemmich D. and Wunsch C. (1985) Two transatlantic sections: Meridional circulation and heat flux in the subtropical North Atlantic Ocean. *Deep-Sea Res.*, 32(6):619–664.

Royer J.F. and Deque M. (1983) Orbital forcing of the inception of the Laurentide ice sheet? *Nature*, 304(5921):43–46.

Royer J.F., Deque M., and Pestiaux P. (1984) A sensitivity experiment to astronomical forcing with a spectral GCM: Simulation of the annual cycle at 125 000 BP and 115 000 BP. In A.L. Berger, J. Imbrie, J. Hays, G. Kukla, and B. Saltzman, eds., *Milankovitch and Climate Part 2*, pages 733–763. D. Reidel Publishing Company, Dordrecht, Holland.

Ruddiman W.F. (2001) *Earth's Climate: Past and Future*. W. H. Freeman and Company, New York, NY. 465pp.

Ruddiman W.F. and McIntyre A. (1979) Warmth of the subpolar North Atlantic ocean during Northern Hemisphere ice-sheet growth. *Science*, 204(4389):173–175.

Ruddiman W.F. and McIntyre A. (1981) Oceanic mechanisms for amplification of the 23,000-year ice-volume cycle. *Science*, 212(4495):617–627.

Ruddiman W.F., McIntyre A., Niebler-Hunt V., and Durazzi J.T. (1980) Oceanic evidence for the mechanism of rapid Northern Hemisphere glaciation. *Quat. Res.*, 13(1):33–64.

Rutberg R.L., Hemming S.R., and Goldstein S.L. (2000) Reduced North Atlantic Deep Water flux to the glacial Southern Ocean inferred from neodymium isotope ratios. *Nature*, 405(6789):935–938.

Saltzman B. (1990) Three basic problems of paleoclimatic modeling: A personal perspective and review. *Clim. Dyn.*, 5(2):67–78.

Savin S.M., Douglas R.G., and Stehli F.G. (1975) Tertiary marine palaeotemperatures. *Geological Society of America Bulletin*, 86:1499–1510.

Schlesinger M.E. and Verbitsky M. (1996) Simulation of glacial onset with a coupled atmospheric general circulation/mixed layer ocean - ice-sheet/asthenosphere model. *Paleoclimates*, 2:179–201.

Schmittner A., Yoshimori M., and Weaver A.J. (2001) Instability of glacial climate in an Earth System Climate Model. *Science*. Submitted.

Schnitker D. (1980) North Atlantic oceanography as possible cause of Antarctic glaciation and eutrophication. *Nature*, 284:615–616.

Semtner Jr. A.J. (1976) A model for the thermodynamic growth of sea ice in numerical investigations of climate. *J. Phys. Oceanogr.*, 6(3):379–389.

Send U. and Marshall J. (1994) Integral effects of deep convection. *J. Phys. Oceanogr.*, 25(5):855–872.

Shackleton N.J. (1967) Oxygen isotope analyses and Pleistocene temperatures re-assessed. *Nature*, 215:15–17.

Shackleton N.J. (1987) Oxygen isotopes, ice volume and sea level. *Quat. Sci. Rev.*, 6:183–190.

Shackleton N.J. (2000) The 100,000-year ice-age cycle identified and found to lag temperature, carbon dioxide, and orbital eccentricity. *Science*, 289(5486):1897–1902.

Shackleton N.J., Backman J., Zimmerman H., Kent D.V., Hall M.A., Roberts D.G., Schnitker D., Baldauf J.G., Desprairies A., Homrighausen R., Huddlestun P., Keene J.B., Kaltenback A.J., Krumsiek K.A.O., Morten A.C., Murray J.W., and Westberg-Smith J. (1984) Oxygen isotopic calibration of the onset of ice-rafting and history of glaciation in the North Atlantic region. *Nature*, 307:620–623.

Shackleton N.J. and Kennett J.P. (1975a) Late Cenozoic oxygen and carbon isotopic changes at deep sea drilling project site 284: Implication for glacial history of the Northern Hemisphere and Antarctica. In R.E.H. J. P. Kennett et al., eds., *Initial Reports of the Deep Sea Drilling Project*, vol. 29, pages 801–807. U.S. Government Printing Office, Washington D.C.

Shackleton N.J. and Kennett J.P. (1975b) Paleotemperature history of the Cenozoic and the initiation of Antarctic glaciation: Oxygeon and carbon isotopic analyses in DSDP sites 277, 279, and 281. In R.E.H. J. P. Kennett et al., eds., *Initial Rep. Deep Sea Drill. Proj.*, vol. 29, pages 743–755. U.S. Government Printing Office, Washington D.C.

Shackleton N.J. and Opdyke N.D. (1977) Oxygen isotope and palaeomagnetic evidence for early Northern Hemisphere glaciation. *Nature*, 270:216–219.

Short D.A., Mengel J.G., Crowley T.J., Hyde W.T., and North G.R. (1991) Filtering of Milankovitch cycles by Earth's geography. *Quat. Res.*, 35:157–173.

Sigman D.M. and Boyle E.A. (2000) Glacial/interglacial variations in atmospheric carbon dioxide. *Nature*, 407(6806):859–869.

Sowers T. and Bender M. (1995) Climate records covering the last deglaciation. *Science*, 269(5221):210–214.

Sowers T., Bender M., Raynaud D., Korotkevich Y.S., and Orchardo J. (1991) The δ^{18}O of atmospheric O_2 from air inclusions in the Vostok ice core: Timing of CO_2 and ice volume changes during the penultimate deglaciation. *Paleoceanogr.*, 6(6):679–696.

Steen R.S. and Ledley T.S. (1997) Asynchronously coupling the cryosphere and atmosphere in an energy-balance climate model. *Ann. Glaciology*, 25:159–164.

Stipp J.J., Chappell J.M.A., and McDougall I. (1967) K/ar age estimate of the Pliocene-Pleistocene boundary in New Zealand. *American Journal of Science*, 265:462–474.

Stommel H. (1961) Thermohaline convection with two stable regimes of flow. *Tellus*, 13(2):224–230.

Syktus J., Gordon H., and Chappell J. (1994) Sensitivity of a coupled atmosphere-dynamic upper ocean GCM to variations of CO_2, solar constant, and orbital forcing. *Geophys. Res. Let.*, 21(15):1599–1602.

Tarasov L. and Peltier W.R. (1997a) A high-resolution model of the 100 ka ice-age cycle. *Ann. Glaciology*, 25:58–65.

Tarasov L. and Peltier W.R. (1997b) Terminating the 100 kyr ice age cycle. *J. Geophys. Res.*, 102(D18):21665–21693.

Tarasov L. and Peltier W.R. (1999) The impact of thermomechanical ice sheet coupling on a model of the 100 kyr ice age cycle. *J. Geophys. Res.*, 104(D8):9517–9545.

Thompson S.L. and Pollard D. (1997) Ice-sheet mass balance at the last glacial maximum from the GENESIS version 2 global climate model. *Ann. Glaciology*, 25:250–258.

Thompson S.L. and Warren S.G. (1982) Parameterization of outgoing infrared radiation derived from detailed radiative calculations. *J. Atmos. Sci.*, 39(12):2667–2680.

Tiedemann R., Sarnthein M., and Shackleton N.J. (1994) Astronomic timescale for the Pliocene Atlantic $\delta^{18}O$ and dust flux records of ocean drilling program site 659. *Paleoceanogr.*, 9(4):619–638.

Trenberth K.E. and Solomon A. (1994) The global heat balance: Heat transport in the atmosphere and ocean. *Clim. Dyn.*, 10(3):107–134.

UNESCO (1981) 10th report of the joint panel on oceanographic tables and standards. Technical Report UNESCO Technical Papers in Marine Science 36, UNESCO, Paris.

van de Wal R.S.W. (1999) The importance of thermodynamics for modeling the volume of the Greenland ice sheet. *J. Geophys. Res.*, 104(D4):3887–3898.

Van Zinderen Bakker E.M. and Mercer J.H. (1986) Major late Cainozoic climatic events and paleoenvironmental changes in Africa viewed in a world wide context. *Plaeogeogr. Palaeoclim. Palaeoecol.*, 56:217–235.

Vavrus S.J. (1999) The response of the coupled arctic sea ice-atmosphere system to orbital forcing and ice motion at 6 kyr and 115 kry bp. *J. Clim.*, 12(3):873–896.

Verbitsky M.Y. and Oglesby R.J. (1992) The effect of atmospheric carbon dioxide concentration on continental glaciation of the Northern Hemisphere. *J. Geophys. Res.*, 97(D5):5895–5909.

Vettoretti G., Peltier W.R., and McFarlane N.A. (2000) Global water balance and atmospheric water vapour transport at last glacial maximum: Climate simulations with the Canadian Climate Centre for Modelling and Analysis atmospheric general circulation model. *Can. J. Earth Sci.*, 37:695–723.

Walland D.J. and Simmonds I. (1996) Sub-grid-scale topography and the simulation of Northern Hemisphere snow cover. *International Journal of Climatology*, 16:961–982.

Weaver A.J., Bitz C.M., Fanning A.F., and Holland M.M. (1999) Thermohaline circulation: High-latitude phenomena and the differnece between the pacific and atlantic. *Ann. Rev. Earth Planet. Sci.*, 27:231–285.

Weaver A.J., Eby M., Fanning A.F., and Wiebe E.C. (1998) Simulated influence of carbon dioxide, orbital forcing and ice sheets on the climate of the Last Glacial Maximum. *Nature*, 394(6696):847–853.

Weaver A.J., Eby M., Wiebe E.C., Bitz C.M., Duffy P.B., Ewen T.L., Fanning A.F., Holland M.M., MacFadyen A., Matthews H.D., Meissner K.J., Saenko O., Schmittner A., Wang H., and Yoshimori M. (2001) The UVic Earth System Climate Model: Model description, climatology, and application to past, present and future climates. *Atmos-Ocean*. In press.

Weaver A.J. and Hughes T.M.C. (1992) Stability and variability of the thermohaline circulation and its link to climate. In *Trends in Physical Oceanography*, vol. 1 of *Research Trends Series*, pages 15–70. Council of Scientific Research Integration, Trivandrum, India.

Weaver A.J. and Hughes T.M.C. (1996) On the incompatibility of ocean and atmosphere models and the need for flux adjustments. *Clim. Dyn.*, 12(3):141–170.

Webb R.S., Rind D.H., Lehman S.J., Healy R.J., and Sigman D. (1997) Influence of ocean heat transport on the climate of the Last Glacial Maximum. *Nature*, 385(6618):695–699.

Weertman J. (1961) Stability of ice-age ice sheets. *J. Geophys. Res.*, 66(11):3783–3792.

Weertman J. (1976) Milankovitch solar radiation variations and ice age ice sheet sizes. *Nature*, 261:17–20.

Wiebe E.C. and Weaver A.J. (1999) On the sensitivity of global warming experiments to the parameterisation of sub-grid scale ocean mixing. *Clim. Dyn.*, 15(12):875–893.

Wilson M.F. and Henderson-Sellers A. (1985) A global archive of land cover and soils data for use in general circulation climate models. *J. Climatology*, 5:119–143.

Wolfe A. (1994) Tertiary climatic changes in western North America. *Plaeogeogr. Palaeoclim. Palaeoecol.*, 108:195–205.

Woodruff F., Savin S.M., and Douglas R.G. (1981) Miocene stable isotope record: A detailed deep Pacific ocean study and its paleoclimatic implications. *Science*, 212:665–668.

Worthington L.V. (1968) Genesis and evolution of water masses. *Meteorological Monographs*, 8:63–67.

Wyle P.K. (1968) The role of the oceans in climatic change: A theory of ice ages. *Meteorological Monographs*, 8:37–62.

Yu E.F., Francois R., and Bacon M.P. (1996) Similar rates of modern and last-glacial ocean thermohaline circulation inferred from radiochemical data. *Nature*, 379:689–694.

Zhang B. (1989) Controversy regarding the exsistence of a large ice sheet on the Qinghai-Xizang (Tibetan) Plateau during the Quaternary period. *Quat. Res.*, 32(1):121–123.

Glossary of Acronyms

- AABW - Antarctic Bottom Water
- AGCM - atmospheric general circulation model
- BP - before present
- CCCma - Canadian Centre for Climate Modelling and Analysis (Victoria, BC, Cadana)
- CCM - Community Climate Model
- CIDM - Continental Ice Dynamics Model
- CISRO - Commonwealth Scientific and Industrial Research Organization (Melbourne, Australia)
- CLIMAP - Climate: Long-Range Investigation Mapping and Prediction
- EERM - d'Etudes et de Recherches Météorologiques (Paris, France)
- EMBM - Energy-Moisture Balance Model
- GCM - general circulation model
- GCMII - CCCma second generation general circulation model
- GENESIS - Global Environmental and Ecological Simulation of Interactive Systems
- GFDL - Geophysical Fluid Dynamics Laboratory (Princeton, NJ, USA)
- GISS - Goddard Institute for Space Studies (New York, NY, USA)
- ka - kiloannum = thousand years
- LGM - last glacial maximum
- LMD - Laboratoire de Météorologie Dynamique (Saclary, Gif-sur-Yvette, France)
- Ma - Million years
- MOM - Modular Ocean Model
- MPI - Max Plank Institute of Meteorology (Hamburg, Germany)

- NADW - North Atlantic Deep Water
- NASA - National Aeronautics and Space Administration (USA)
- NCAR - National Center for Atmospheric Research (Boulder, CO, USA)
- NH - Northern Hemisphere
- NOAA - National Oceanic and Atmospheric Administration (USA)
- OGCM - ocean general circulation model
- OSU - Oregon State University
- PD - present-day
- ppmv - parts per million by volume
- SAT - surface air temperature
- SH - Southern Hemisphere
- SPECMAP - Spectral Mapping Analysis of the Pleistocene
- SST - sea surface temperature
- UGAMP - U.K. Universities Global Atmospheric Modelling Programme